Title
Design of A System for Cancelling Stimulus Artifact in Multi-Channel Neural Interfaces

Author
Culaclii, Stanislav

Publication Date
2019

Peer reviewed|Thesis/dissertation

UNIVERSITY OF CALIFORNIA

Los Angeles

Design of A System for Cancelling Stimulus Artifact in Multi-Channel Neural Interfaces

A dissertation submitted in partial satisfaction of the

requirements for the degree Doctor of Philosophy

in Bioengineering

by

Stanislav Culaclii

2019

ABSTRACT OF THE DISSERTATION

Design of A System for Cancelling

Stimulus Artifact in Multi-Channel Neural Interfaces

by

Stanislav Culaclii

Doctor of Philosophy in Bioengineering

University of California, Los Angeles, 2019

Professor Wentai Liu, Chair

Bidirectional neural interfaces record electrical activity in neurons and modulate their signaling by suppressing or enhancing the activity via an electronic device. Such devices have been shown to treat and rehabilitate subjects suffering from neural diseases as well as to conduct research to advance the treatment methods. These applications require a new paradigm, which is currently widely explored in neural interface designs: the ability to stimulate and record simultaneously to explore complex tissue responses and to automatically adjust the stimulation in real-time based on the recorded data, thus “closing the loop”.

The recordings are contaminated by a stimulation artifact which is formed when the stimulation current flows into the device-tissue interface and is recorded at the time of stimulation event as an undesired waveform. This waveform often overwhelms the recording device and disturbs the recording data long enough to overlap with the response of the neural tissue to the

stimulation. To isolate the response from the contaminating artifact, a sophisticated artifact cancellation methodology is needed. Current state-of-the-art works offer solutions to the artifact problem but are practically constrained in the maximum artifact amplitude they can accommodate. A generalized framework and a corresponding methodology are thus developed and described in this work.

The proposed architecture uses a combination of a coarse feedback in analog domain with a template generation in the digital domain to suppress artifacts and separate them from the underlying neural signals. Two variants of the design are discussed and then tested for studies of neural networks. The design is validated in-vivo in a deep brain stimulation of a hippocampus in a rodent model. The design is also validated in-vitro in an emulated stimulation and recording of a rodent spinal cord, based on preliminary in-vivo work conducted prior. The architecture notably performed artifact cancellation and recording of neural signals in-vivo on the stimulating electrode with a large artifact. A ~1V artifact was generated and suppressed with an unprecedented ratio of 80-100dB, while recovering the neural signals.

The dissertation of Stanislav Culaclii is approved.

Jonathan Chau-Yan Kao

Pei-Yu Chiou

Richard Joseph Staba

Wentai Liu, Committee Chair

University of California, Los Angeles

2019

To my dear sister Eleonora

who never gave up the fight in the face of her adversities

and inspired my field of research.

Table of Contents

List of Figures

List of Tables

Acknowledgements

First and foremost, I'd like to acknowledge my adviser Dr. Wentai Liu, for guiding and motivating the research in our lab through his insightful vision and his inspiring passion. I'm thankful for his dedication to the research, for the early mornings during which he reviewed and responded to our reports and manuscript drafts, for the long lunches during which he mentored us on the direction of our projects and research, and many long nights when he stayed side-by-side with us through the endless testing and troubleshooting of our designs. It's very rare and valuable to be under a leadership of a professor who is persistently "in the trenches" with his students, sharing the highs and the lows of each step of the project. Finally, his persistent and unique way of challenging and questioning the conventional thinking in my work, symbolized in his phrase "so what is new about this?", sent me back to the drawing boards many times in the search of a better and more impactful path in my work. The takeaways and lessons Dr. Liu shared with me will stay with me for the remainder of my career and I am very grateful for this.

I also want to thank my panel for aiding me in my work and for their time to review and critique my dissertation defense. Dr. Staba helped us to establish collaboration with his colleagues to conduct animal testing and thus increase the impact of my work. Dr. Chiou's lectures in microfabrication provide me with critical knowledge needed for the troubleshooting of our chronic in-vivo implants, which became one of the pillars for my dissertation. Dr. Kao's comprehensive neural signal processing class enabled me to conduct a detailed analysis of the signals I collected which greatly enhanced my dissertation.

I'd like to also thank our collaborators Dr. Bragin and Dr. Li who provided their resources and mentorship for the animal testing of our design, and Dr. Taccola who worked closely with our

laboratory to apply our technologies to his research to discover novel and effective protocols in the field of therapy for spinal cord injuries.

I'd like to thank Dr. Yi-Kai Lo who, as a post-doc during my first years in the lab, has guided me through the nuts and bolts of conducting a research and openly shared numerous advices and ideas, one of which became the back-bone of this dissertation. I'm also grateful for the other graduate and undergraduate students in our lab who shared the joys and miseries of the daily grinds during the seemingly endless years of my PhD.

Finally, I'd like to extend my sincere gratitude to my family. My parents gave me unconditional support throughout my life, and the period of my PhD was no exception. My wife Naomi was always there for me to bring me back to life after many planned and unplanned emotional and physical burnouts. I also want to thank her for building a custom tool to help me greatly speed up processing of in-vivo data for my manuscript. Last but not least, my son Christopher has unknowingly taught me what it means to be truly relentless in learning and to live life just one moment at a time. He was born as I began to write this dissertation and quickly became my most favorite "artifact" of them all.

Sections of Chapters 2 and 4 borrow from [1], while Chapter 3 is largely adopted from [1]. Our research was supported in part by the Endowment for the Chan Soon-Shiong Bionic Engineering Research Center at University of California, Los Angeles by California Capital Equity LLC, NIH BRP U01 EB007615, and NIH SPARC #1OT2OD024899.

Vita

Education

B.S. Electrical Engineering, University of California, Los Angeles	2004 - 2007
M.S. Electrical Engineering, University of California, Los Angeles	2007 - 2009
M.S. Bioengineering, University of California, Los Angeles	2019

Prior Experience

Engineering Intern, Hughes Research Laboratory, LLC.	2008 - 2009
Malibu, CA	
Senior Electrical Engineer, Raytheon Co.	2009 - 2014
Space and Airborne Systems, El Segundo, CA	

Publications

- Taccola, G., Gad, P., **Culaclii, S.**, Ichiyama, R. M., Liu, W., & Edgerton, V. R. (2019). "Using EMG to deliver lumbar dynamic electrical stimulation to facilitate cortico-spinal excitability". Brain Stimulation.
- Wang P.M.*, **Culaclii S.***, Yang, W., Long Y., Massachi J., Lo Y.K., Liu W., "A Novel Biomimetic Stimulator System for Neural Implant," in 2019 9th International IEEE/EMBS Conference on Neural Engineering (NER), 2019, pp. 843–846.
- Wang P.-M., **Culaclii S.**, Seo K. J., Wang Y., Fang H., Lo Y.-K., Liu W. (2019). Challenges in the Design of Large-Scale, High-Density, Wireless Stimulation and Recording Interface, New York, NY: Springer, in press.

- **Culaclii, S.**, Kim, B., Li, L., Lo, Y.K., Liu, W. (2018). Online Artifact-Cancellation In Same-electrode Neural Stimulation and Recording Using a Combined Hardware and Software Architecture. IEEE Transactions on Biomedical Circuits and Systems, PP(99), 1–13.
- Qiang Y.†, Artoni P.†, Seo K. J.†, **Culaclii S.**, Hogan V., Zhao X., Zhong Y., Han X., Wang P.-M., Lo Y.-K., Li Y., Patel H. A., Huang Y., Sambangi A., Chu J. S. V., Liu W., Fagiolini M.*, Fang H.*, (2018). "Transparent Arrays of Bilayer-Nanomesh Microelectrodes for Simultaneous Electrophysiology and 2-Photon Imaging in the Brain", Science Advances, vol. 4, no. 9, p. eaat0626, Sep. 2018.
- Qiang, Y., Seo, K. J., Zhao, X., Artoni, P., Golshan, N. H., **Culaclii, S.**, Wang P.-M., Liu W., Ziemer K., Fagiolini M., Fang, H. (2017). Bilayer Nanomesh Structures for Transparent Recording and Stimulating Microelectrodes. Advanced Functional Materials, 27(48).
- Lo, Y. K., Kuan, Y. C., **Culaclii, S.**, Kim, B., Wang, P. M., Chang, C. W., Massachi J. A., Zhu M., Chen K., Gad P., Edgerton, V. R. (2017). A fully integrated wireless SoC for motor function recovery after spinal cord injury. IEEE transactions on biomedical circuits and systems, 11(3), 497-509.
- **Culaclii, S.***, Kim, B.*, Lo, Y. K., & Liu, W. (2016, August). A hybrid hardware and software approach for cancelling stimulus artifacts during same-electrode neural stimulation and recording. In Engineering in Medicine and Biology Society (EMBC), 2016 IEEE 38th Annual International Conference of the (pp. 6190-6193). IEEE.
- Lo, Y. K., Chang, C. W., Kuan, Y. C., **Culaclii, S.**, Kim, B., Chen, K., ... & Liu, W. (2016, January). 22.2 A 176-channel 0.5 cm3 0.7 g wireless implant for motor function recovery after spinal cord injury. In Solid-State Circuits Conference (ISSCC), 2016 IEEE International (pp. 382-383). IEEE.

Chapter 1

Introduction

1.1 Introduction to Neural Interfaces

Neural interfaces are the devices that are intended to interact with the nervous system for a two-way exchange of information. Natural communication within the nervous system is naturally established through relay of impulses called action potentials. These action potentials can be read out to recover critical information. The information can then be used to assess a condition of an organ or a state of a physiological subsystem of the body. The neural interface devices are designed to extract these action potentials from the nervous system by electrically recording its signals. Conversely the information can be introduced into the nervous system by inducing action potentials [2]. The neural interface device facilitates this by injecting electrical stimuli from outside of neural cells, which affects the voltage gradient across the membranes of the neurons, and subsequently triggers neuronal responses. This is ultimately done to exercise some kind control over the signals within the nervous system [3]. When electrical stimulation is used for the purposes of restoring a body or system function which is otherwise impaired by disease or other disability, the device performing the stimulation is called a neural prosthesis. Information can also flow in both directions to create a feedback loop where the input from the device is adjusted based on the output from the organism's neural signaling. This feedback is a basis for closed-loop prosthetic devices [2].

Historically, electrical stimulation of motor cortex to elicit limb movement was reported first in canines in 1870 [4] and later in humans by 1874 [5]. On the other hand, in the 1950s wires were introduced that were first to measure chronical activity from the brain in animal models. This followed by patch-clamp electrophysiology in the 1970s [6]. Today, the interfaces to the central

nervous system (CNS) have become a major focus of neuroengineering research. Needs for interfacing with CNS include regulating mood disorders, epilepsy or Parkinson's symptoms with deep brain stimulation (DBS) [2]. Despite many hypotheses proposed, the exact mechanisms of action of DBS is still not fully understood. One approach to better appraise these hypotheses is to record the changes occurring in neuronal activities during DBS [7]. The needs also include electrical stimulation of the spinal cord, to restore function in individuals with paralysis caused by spinal cord injuries (SCI). A popular approach utilizes implanted electrodes to pass an electrical stimulus across the SCI wound to stimulate injured axons, which promotes regrowth of injured axons to reconnect with proper targets. Still during the past three decades, in-vivo electrical stimulation to treat SCI has exhibited mixed results. Moreover, to date, the exact mechanism by which electrical stimulation improves axonal regeneration and/or functionality in animal and human nerve injury remains unknown, motivating need for further studies [8].

1.2 The Challenge of a Stimulation Artifact

Neural interface devices which study neural network dynamics make use of active manipulation of neuron populations by means of electrical stimulation while simultaneously recording their electrical activity [9]. Along with neuronal activity, these devices record the undesired artifact waveforms resulting from the applied stimulation. These stimulation artifacts can be several orders of magnitude larger in amplitude than the recorded neuron potentials, and as a result can saturate the recording amplifier and make the detection of the neuron responses very difficult [10]. A method to remove the artifacts is thus required to make further advancements in these designs.

There already exists a large body of published work on the topic of stimulation artifact removal. Some date as far back as 1920s [11]. And yet this area of research is still relevant and ongoing. As with all engineering, trade-offs exist for every design, limiting their use for specific applications and use cases. Thus, as the applications of neuroscientific research evolve and experiment parameters and requirements change, so must the tools. Bidirectional neural interfaces and their abilities to perform artifact suppression are no exception. Many recent advances made in artifact cancellation focus on brain stimulation and recording for the purposes of improvements of therapeutic interventions for various brain diseases. The corresponding neural interface innovations thus constrain themselves to a common set of parameters, such as specific artifact frequencies and amplitudes, and separation between the neural signals and artifacts in frequency domain [12]. In our recent exploration and development of tools for research on spinal cord injury and the corresponding rehabilitation methods [13], we have found the existing artifact cancellation techniques to be insufficient for the experiment requirements. This motivated a new study for a step to a more generalized framework for cancelling artifact, which includes accommodating and suppressing larger artifacts, which strongly overlap in frequency with the underlying recorded neural signals. This thesis is a result and record of that study.

1.3 Thesis Outline

The remaining pages of the thesis are organized in the following order. Chapter 2 details the background information and theory of the stimulation artifact and neural signals, surveys the state-of-the-art, and discusses relevant applications that are targeted by this work. Chapter 3 discusses the development of a system targeting stimulation and recording of neural tissue simultaneously on the same electrode. Discussion includes definition of requirements, the

proposed architecture, the implementation of both the hardware circuits and signal processing algorithms. In-vitro and in-vivo studies are shown outlining the key results and paving the way for further improvements of the design. Chapter 4 discusses the expansion of the system to a multi-channel design, specifically targeting recording of spinal cord's evoked potentials during epidural stimulation for studies of rehabilitation protocols in rodent models for spinal cord injury. The design and implementation are presented in detail, and in-vitro results are demonstrated. Finally, Chapter 5 concludes the accomplishment, outlines future work and projects new challenges for next generation bidirectional neural interfaces based on our related recent work.

Chapter 2

Background Knowledge and State-of-the-art

2.1 The Characteristics of a Stimulation Artifact

2.1.1 The Stimulation Artifact Waveform

To aid the discussion of the solutions which remove the artifact, it is important to first understand the details of the stimulation artifact waveform. When the stimulating current interacts with the chemical interface which forms between an electrode, tissue and surrounding electrolyte such as extracellular fluid, it causes changes to the chemistry in the interface, due to the charge being transferred by the current flow. There are two primary mechanisms of charge transfer at the electrode/electrolyte interface. One is non-Faradaic reaction, where no electrons are transferred between the electrode and electrolyte. Instead a redistribution of charged chemical species occurs in the medium to accommodate the current flow. The second mechanism is a Faradaic reaction, in which electrons are transferred between the electrode and electrolyte at the interface [14].

Both mechanisms can be conveniently modelled with equivalent electrical circuit components. The non-Faradaic charge redistribution may be modeled as a simple electrical "double-layer" capacitor, C_{dl}. The Faradaic processes can be modeled by a Faradaic impedance. This impedance doesn't have an exact equivalent among standard circuit components but can be approximated by a resistor R_{ct} (for charge transfer). Finally, the flow of charges from the interface into the greater electrolyte medium can be modeled by a solution resistance, R_s [14]. The three-component model of the interface, called the Randles cell, is depicted in Figure 2-1 (left).

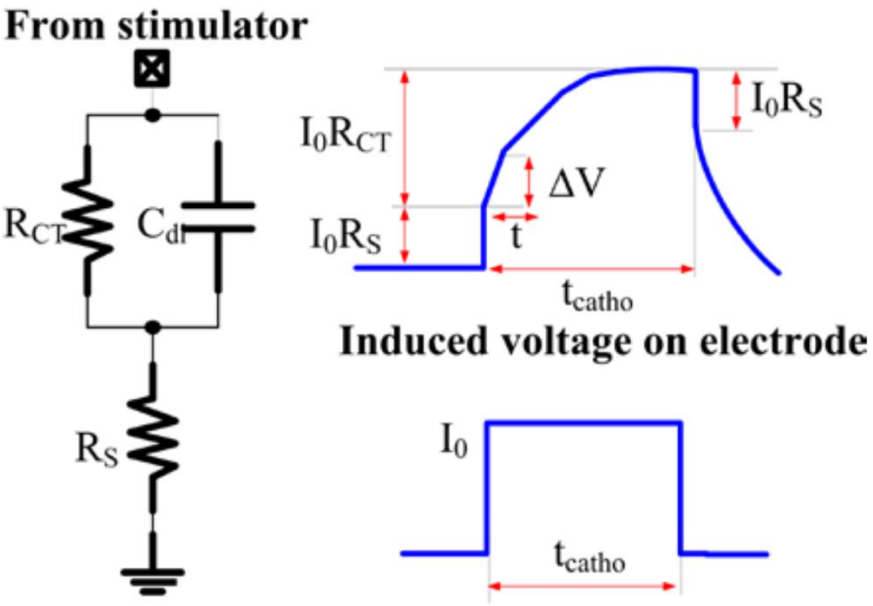

Figure 2-1. The electrode tissue interface and stimulation waveform.
The interface is modeled as a three-component Randles cell. The current pulse I_0 injected into the interface produces a stimulation artifact on top, right. Adopted from [15].

The transient voltage that forms the stimulation artifact when a stimulating current is injected into the electrode, can approximately predicted by deriving the time domain response of the Randles cell model to a stimulating current pulse. For a current step input I_0 (Figure 2-1, bottom right), the voltage across the terminals of the Randles cell can be expressed in the Laplace domain as a product of a current step and the cell's total impedance: $I_0/s * [R_{ct}/(1 + sR_{ct}C_{dl}) + R_s]$. The time domain equation is derived by taking the inverse of Laplace transform:

$$V(t) = \left[I_0 * R_{ct}\left(1 - e^{\frac{-t}{Rct*Cdl}}\right) + I_0 * R_s\right] * u(t) \qquad (2\text{-}1)$$

The equation can be considered as a sum of two main terms that compose the total electrode voltage. The first term, containing an exponential settling towards a final value $I_0 * R_{ct}$ represents processes at the narrow electrode-tissue interface. The second term $I_0 * R_s$ is the voltage drop of the stimulation current across the resistance of the saline. Figure 2-1, top right, displays the corresponding waveform. This waveform and its composing terms well describe a typical

stimulation artifact on a single electrode. Additionally we extrapolate this analysis to model the artifacts which form on multiple channels of an electrode array in Sections 4.3.2 and 4.3.3.

2.1.2 Artifact Amplitude vs. Distance to Site of Stimulation

Finally, it is useful to point out the relationship between an artifact formed at the stimulation electrode and one recorded at an electrode distant from the site of stimulation. In-vivo recordings in Figure 2-2 show that the closer the distance, the larger the artifact. This can also be extrapolated to the extreme: the largest artifact waveform will be observed at the stimulation electrode. Unlike notable published works on artifact cancellation, which avoid recording at the stimulating electrode, due to the challenges with the large artifact amplitude, the methodology proposed in this thesis is capable of recording at all locations, including the same-electrode stimulation and recording. This allows capture of complete set of neural responses across all available electrodes in the electrode array and thus a more complete analysis of neural networks.

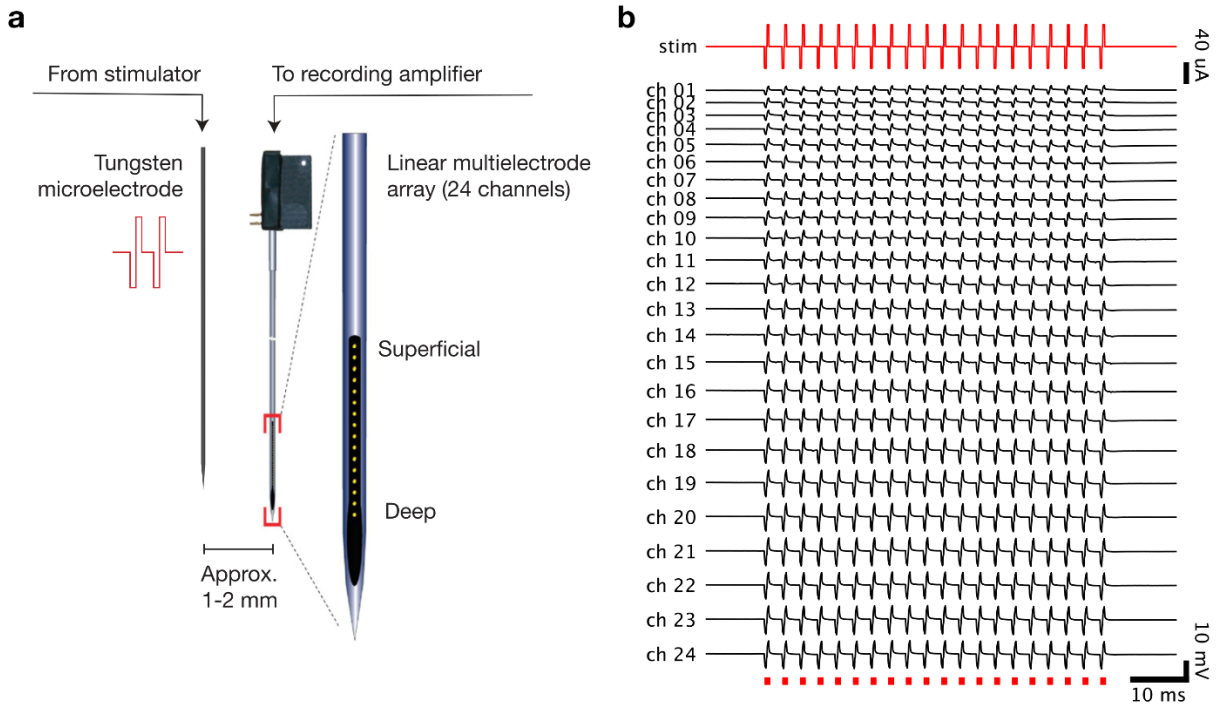

Figure 2-2. Stimulation artifact amplitude vs. distance to stimulation electrode.
The amplitude at each recording channel varies depending on the distance to the stimulation electrode. Adopted from [16].

2.2 Characteristics of Neural Responses to Stimulation

2.2.1 The Stimulation Threshold

The usefulness of an electrical stimulation in neural prosthesis depends on the ability to chronically provide safe levels of therapeutic stimulation [17]. This sets the limits – maximum (safety) and minimum (therapeutic) – for the parameters of the stimulation currents. The minimum limit is defined as one which produces a desired effect. This effect, from the point of view of neural recording, is commonly an electrophysiological neural response which follows the stimulation event. Electrical stimulation initiates a functional response by depolarizing the membranes of excitable cells, which is achieved by the flow of ionic current from the electrode in proximity to the target tissue [17]. The minimal stimulation amplitude and pulse width that produces a response is governed by strength-duration curve which is in turn dependent on the properties of the electrode and its location, which affects the amount of charge it can deliver to the neurons of interest. It also depends on the properties and state of the neural tissue, which affects its excitability – the minimal amount of charge that needs to be injected to trigger an action potential. Stimulation threshold in terms of charge delivered is summarized in [17] assuming common neural interface setup for each application listed. For a specific experiment or study and for a specific test subject this threshold is determined experimentally by sweeping the stimulus intensity from low to high (Figure 2-3). When the threshold is reached an obvious response appears after the artifact.

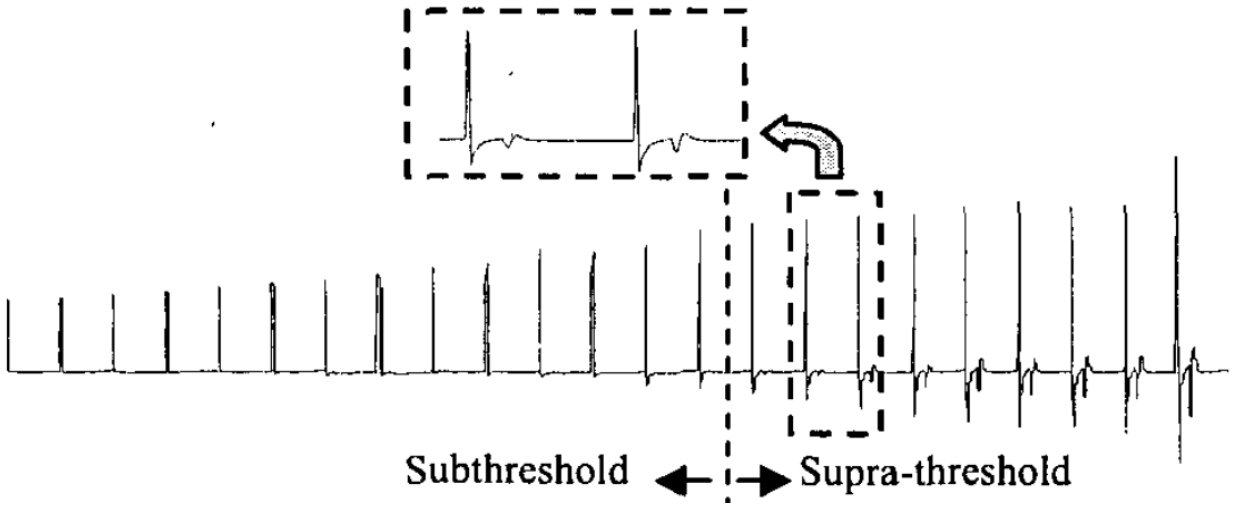

Figure 2-3. Concept of the electrical stimulation threshold.
When the intensity of the stimulation crosses a threshold, a neural response appears after the stimulation artifact. To determine the threshold the stimulation amplitude or pulse width sweep is performed while observing the recording signals. Adopted from [18].

2.2.2 Latency from Stimulation Event to The Neural Response

If the tissue is stimulated near the threshold level, there will be a probability between zero and one of whether a response will be evoked with each stimulus [18]. This is because the excitability of a tissue varies based on additional hidden factors, which include background processes, such as signals conducted by other neurons connected to this tissue. If an internal action potential from another neuron fires close to the time when the external electrical stimulus is delivered, they can sum directly to a larger total amplitude and thus generate a response. Conversely, if the internal action potential delivered is of opposite polarity, then it can subtract from the external stimulus and prevent a response.

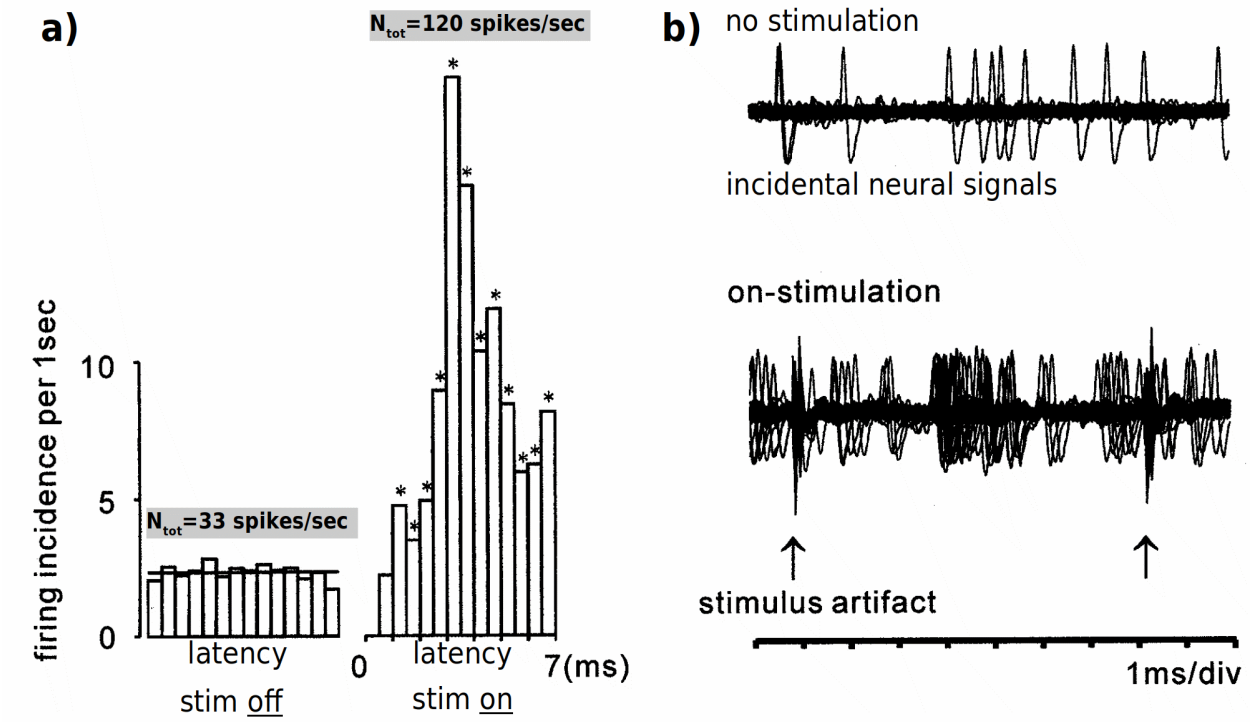

Figure 2-4. Variance of latency between stimulus and neural response.
(a) When the stimulation is off, the neural spikes recorded have a uniform distribution. When the stimulation is on, the latency of neural responses has a non-uniform probability distribution with a clearly defined mean and variance. (b) the same idea is illustrated in time domain by overlapping the stimulation frames. Adopted from [19].

This also implies that the exact timing of the response with respect to the stimulus can vary from one instance to another (Figure 2-4). Since each type of neuron has an intrinsic time constant associated with their structure, the summation or subtraction between and internal or external stimulus does not require the two events to be precisely aligned in time. The neural response will follow the later of the two events. For each stimulus set to the threshold level, the latency of neural response will in part depend on the timing of a following incidental background action potential and will vary [19]. Many published works take advantage of this property when designing an artifact cancellation methodology [10], [18]–[20]. If the stimulus intensity is adjusted to significantly above the threshold, the response will be less dependent on additional intrinsic signals

and will sufficiently fire with a more deterministic latency. This is sometimes called a time-locked response. Both cases are accommodated within the two design phases of the proposed in this work.

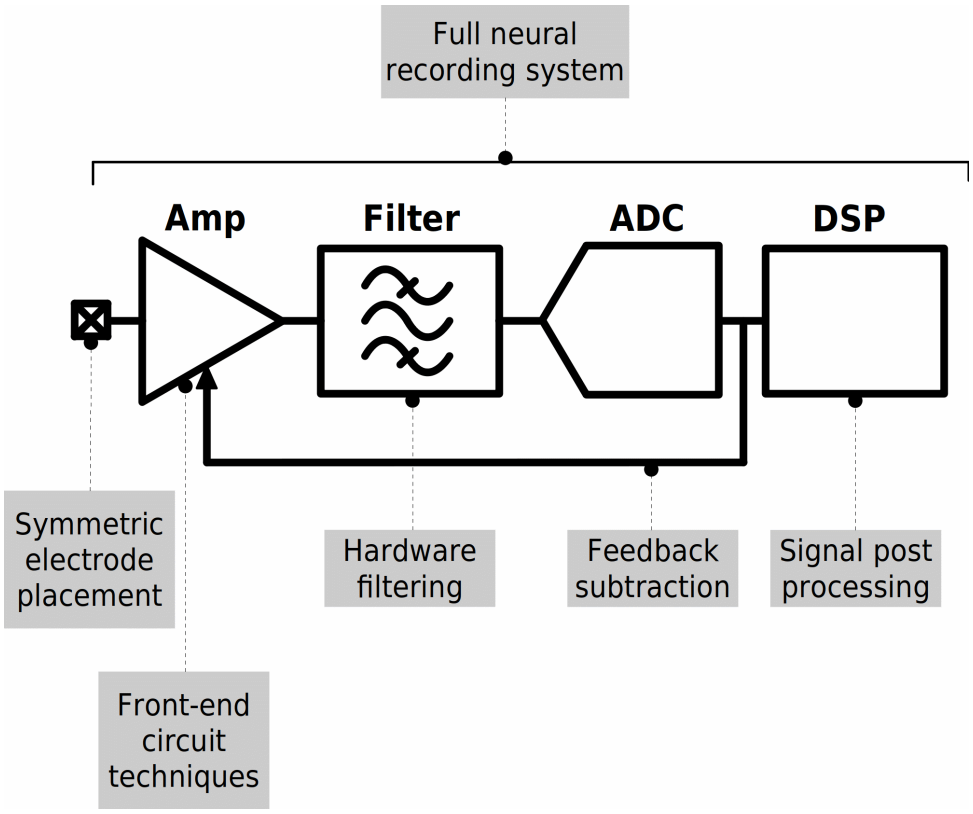

Figure 2-5. Design approaches to stimulation artifact cancellation.
Published works on artifact cancellation target innovations within one or multiple specific blocks of the standard neural recording chain or full system solutions. The blocks include a particular electrode arrangement, improved front-end recording circuits, filtering techniques, negative feedback that subtracts the incoming artifacts and novel signal post-processing as digital circuits or as software algorithm.

2.3 State of the Art Bidirectional Neural Interfaces

A large body of work has been published for removing stimulation artifact in bidirectional neural interfaces. Many relevant and notable works are reviewed here. The innovations proposed by the existing works can be grouped into three major categories based on the domain of the approach emphasized in the work: 1) innovations within front-end recording, 2) digital signal-

processing techniques, and 3) full system implementations. Each work has inherent advantages and limitations, while targeting a specific application. The limitations are commonly in the parameters of artifacts that can be removed using the proposed techniques. Here we discuss these limitations, generally and in the context of our target application (described in Section 2.4)

Figure 2-5 shows a block diagram of a standard neural recording chain, which includes a low-noise amplifier, a frequency filter, an analog-to-digital converter and a signal processing module. The recorded signal is processed through each of the blocks sequentially left to right. The low-noise-amplifier's function is to amplify the neural signal being recorded while minimizing the amount of noise, which is inherent to all hardware circuits, added to the signal during amplification. The hardware filter can usually include a high-pass filter, a low-pass filter and a 60Hz/50Hz notch filter. The former removes the mean and slow changes in the DC offset of the signal, which can otherwise limit the amount of headroom available in the remaining signal chain. The low-pass filter removes undesired high-frequency components, which can be coupled from digital circuits in the system as well as thermal noise added by electrode. The notch filter removes the noise from the power supply. The analog-to-digital converter digitizes the signal and requires the signal to be within a specific minimum and maximum limit to prevent any information loss. Finally, the digital signal processing block can include further filtering or signal conditioning, feature extraction such as spike sorting or biomarker identification, and signal compression. The DSP block can be implemented on the recording device as a set of digital circuits, or as a software code on the computer after the signal has been received and recorded.

The published state-of-the-art blocks in artifact cancellation include works that integrate their methodology into each of the listed blocks in the recording chain. Additionally, artifact rejection can be aided by a specific electrode arrangement, and by providing a feedback loop that

partially subtracts incoming artifacts. The following subsections survey the most notable works in this relevant and still not fully resolved design space.

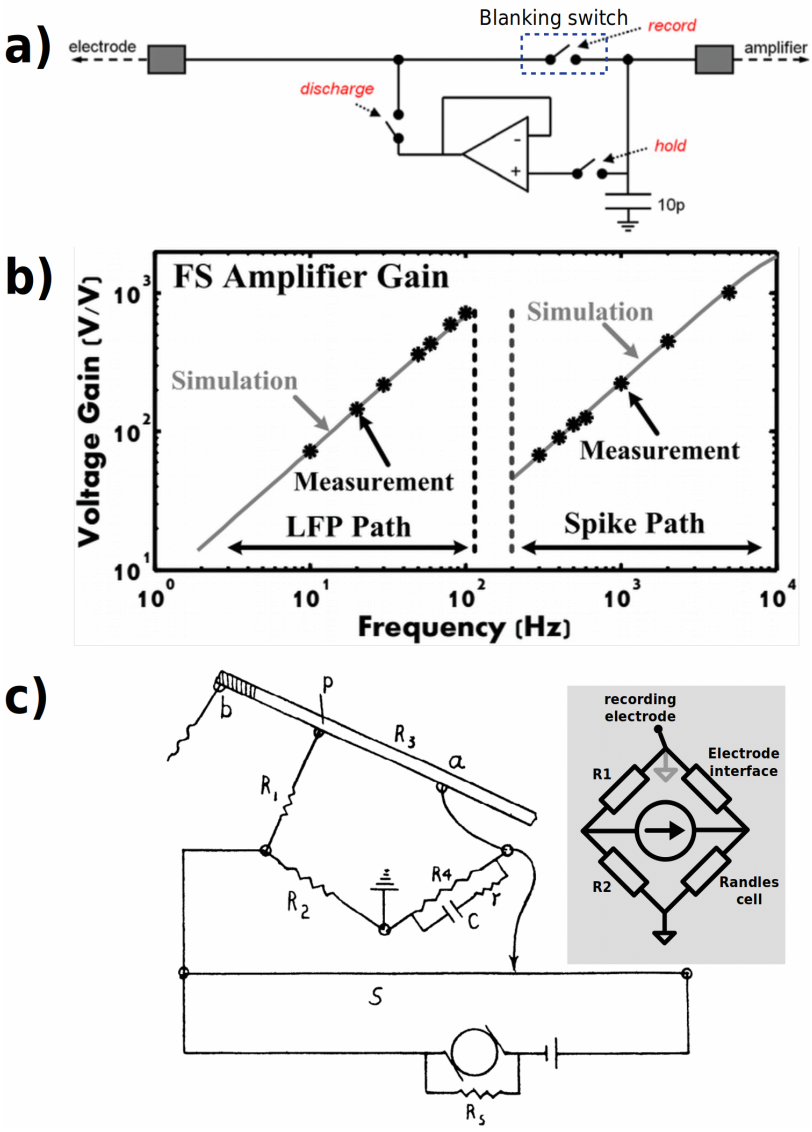

Figure 2-6. Three notable artifact cancellation works using front-end circuit designs.
They share a common goal: to prevent amplifier saturation. a) Amplifier blanking in [10] disconnects the amplifier from the electrode during the time of stimulation. b) Frequency shaping in [21] provides lower gain for low frequency signals, such as motion artifact or long pulse width stimulation artifact. c) A historic account [11] uses Wheatstone bridge to balance the electrodes to a virtual zero and record an action potential with less artifact distortion.

2.3.1 Front-end Circuit Solutions to Stimulation Artifact

Novel front-end design techniques which address stimulation artifacts by circuit design are proposed in notable works [10], [11], [21]–[23]. Work [10] utilizes a combination of methods in their approach, one of which is the amplifier blanking (Figure 2-1 (a)). Blanking disconnects the amplifier from the input during an undesired event such as a stimulation artifact. The amplifier is connected back to the input after the event has passed. Here, the amplifier's previous state is stored on a capacitor such that it can be returned to this state post-blanking with minimal start-up time. Still the main downsides of blanking are the fact that the input signals are completely lost during the disconnect and that the amplifier take some additional time to get back to normal recording state after the blanking event. The work demonstrates an ability to record neural responses on all electrodes including the site of stimulation, which is the most stringent case (Section 2.1.2). But the stimulation current used in the work is on the order of 0.1-1uA. This current is relatively small compared to other common in-vivo neural interface applications [13] and takes advantage of the correspondingly smaller artifact. Also, the quality of the data on that electrode is neither displayed nor analyzed. Extracted retinal ganglion cells are stimulated for the ex-vivo testing.

Another blanking design in [24] employs this approach and demonstrates a neural amplifier that takes 1 ms to recover to a normal recording state after completion of the stimulus event. In comparison, a neuron action potential can be evoked as early as 100 μs from the onset of the stimulus [25] and end in under 1 ms, prior to amplifier recovery. In addition, blanking does not accommodate deep brain stimulation (DBS) protocols, which commonly use high frequency pulse trains [12]. During this high-repetition rate stimulation, a neural response induced by one pulse may be obscured by the following pulse. Yet, artifact-free neural recording during DBS is critical to understand its underlying mechanisms and to design closed-loop DBS prosthetics [7].

Work [21] instead uses a frequency shaping circuit which adjusts the amplifier gain to be lower for lower frequencies and higher for higher frequency signals (Figure 2-1 (b)). This allows neural spikes to have a larger amplification factor than a slow-moving artifact. The technique is effective only for a stimulation protocol which uses wide slow rising pulses for stimulation, which is not common. This technique is most suitable for motion artifact tolerance, as motion artifacts waveforms follow a much slower time scale than the action potentials of a neuron.

Work [22] uses a lower-gain amplifier to record 20 mV peak-to-peak signals along-side the neural spikes without saturation. One innovation includes reducing the recording noise despite the reduced gain. Similar performance is targeted with work [23], but achieving a 100 mV input range. The input ranges in these works are sufficient for recording far from the site of stimulation but would not suit same-electrode stimulation and recording or any case with artifacts larger than 100 mV. Finally, these works were not validated ex-vivo or in-vivo.

A commendable ex-vivo same electrode stimulation and recording was demonstrated in a historical account in 1927 publication [11]. The approach used a Wheatstone bridge in which the branch connected to the axon with a stimulation artifact was balanced with the artifact created on a replica Randles cell created with resistors and a capacitor to match the electrode interface with the neuron (Figure 2-1 (c)). The arrangement created a virtual ground at the recording node with respect to the artifact. The virtual ground was only disturbed by an action potential which was recorded. The work impressively achieved the objective without access to modern tools such as an oscilloscope or robust neural amplifiers. Still this approach is sensitive to matching between the replica Randles cell with the actual electrode-tissue interface under test. The match was sufficient to cancel a small 8 mV artifact, but will not precise enough to precisely cancel large stimulation

artifacts in many other recording scenarios, such as the application targeted for this design (Section 2.4).

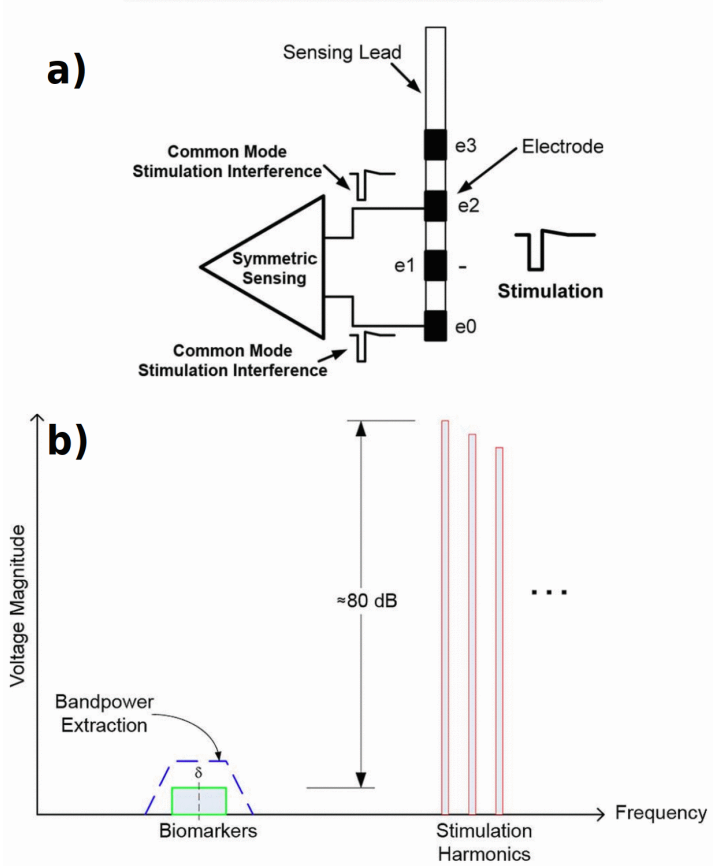

Figure 2-7. Metronic Inc's Activa RC+S device [12].
a) It reduces artifact by constraining the electrode placement to a symmetric bipolar recording around the artifact injection locus. b) Additionally, a hardware and software filter are proposed, as the biomarkers of interest are within LFP band, while stimulation is narrow pulses with high frequency content.

A popular front-end approach to cancelling artifacts is commercialized as the device [12] by Medtronic plc. This device requires a symmetric arrangement of the recording electrodes around the stimulating one, such that the artifact would be common to both recording electrodes which will subtract the signal at the amplifier (Figure 2-7). The neural signals are expected to have no symmetry and thus would remain. As perfect symmetry won't be achieved, the design also uses aggressive filtering in the signal chain to remove a high frequency stimulation artifact from the

low frequency local field potential recordings (LFP). This suits the specific DBS protocol for which this device is intended. But neural responses that overlap in the frequency spectrum with the stimulus waveforms become distorted or suppressed by such analog filtering method [22], and the constrained electrode placement does not generalize to other applications.

Other circuit design methods published in [24], [26]–[30] are extensions or variations of approaches described above. All together all circuit approaches share the following limitations. Their tolerated maximum artifact amplitude is small and does not generalize to all applications, including the target application in this thesis. They lack validation in-vivo or ex-vivo. Finally, they are only designed to tolerate the artifact to avoid recording loss but are not capable of removing it to reveal the underlying neural signals.

2.3.2 Back-end Signal Processing Solutions to Stimulation Artifact

In contrast, designs in the signal processing domain focus on removing the artifact from the signals. Most popular approach in this domain is the Principle Component Analysis (PCA). This technique is used in statistical analysis of high dimensional data sets to find key features which can be represented in new, smaller set of dimensions. A new set of axes is represented as vectors within the old dimensions [31], and the data is then projected onto the new axes, thus reducing the original dimension. When applied to time domain signals, each time sample of the signal is treated as a dimension. The new axes are then a set of fixed waveforms – Principle Components (PCs) – spanning the full length of time of the recordings under analysis. PCA chooses these waveforms as bases which maximally differentiate among signals at each channel. Since the artifact is commonly present at different amplitude levels on multiple channels and is larger and more pronounced than the neural signal, PCA is likely to choose the artifact waveforms as the most significant bases which differentiate the signals on different channels.

This is explored in work [16], where the PCs are chosen carefully across multiple channels and multiple experiment trials to find an accurate template of the artifact and subtract it from the recordings. The approach is successfully demonstrated on previously recorded in-vivo data. Additionally, manuscript [32] demonstrates a real-time implementation of this technique for closed-loop neural-interface applications. The shortcoming of these works in the context of general artifact cancellation, is that they assume that the artifacts are small enough that the amplifier saturation is not a risk. If the PCA technique is paired with one of the circuit solutions discussed above, additional challenges are likely to surface and require further work, as is presented in detail in Chapter 4 of this thesis.

Yet another common digital post-processing technique which can successfully remove the stimulation artifact is described in [19], [20] as template averaging. The method relies on the varying latency of neural responses to stimulation, as described in Section 2.2.2 and Figure 2-4. When the artifact frames are overlaid as an array, and a template is constructed from their average, the artifact will be clearly defined within the template while the neural signals within the frames will be attenuated. The attenuation of the neural signal component depends on the degree to which their latency varies. Due to this condition the method is best applied to a protocol with stimulation intensity set to near-threshold levels, as discussed in Section 2.2.2. Finally, the method shares the same limitation as above: it assumes that the artifact is small, and amplifiers were not saturated during the recording.

The work [18] uses a subthreshold artifact, which contains no neural response, to build a template for the suprathreshold (therapeutic level) artifact, which does contain the neural response of interest. The template is built by scaling, and the scaling constant is calculated using an adaptive

filter which is trained by a series of subthreshold artifact waveforms at different levels, labeled by their stimulus current.

Work [33] implements a signal processing algorithm on a chip using digital circuits. The algorithm uses an artifact on one channel and scales it to cancel the artifact on another channel. The scaling here is incrementally performed by a loop which adjusts the value until it reaches a least square error minimum. The demonstration of the algorithm with prerecorded neural signal and in-vitro stimulation in saline shows that the scaling loop has a relaxed precision requirement as the artifacts are not much larger than the neural signal. They also are high-frequency and span a couple of sample points while the neural signal recovered by this method is a slower moving LFP waveform. The method is thus specific to this and closely related applications.

Additionally, other recent work has used digital post-processing [7], [34]–[37] to remove artifacts. Many are variations of methods listed above, using curve fitting or learning a template to subtract the artifact. Just as with the other post-processing methods, to generalize them to a wider set of applications, they must be combined with front-end circuit solutions which prevents amplifier saturation.

2.3.3 Complete System Solutions to Stimulation Artifact

Complete system solutions, which remove the stimulation artifact from neural recordings, have been shown in recent works. They achieve their objective by integrating front-end circuit solutions with back-end signal processing. In work [38], the team adapted their previous design of front-end circuits which can theoretically tolerate 100 mVp-p artifacts [23], and their digital back-end capable of artifact removal [33], integrated into one package. Their in-vitro testing (Figure 2-8) demonstrated an ability to suppress ~45 mV artifacts down to ~5mV residual, showing a 10x reduction, while simultaneously recording a 3mV peak-to-peak prerecorded neural signal injected

into the saline. While the work is impressive in integrating advanced stimulator functions with the recording circuits onto an implantable packaging, the artifact rejection methodology by itself would not suffice for applications where the artifact exceeds 100 mV amplitudes and where the neural signals that need to be recovered are on the order of 100 µV in amplitudes, requiring a >1000x artifact suppression.

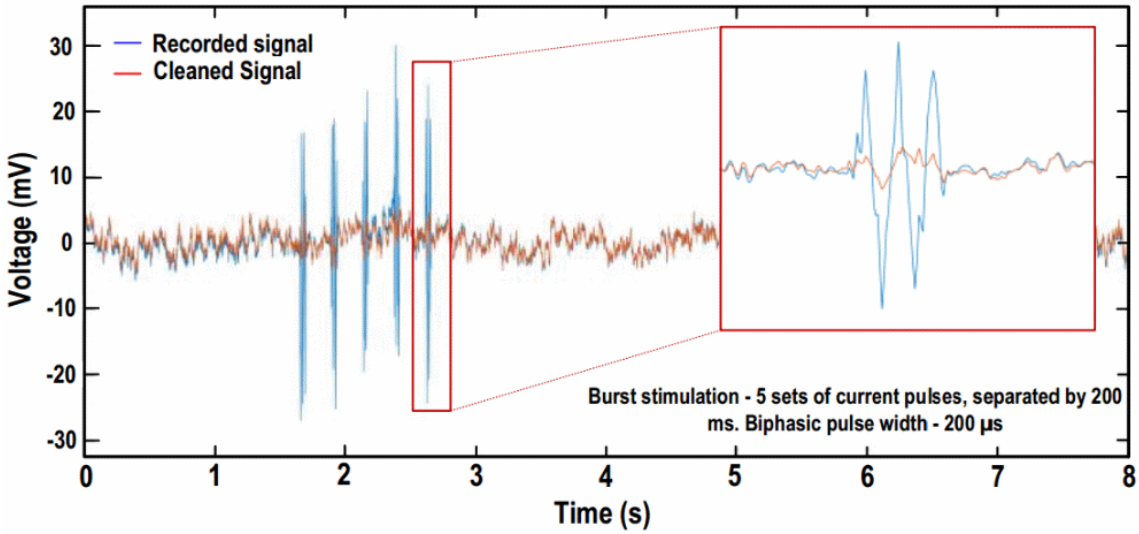

Figure 2-8. Notable artifact cancellation system published in [38].
Work [38] demonstrates their artifact cancellation in a saline. Artifact is reduced from ~45mV to <1mV. Narrow pulses which have a high frequency content are used for in-vitro test.

Work [39] integrated a novel schema into the recording circuits which suppresses artifact by making an approximation and subtracting it through a real-time feedback loop. The loop takes multiple artifacts to eventually converge to an approximate artifact template with enough precision to prevent the amplifier saturation (Figure 2-9 (a)). The back-end digital circuits are tasked to run the convergence process efficiently using a simplified search algorithm. The precision of the artifact cancellation in this work is not clearly quantified with respect to the expected signals of target application. The design nevertheless was tested in one example in-vivo during stimulation and recording of a rat hippocampus. The stimulation artifact presented at the input of the system was ~3.5 mV while the recorded signal was ~0.5 mV, equivalent to a 7x ratio. The artifact

amplitude is small as the recording is performed far from the site of stimulation. The design showed convergence and eventual suppression of the artifact, which reveals the neural signal, although specific features evoked by stimulation were not pointed out (Figure 2-9 (b)).

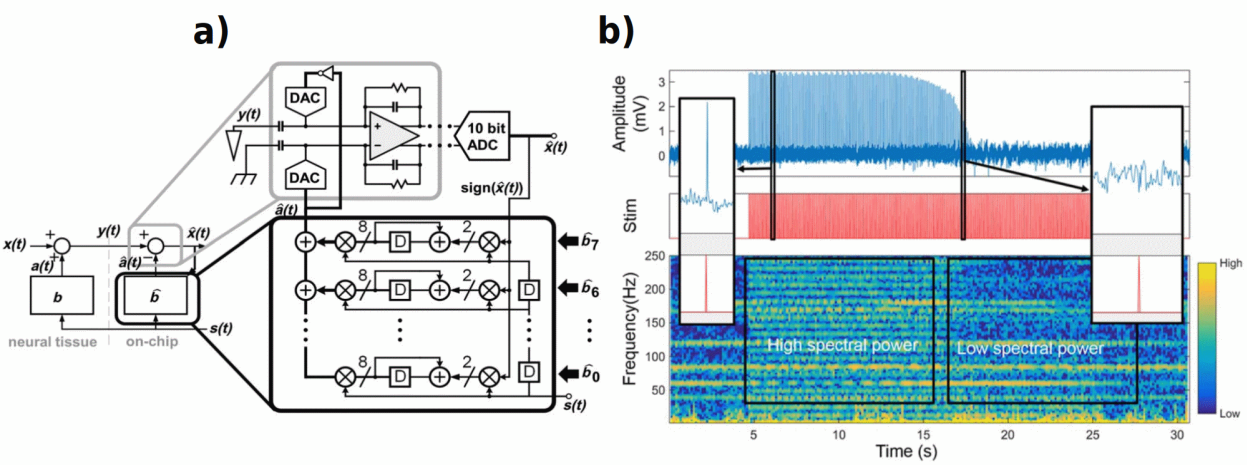

Figure 2-9. Notable artifact cancellation system published in [39].
Work [39] uses a feedback loop to converge and subtract the artifact. b) In-vivo testing cancels an artifact with amplitude of 3.5mV to reveal a 0.5 mV neural signal. Top blue trace shows gradual convergence of the system as it suppresses the artifacts.

Finally, [40] reports another schema which uses a feedback to subtract the artifact. But unlike the above work, the feedback algorithm previously published in [41] is designed to subtract a value for every sample signal recorded such that the resulting difference is always within the amplifier input range, which prevents saturation (Figure 2-10 (a)). The artifact is never learned, nor must it converge, and is instead suppressed from the very first instance. The tradeoffs made by the authors include limiting the sampling rate of the signal to accommodate the time required for the suppression mechanism and to reduce the design complexity. The high-frequency artifact thus spans just one or two sample points within the recorded signal, while the low-frequency neural signal under observation spans a higher number of samples. The back-end signal processing in this design overwrites the artifact sample point(s) by an interpolated value between previous and next data point in the signal. The design has a theoretical artifact tolerance range of up to 100 mVp-p.

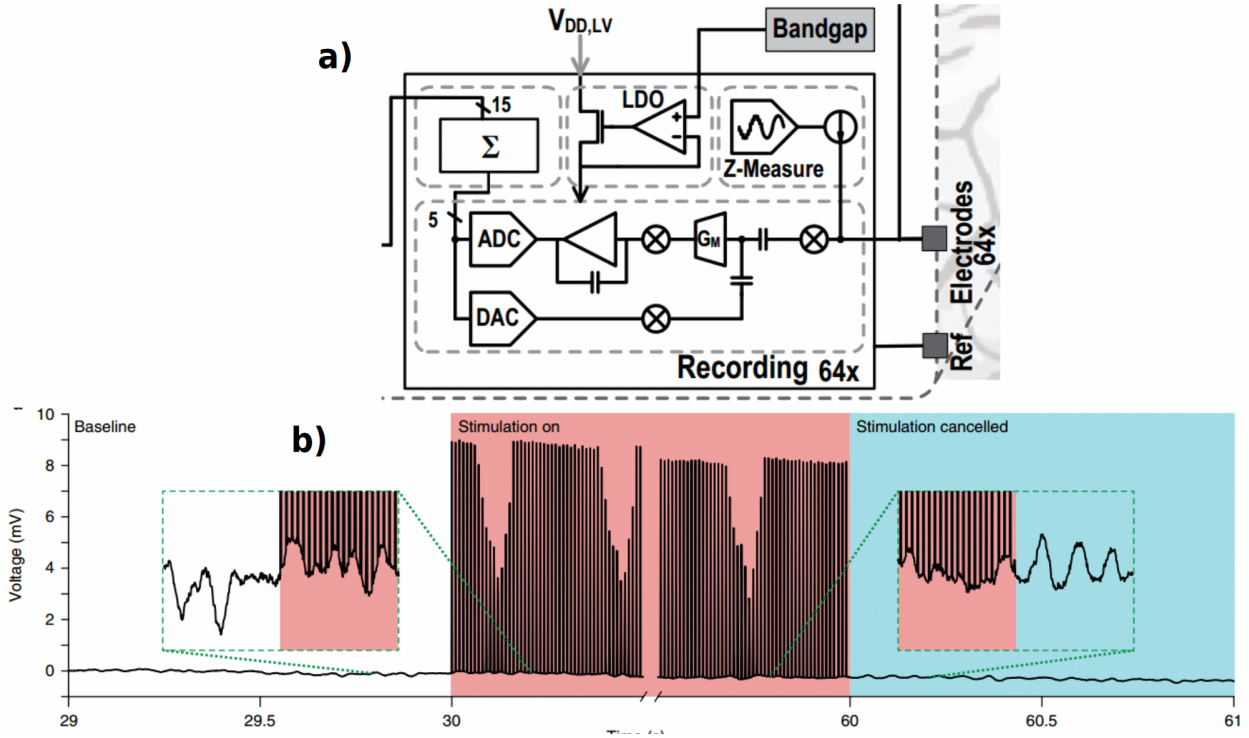

Figure 2-10. Notable artifact cancellation system published in [40].
a) Work [40] suppresses artifact using instantaneous feedback subtraction at each sample. Digital algorithm finally removes the suppressed artifact sample and interpolates a new point instead to erase the artifact. b) ~10 mV artifact is recorded and suppressed in-vivo.

The implemented device is demonstrated in-vivo and records LFPs in the bandwidth <200Hz, while effectively rejecting artifacts that are <10mV in size at 125 µs or 62.5 µs pulse width (Figure 2-10 (b)). The separation between artifacts and observed neural signals in frequency domain is essential to the success of this design, but as stated previously, does not generalize to other applications, such as spike recordings.

2.3.4 Remaining Knowledge Gap in Cancellation of Stimulation Artifacts

Significant progress has been made by the state-of-the-art designs in resolving the difficult problem of stimulation artifact during simultaneous stimulation and recording. Most effective designs utilize both the front-end circuitry as well as the digital signal processing algorithms in a full system solution. Still, the notable state-of-the-art works are confined to recording low-frequency neural signals during narrow pulse stimulation with high frequency content.

Additionally, the designs claim theoretical maximum artifact size of 100 mV or less and demonstrate their work with amplitudes well under this limit. Report [10] is the only recent work which claimed to be able to stimulate and record on the same electrode, but with stimulation levels so small that they result in an artifact sized a few mV. Finally, some of the state-of-the-art works lack demonstration in-vivo or ex-vivo with live tissue and real neural signals.

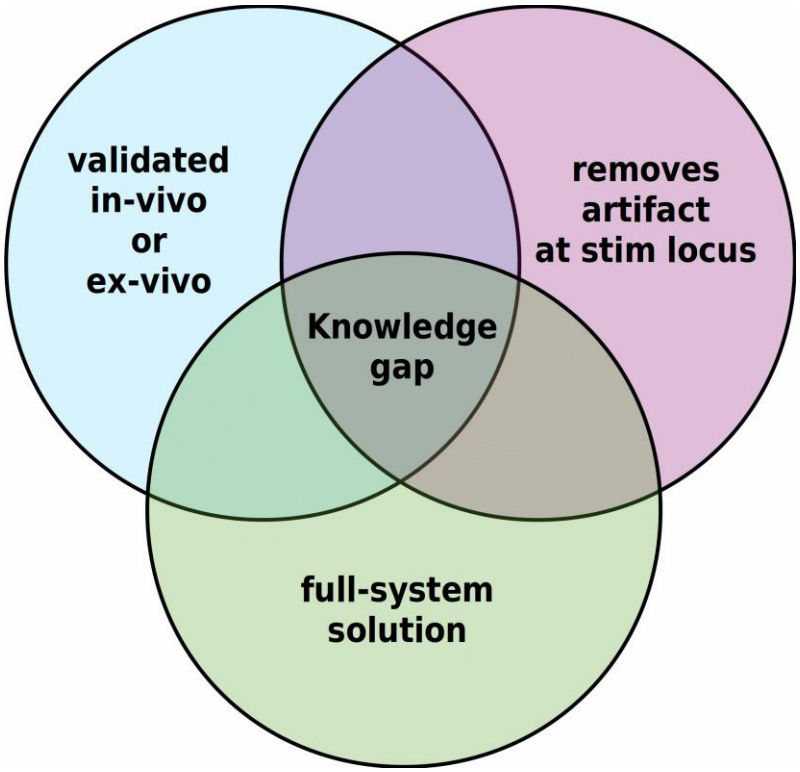

Figure 2-11. Knowledge gap within artifact cancellation research space.
A knowledge gap still exists among previously demonstrated state-of-the-art artifact cancellation works. This gap is addressed by this thesis and related reports published by the author.

Thus, reports [1], [42] by this author, further expanded in this thesis, fulfill an otherwise unaddressed knowledge gap (Figure 2-11): a full system design validated in-vivo, able to cancel large stimulation artifacts arising at all recording sites, including the locus of stimulation.

2.4 Target Application: Study of Neural Networks of The Spinal Cord

This work was motivated by challenges existing in research of rehabilitation protocols for spinal-cord injury. SCI is defined as damage to the spinal cord that leads to permanent or temporary neurologic deficit [43]. Although SCI interrupts the cerebrospinal pathway, key planning coordination, and effector centers above and below the injured spinal segment remain intact [44]. Additionally, the cerebrospinal interrupts in the SCI are rarely complete, sparing tissue bridges that might support functional recovery. The interrupt nevertheless causes loss of volitional control of motor function and partial or complete paralysis by cutting off the supraspinal input (Figure 2-12 (a)). The underlying objective of the rehabilitation is to promote a highly functional state which causes the sensory motor pathways aid in enabling plastic changes. These changes are promoted by these pathways, which then route sensory information to the remaining planning and effector sections of the spinal cord and become a source of control of movement. This rehabilitation process has been enabled by a safe and effective tonic electrical stimulation applied epidurally over the dorsal aspect of lumbosacral segments in paralyzed animal models, which effectively restored hindlimb movements (Figure 2-12 (b), left). These movements of stepping and standing are produced without the need of supraspinal input from the test subjects as long as the epidural stimulation is present [45].

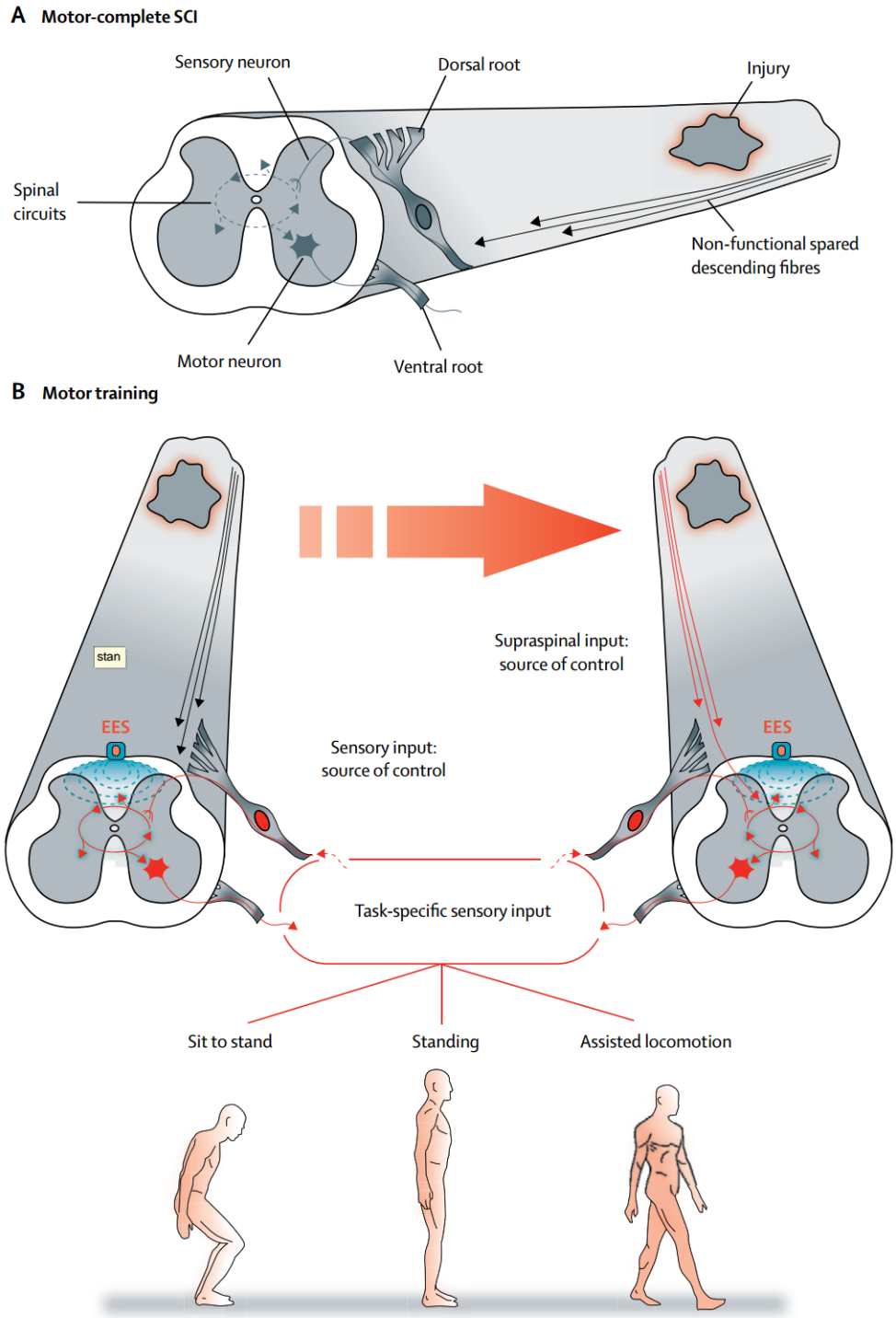

Figure 2-12. Physiology behind rehabilitation from spinal cord injury.
(a) A cerebrospinal interrupt still contains axonal tissue bridge fibers that can be used to restore motor function with rehabilitation. (b) Electrical epidural stimulation has been shown to be effective in recovery of motor functions in SCI patients. Left: stimulation enables motor function in response to sensory input from legs. Right: epidural stimulation promotes plasticity in neural tissue and helps to reestablish a connection along the spinal cord across the site of injury. Adopted from [45].

This approach was also translated to a viable application for human beings with motor complete SCI by the team [46]. The additional discovery was that after several months of continuously applying these methods on the human subject, the therapy has promoted the plasticity of axonal projections that presumably were spared in the injury and thus generated new connections and restored previously lost supraspinal input to the lumbosacral segments. This allowed the subject to regain conscious control of join-specific movements of the leg (Figure 2-12 (b), right).

The success of these therapies is driven by the regeneration and plastic remodeling of the neuronal circuitries [44]. The exact mechanisms are not fully understood, motivating further research into new parameters for the epidural stimulation protocols as well as analysis of fundamental changes in neural networks in response to the therapy.

To that end, we have contributed to [13] in exploring novel techniques for spinal cord modulation. The explored techniques aimed to enhance the excitability of the spinal cord and increase of connectivity from spinal cord to motor output of animal models with and without spinal cord injury. To apply the neuromodulation protocols, we have employed our custom flexible epidural Micro Electrode Array (MEA) [47] to the epidural space of animal test subjects. A set of electrical stimulation signals hypothesized to be more effective than the traditional protocols. Their efficacy was evaluated by administering the protocols while assessing changes in the connectivity between the spinal cord and motor responses of limb muscles (Figure 2-13). The connectivity was measured by recording EMG signals in response to spinal cord stimulation.

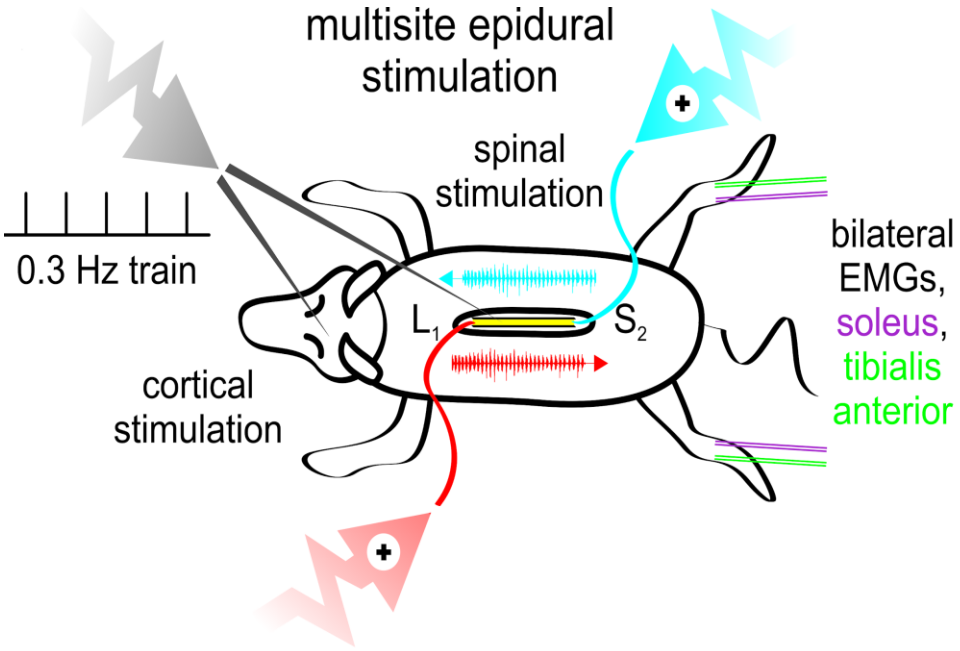

Figure 2-13. Our work in spinal cord neuromodulation.
We have contributed to the study [13] of spinal cord neuromodulation on animal models with and without spinal cord injury measures changes in the excitability of synaptic pathways between spinal cord and muscles of hind limbs. The measurements are EMG signals recorded in response to stimulation applied to the spinal cord through an implanted epidural microelectrode array. Adopted from [13].

In addition to this approach, pilot recordings were also captured from the spinal cord dura itself by stimulating and recording on the same MEA. These recordings contained the spinal cord evoked potentials (EPs) which were elicited by the electrical stimulation. The EPs are hypothesized to be significant biomarkers intended to directly assess the neural networks across the length of the spinal cord. Specific parameters, such as the speed and direction of propagation of the potentials across the site of injury can be used as indicators change in the network during rehabilitation protocols tested on SCI animal models.

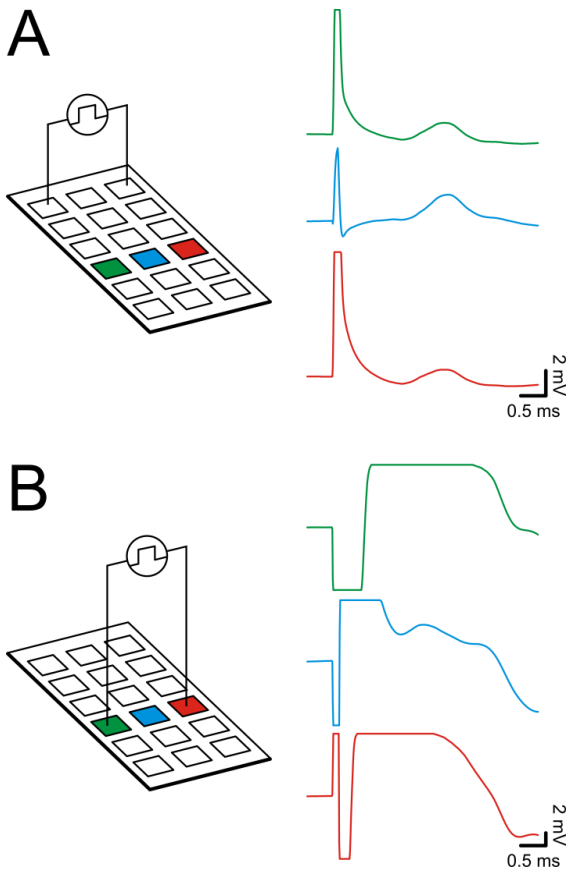

Figure 2-14. Epidural MEA was implanted into an animal model.
Evoked Potentials from the spinal cord were recorded during electrical stimulation applied to the MEA. (a) Stimulation artifact greatly distorts the details of the EPs when recording from non-stimulating electrodes. (b) Recording shows complete signal loss when recording from stimulating electrodes.

Yet, the recorded EPs are contaminated with relatively large stimulation artifacts. This occurs because a significant stimulation current applied in the protocols is large given the electrode size and impedance, and there is a proximity among all electrodes on the MEA used for recording and stimulation. The stimulation artifacts greatly obscure the evoked responses of interest (Figure 2-14 (a)). Recordings at the stimulating electrodes, show complete signal loss, rendering them useless for our intended measurements (Figure 2-14 (b)).

This existing challenge motivates a design of a neural interface capable of recording evoked responses during stimulation at or close to the stimulation site in the presence of large interfering stimulation artifacts. Such design is presented in this thesis.

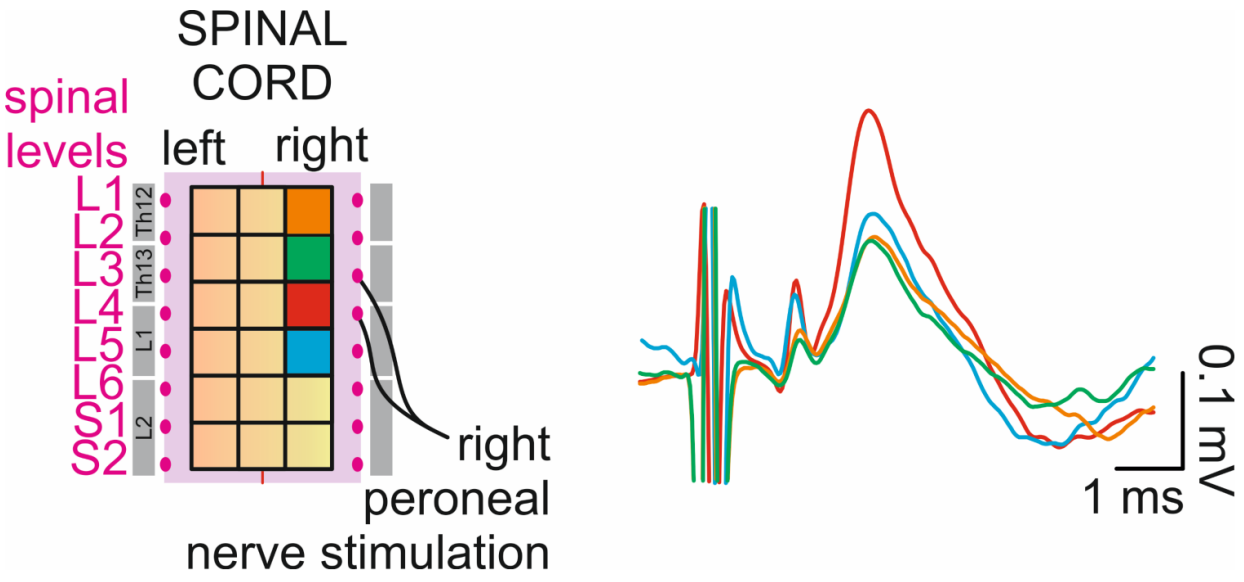

Figure 2-15. Intact EPs collected from the spinal cord.
The intact EPs with significantly less contamination are recorded epidurally while stimulating the peroneal nerve in a rat model. These EP waveforms were used in in-vitro testing of the Phase II design of the proposed system.

In order to observe the intact evoked potentials on the spinal cord, we have recorded the epidural MEA electrodes while stimulating the peroneal nerve in a rat model. The spinal cord neural responses show a significantly smaller levels of contamination (Figure 2-15). This is due to the greater distance between the site of stimulation (here in the peripheral nerve) and the site of recording. These in-vivo waveforms were injected into the saline to emulate the EPs of spinal cord during the validation of the final design of our proposed artifact cancellation system.

Chapter 3

Phase I: Single-channel Artifact Cancellation Design

3.1 System Design

We have designed a solution, which cancels stimulation artifact while recording on the stimulation electrode where the signal contamination is strongest, illustrated in Figure 3-1. A current stimulator injects pulses into the stimulation site of a neural tissue (intra or extracellular), which generates a neural response and a large stimulus artifact on the same electrode. The resulting signal is processed by the artifact cancellation device where the artifact is suppressed in real-time to allow uninterrupted recording of neural responses. The device output is then streamed into a custom software application driven by a graphical user interface (GUI). The software algorithm completes the processing on-line and immediately presents the underlying neural signals to the user as a live plot.

The designed mechanism which cancels stimulus artifact followed two main requirements. First, the input voltage range of the recording circuitry must be sufficiently high to accommodate and suppress large stimulation artifacts, when recording near or at the stimulation site. This requires partial artifact removal at the input, before signal amplification, to avoid amplifier saturation and thus preserve continuous neural recording with high fidelity. Second, the system must have a sufficiently high SNR to record clean neural signals, which are multiple orders of magnitude smaller than the superimposed artifact. The noise must be carefully controlled, as artifact suppressing circuits prior to amplification will add noise directly to the recording.

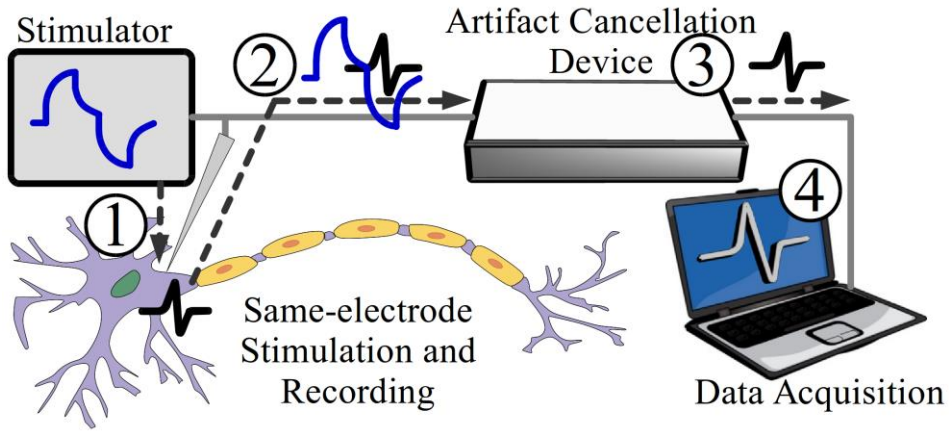

Figure 3-1. Overview of the design of our system.
1. A stimulus is injected into the cell and generates an artifact with a neural response. 2. The neural response is superimposed on the stimulus artifact waveform. 3. An artifact cancellation device suppresses the artifact and prevents amplifier saturation. 4. Software processing reveals the final neural signal without the stimulation artifact to the user.

We have additionally imposed a third requirement for this design (this was dropped in the phase II design to further focus on the targeted application): the system must recover neural signals online. This accommodates closed-loop operation for any devices that need to continuously assess neural responses to adjust stimulation parameters in real-time. Such feature can be used in experiments which intend to disrupt neural signaling based on presence of a specific activity, to investigate an isolated dynamic of a network in a neural tissue. It is also useful for investigation of closed-loop therapies for eventual design as neural implants.

The design methodology we have conceived satisfies the above principles by a solution that combines a hardware circuit topology and a software design, which together allows an artifact-free neural recording in real-time.

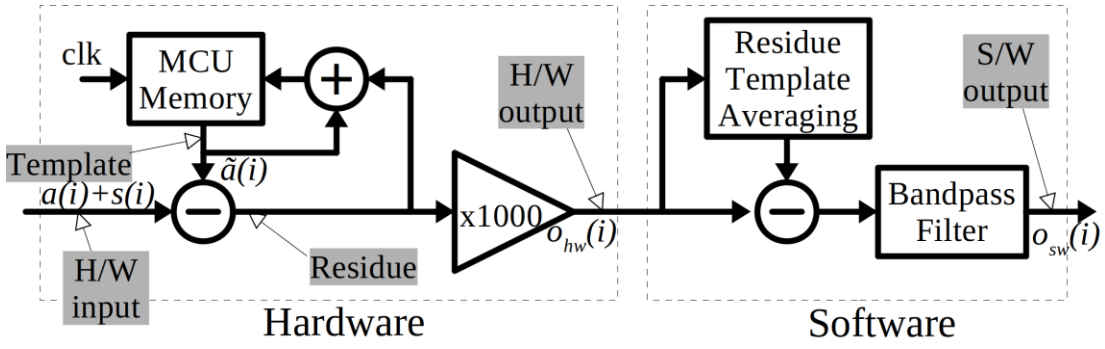

Figure 3-2. Block diagram of the system's H/W and S/W architectures.

3.1.1 System Architecture

Figure 3-2 shows the basic functional diagram of the proposed system divided into hardware and software modules. The hardware module consists of the analog amplifiers and filters, microcontroller unit (MCU) with custom firmware, analog-to-digital converter (ADC), and digital-to-analog converter (DAC) that together constitute the artifact cancellation device. The Data Acquisition Card (DAQ) relays the hardware output to the software module. The software module consists of the GUI and template-averaging algorithm. Both module designs take advantage of the fact that periodically incoming stimulus artifacts are relatively similar in shape and amplitude, since neural stimulation is commonly performed by a periodic train of pulses with fixed stimulus pulse amplitudes, widths, and inter-pulse delays. Any changes in the artifact waveform that happen due to naturally occurring electrode-tissue impedance drift during stimulation are accommodated in the hardware and software modules as well. The detailed functionality of each module is described below.

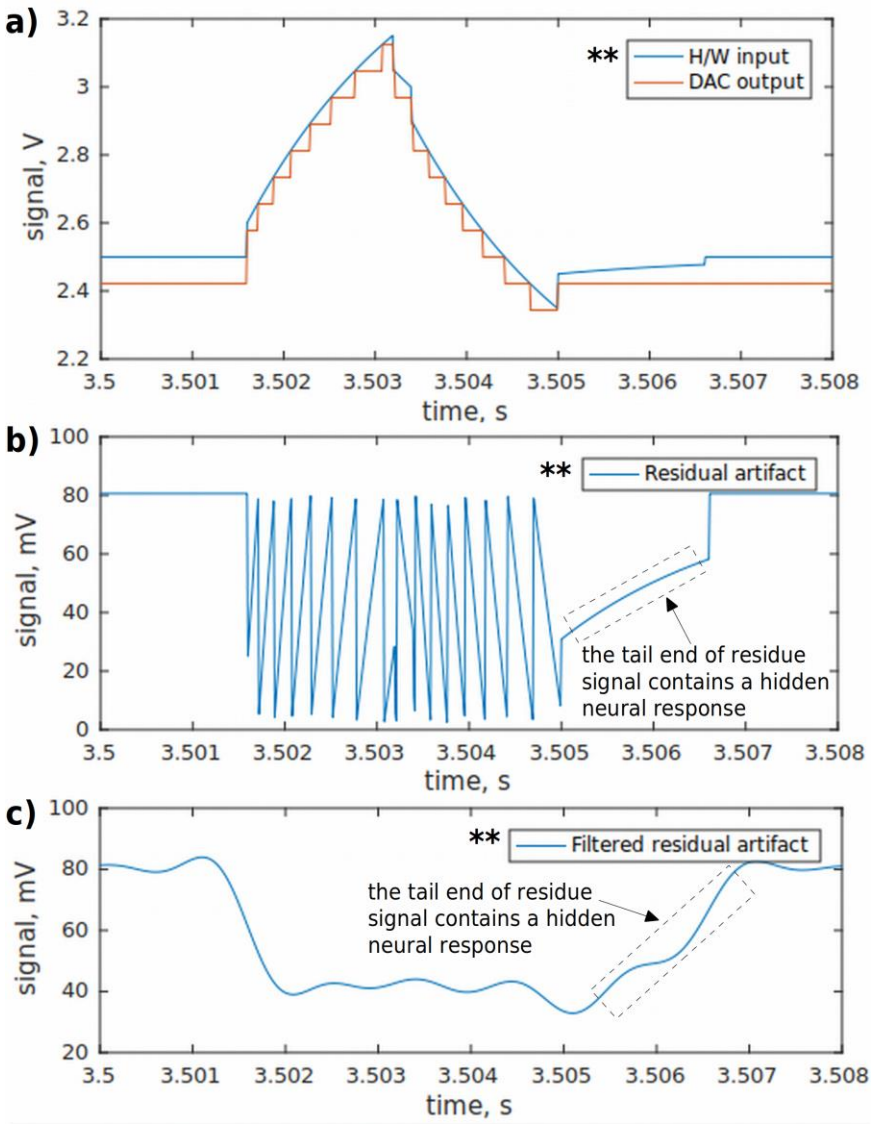

** Signals are not displayed to scale.

Figure 3-3. The HW-M prevents amplifier saturation.
This is done by suppressing the stimulation artifact in the signal while recording it. a) The artifact (blue) is approximated by the HW-M's feedback loop (orange). b) The loop has limited precision and leaves a residue post subtraction. The residue amplitude is a function of the precision, and only must be small enough to be within the gain amplifier's input compliance voltage. The tails of the residue contain the neural signal. c) The residue is filtered to remove the digital switching noise created by the HW-M's feedback loop. The final filtered residue is then recorded and processed by the SW-M to remove the residue and extract the underlying neural signal.

The hardware module design reduces the artifact amplitude to meet the compliance requirement of the back-end amplifier without altering the neural signals. This is accomplished through an iterative hardware loop (Figure 3-2). The loop consists of first storing the artifact as an

initial template, then iteratively updating the template based on measured differences until the incoming artifact and stored template converge within the resolution of the hardware components. The final template is then subtracted from all following artifacts, and the result is amplified. The output of the hardware module at i_{th} stimulation instance $o_{hw}(i)$, after convergence ($i > c$), can be described as:

$$o_{hw}(i) = \big(a(i) + s(i) - \tilde{a}(c)\big) \times G = (\Delta a(i) + s(i)) \times G, \qquad i > c \tag{2-1}$$

where $a(i)$ is any single artifact occurring after convergence, $s(i)$ is the neural signal underlying the artifact, $\tilde{a}(c)$ is the digitized artifact template converged at iteration c, G is the output amplifier gain, and $\Delta a(i)$ is the residual between the incoming artifact and stored template ($\Delta a(i) = a(i) - \tilde{a}(c)$). The term $s(i) \times G$ in (1) is equivalent to amplifying a neural signal by a basic recording amplifier without the stimulus artifact and is the component that is preserved and recovered in the later stages of the software signal processing. Each term in the equation 2-1 represents a time segment spanning the duration of the artifact instance. The residual artifact, $\Delta a(i)$, can be much larger than $s(i)$ without information loss as long as the amplified sum $o_{hw}(i)$ is lower than the saturation voltage limits, V_{hw_sat}. Thus, hardware cancellation only requires that signal path accommodates:

$$\Delta a(i) \times G \ < V_{hw\_sat}, \tag{2-2}$$

assuming $\Delta a(i) \gg s(i)$, which is typically the case. For a fixed gain G, the maximum tolerated $\Delta a(i)$ value defines the precision requirement for hardware components implementing acquisition and subtraction of the artifact (mainly ADC and DAC). The precision requirement above can be met with modest resolution data converters, reducing the complexity of the design implementation. An additional benefit is that a modest resolution data converter will not capture

and subtract the key features of the neural signal alongside the artifact. The signals of the HW-M's feedback loop are depicted in Figure 3-3.

In contrast, a commercial front-end IC with a high-resolution ADC [48] could be used to accommodate a large stimulation artifact in simultaneous neural signal recording. However, a large section of the ADC's highest weighted bits that represent the artifact will be discarded in post-processing, thereby reducing the available bits for the neural signal capture. For example, the front-end IC with 5.25 V supply and 24-bit ADC [48] would use 13 highest weighted bits to capture a 5 V artifact for subsequent removal in software domain, and only use the remaining 11 bits for digitizing a 0.5 mV neural signal. Such a design is inefficient and sub-optimal to implement in miniature SoC neural implants, where space and power are limited.

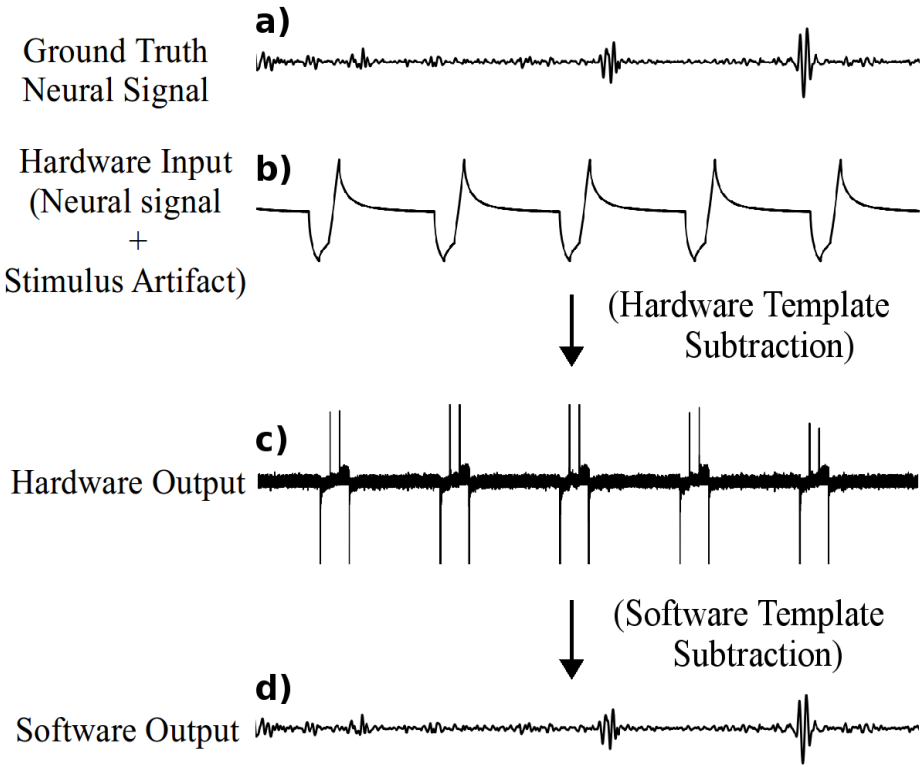

Figure 3-4. Simulations based on system equations.
Simulations illustrate signal transformation from contamination by a 1.2 V artifact to recovered neural response with 100 µV signal waveforms.

The software module in Figure 3-2 eliminates residual artifacts from the hardware module output via generating and subtracting the software template. This template is generated by averaging multiple hardware output instances $o_{hw}(i)$. Each instance contains a residual stimulation-artifact waveform $\Delta a(i)$ and an underlying neural signal segment $s(i)$. The residual artifact is stable and periodic after hardware convergence ($\Delta a(i) = \Delta a(j)$ for any $i, j > c$). The component $s(i)$ contains the incidental neural activity, which spans the duration of the artifact, and does not include the neural response, which occurs after the stimulation that caused it. The neural response after the artifact is freely passed to the output as the system prevents any amplifier saturation and signal loss. The incidental neural segment $s(i)$ underlying the artifact is uncorrelated to the stimulation and thus varies from one instance to another. Averaging this variance reduces $s(i)$ contribution below noise level (Section 3.3) but fully preserves the residual artifact component in the template [19]. The template is then subtracted from $o_{hw}(i)$ at each stimulation event to uncover the underlying neural signal. Thus both, the underlying incidental signals and stimulation responses, are revealed at system's output. The output of the software module, $o_{sw}(i)$, can be described as:

$$o_{sw}(i) = o_{hw}(i) - \frac{1}{k}\sum_{j=i+1}^{i+k} o_{hw}(j)\,,\ i > c = o_{hw}(i) - \frac{1}{k}\sum_{j=i+1}^{i+k}\big(\Delta a(j) + s(j)\big) \times G \approx$$

$$\approx (\Delta a(i) + s(i)) \times G - (\Delta a(i) \times G) = s(i) \times G \qquad (2\text{-}3)$$

where the function $\frac{1}{k}\sum$ averages k stimulation periods of $o_{hw}(j)$. The number (k) of segments to average is determined by signal analysis in Section 3.3. Figure 3-4 illustrates the simulated input and output of the hardware and software modules during artifact cancellation. The signal a) is the ground truth neural signal. The signal b) is the system's input – the sum of a periodic stimulus artifact and a pre-recorded ground-truth neural signal. The neural signal amplitude is several orders of magnitude smaller than the artifact, thus the latter dominates the summed waveform. The signal

c) emulates the hardware module output – an amplified sum of the reduced residual artifacts and the neural responses, which meets the amplifier's input range. Finally, the signal d) represents the software module output, which contains the neural signal without the artifact.

3.1.2 System Specifications

The specifications of the artifact cancellation system in Table 3-1 are derived to: 1) cancel stimulus artifacts orders of magnitude greater than the underlying neural signal, and 2) preserve the integrity of the neural signals during the recovery process. The input compliance voltage range is determined by the expected maximum artifact amplitude. This amplitude is estimated using the Randles cell model equation of an electrode [15], for typical stimulation settings provided below.

Table 3-1. System Design Requirements.

Requirement Parameter	Value
Maximum Stimulus Artifact Amplitude	5 V
Minimum Neural Signal Amplitude	50 µV
Ratio: Max. Artifact to Min. Signal of Interest	100 dB
Maximum Gain	60 dB
Bandwidth of Signal Interest	1 Hz–10 kHz
Sampling Frequency	100 kHz

During rat cortex stimulation using a platinum ball electrode with 0.8 mm diameter and 50 µs pulses of 10 mA current [49], the artifact amplitude will be 4.99 V, as derived from [15] with Pt parameters from [50]. By the same token, intrafascicular sciatic nerve stimulation in cats using Utah electrode array with 0.005 mm^2 exposed platinum tips [51] and 200 µs pulses of 50 µA [52] results in artifact amplitude of 0.198 V. Finally, [53] characterizes a typical DBS stimulation in-vivo with safe stimulation currents and pulse widths, and records resulting voltage amplitudes. The resulting maximum artifact amplitude is 3.4 V. To accommodate all listed applications by the

proposed device, the input signal limit V_{hw_sat} is set to 5 V. This parameter also specifies the ADC and DAC full scale voltages.

On the other hand, extracellular action potential (AP) signal amplitude ranges 50-500 µV, while local field potentials (LFPs) have amplitudes 500 µV-5 mV [54]. The resulting ratio of the maximum artifact to minimum signal of interest is V_{hw_sat}/V_{sig_min} – is then 100,000 V/V, or 100 dB (20log scale). Additionally, to detect a 50 µV neural response with sufficient clarity, the noise must be 5-10x less. This is considered in the design of software algorithm in Section Software Module Implementation3.3 .

Analog signal gain of the system, G, is programmable between 100 V/V and 1000 V/V, (40-60 dB), where a larger 5 mV LFP signal can be amplified back to 5 V at maximum gain. Combining the maximum gain and the set specifications with equation 2-2, a requirement for the residual artifact amplitude is defined as $\Delta a(t) < 5$ mV at the hardware module's output. Recording bandwidth is set to frequency range from 1 Hz – 10 kHz for both AP and LFP signals [54].

3.2 Hardware Module Implementation

The design topologies for analog components, data converters and MCU firmware were chosen to satisfy system requirements in the implementation described in the following sections.

3.2.1 Analog Circuits

The analog signal chain shown in Figure 3-5 consists of three amplifier stages connected in series. The first differentially records the input signal between the working and reference electrodes (WE and RE respectively), the second subtracts the hardware artifact template, and the third amplifies the signal for final processing by the software module.

The first stage is implemented using an Instrumentation Amplifier (INA111, Texas Instruments, TX, U.S.), which exhibits low noise, high precision subtraction, and insignificant input bias current. The minimal input bias current assures no disturbance to electrode-tissue interface at RE and WE electrodes. The amplifier gain is set to one, as amplification takes place only after artifact reduction is complete.

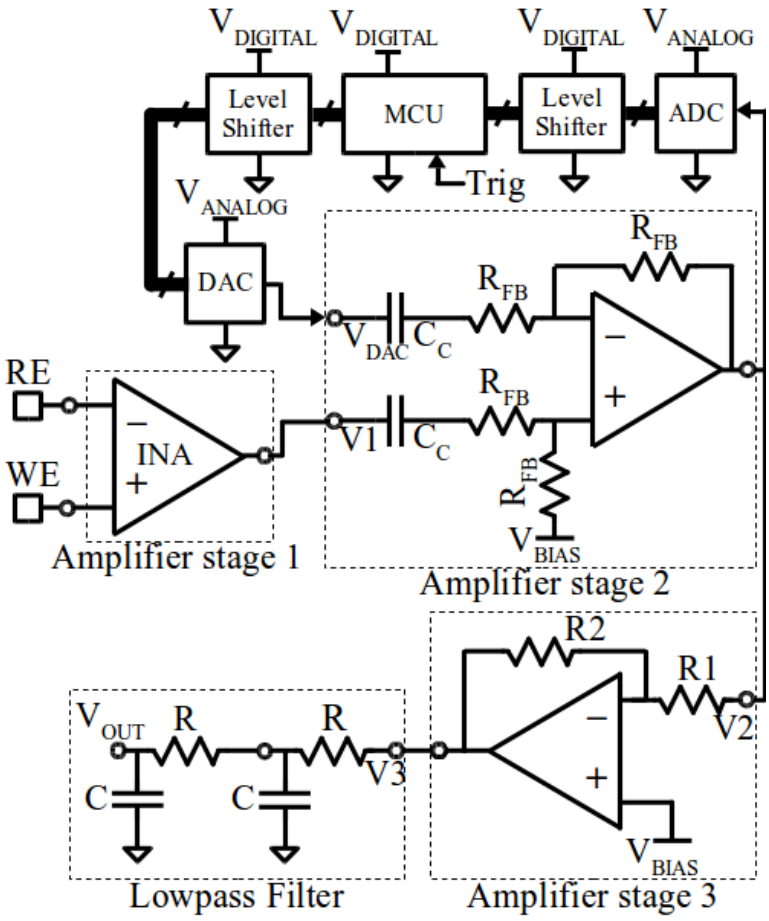

Figure 3-5. Schematic of implementation of the hardware module for stimulation artifact cancellation.

The second amplifier stage employs a capacitive input and resistive feedback and performs artifact subtraction at unity gain. Amplifier feedback is carefully designed to remain stable during fast edges and large-signal variations in common-mode and differential-mode signal components during template subtraction. Coupling capacitors C_{cpl} and feedback resistors R_{fb} are chosen to

ensure the required low frequency cut-off point, noise level, and sufficient phase margin. The low frequency cut-off is set to comply with system specifications using the relationship $fc_{low}=1/(2\pi R_{fb}C_{cpl})$. Thermal noise generated by R_{fb} appears in the signal frequency band and is considered in the design trade-off. The DAC signal is AC-coupled to negative input of the second stage to perform subtraction of the digitized template from the incoming artifact. The DAC is buffered with unity gain to ensure sufficient driving capability. The ADC is connected to the output of the second stage to acquire the hardware artifact template and update it until it converges with the incoming artifact within 1 LSB of the ADC.

The final output amplifier stage employs a programmable gain amplifier, where the feedback resistor can be programmed based on the need of the neural recording application. The output of this stage is loaded with a second order passive low-pass filter. The final amplifier stage is connected to the DAQ card, which digitizes the signal for the software algorithm.

3.2.2 Data Converters

The DAC outputs the digital template to cancel the incoming input artifact via the second stage Figure 3-5). To effectively filter out the DAC switching noise, the sampling frequency fs must be sufficiently higher than the neural signals recorded. Since the neural signals can contain components up to 10 kHz, fs is set at 100 kHz. A full decade of separation allows the passive filter to attenuate the switching waveforms without distorting the recording. The ADC fs must be the same as that of the DAC.

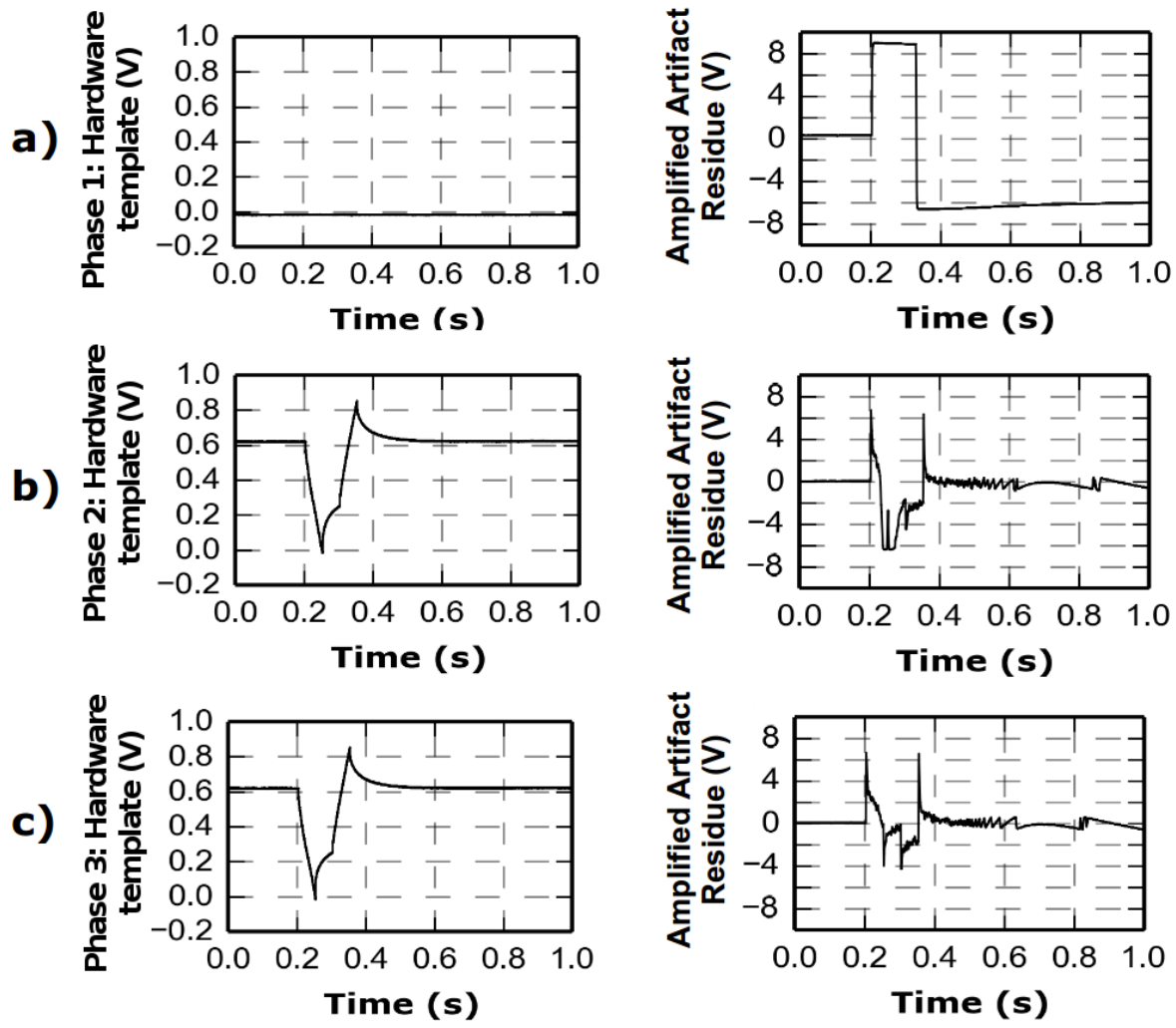

Figure 3-6. Illustration of MCU's operational phases in hardware artifact subtraction.
Left column: artifact template stored in MCU memory. Right column: residual artifact after hardware reduction. (a) Phase 1: output saturates before initial template is acquired. (b) Phase 2: the acquired template is subtracted but leaves areas of saturation in the residual artifact. (c) Phase 3: the updated artifact template is subtracted and results in a smaller artifact residue, displaying no saturation as desired.

The hardware avoids capturing and subtracting the neural signals by choosing the correct ADC and DAC resolution. The resolution is set such that the LSB is larger than the expected neural signal amplitude prior to amplification. At 5 V full scale, 12-bit resolution sets LSB at 1.22 mV, near the maximum of an AP signal, while 10-bit sets LSB at 4.88 mV, near the maximum of an LFP signal. DAC and ADC components are chosen with 12-bit resolution. Adjustment to 10-bit

resolution is performed by discarding the last 2 bits during MCU programming. This flexibility accommodates both neural signal types.

3.2.3 MCU Operations

The MCU performs artifact cancellation in three distinct phases. Each phase is initiated by the stimulator trigger signal, which raises an internal interrupt for every stimulus event. During phase 1, the MCU employs the ADC to digitize and store the output of the raw artifact-contaminated neural signal at the second amplifier output. During phase 2, the MCU outputs the stored template via DAC to subtract the template from the incoming signal. The MCU simultaneously records the resulting residue at second amplifier output. The stored template is iteratively updated during phase 2 by accumulating the residue onto the stored template, which reduces the residue to prevent saturation of the following gain stage (Figure 3-6). The number of required iterations depends on the asymmetry of the differential signal path in second stage (e.g. electrical component mismatch, conductor trace parasitics), but not on characteristics of the incoming signal. It is thus experimentally measured and then pre-programmed at initial testing. During phase 3, the DAC outputs the final converged template to cancel all following artifacts. The output of this phase is the amplified sum of the neural signal and minimized residual artifacts as described in (1). If stimulation protocol is deliberately changed, causing large changes to artifact waveform, the MCU is then reset back to phase 1 to recalibrate to the new artifact. Lastly, an experiment protocol with multiple stimulation patterns can be accommodated by recording and pushing the corresponding templates into MCU memory stack at initial test and sequencing them by an external control pin as needed during the experiment.

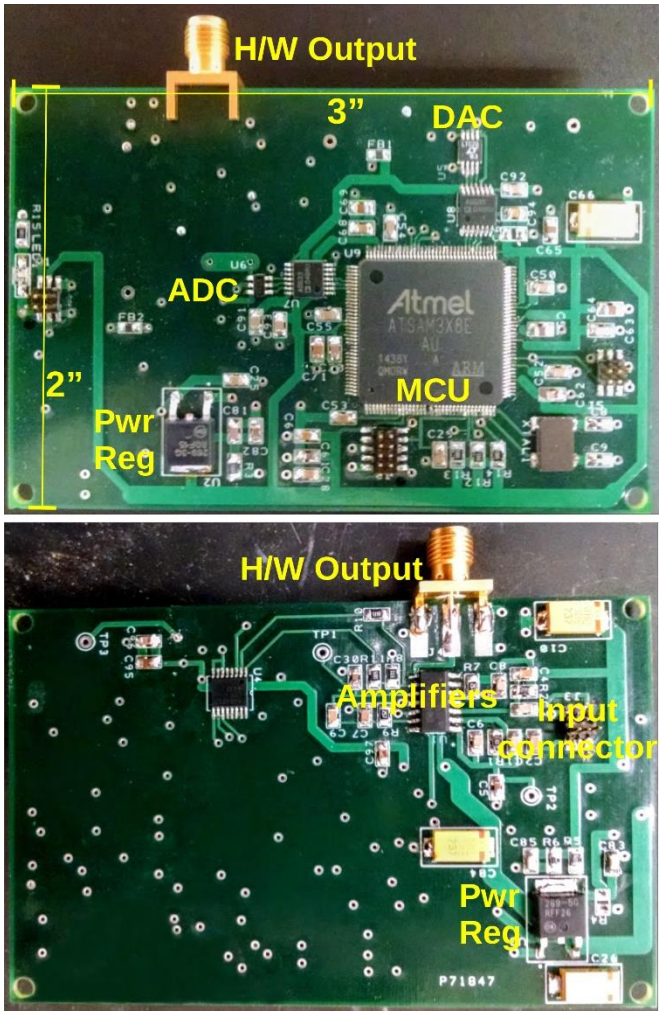

Figure 3-7. HW-M is implemented on a printed circuit board.
The board contains the signal chain based on amplifiers, ADC, DAC and MCU, and the supporting components. The board is implemented with one recording channel only, to validate the methodology and design for same-electrode stimulation and recording.

3.2.4 Hardware Module Printed Circuit Board

The HW-M is implemented on a printed circuit board (PCB) to validate the artifact cancellation methodology and the selected design topologies (Figure 3-7). The validation is specifically focused on testing the performance of the system in the same-electrode stimulation and recording configuration. The PCB is designed with 4 layers. Two outer layers contain traces which conduct the system’s analog and digital signals, respectively. The two inner layers are

designed as parallel planes connected to digital ground and analog ground, respectively. This allows the digital and analog currents to circulate between their respective traces and ground plane, which significantly reduces digital noise from coupling to the analog signals.

3.3 Software Module Implementation

Prior to software signal processing, the DAQ card NI 6259 M Series, (National Instruments, Austin, TX, U.S.) digitizes the hardware device output. The device output, along with the trigger signals indicating the start of each stimulus, are simultaneously read via the DAQ card into the GUI software. The software performs signal processing online and displays results live. The algorithm and GUI are implemented in Python (Python Software Foundation, https://www.python.org/).

The core of the software design is the template averaging algorithm that aligns the trigger signal with the hardware device output and extracts segments of stimulation artifact, each containing a residual artifact $\Delta a(i)$ and an underlying neural activity segment $s(i)$ (3). As mentioned in Section 3.1.1, the neural response, which occurs any time after the stimulation that caused it, is not included in $s(i)$ and thus passes unaltered to the output. The $s(i)$ instead contains an incidental neural signal that spans the artifact, is uncorrelated to stimulation and thus varies from instance to instance. The algorithm preserves the consistent Δai and suppresses the varying $s(i)$ by averaging the last k instances. The number k is chosen to reduce the averaged $s(i)$ component to a size below the system's noise requirement (Section 3.1.2), which is 0.1 of the amplitude of the original neural signal.

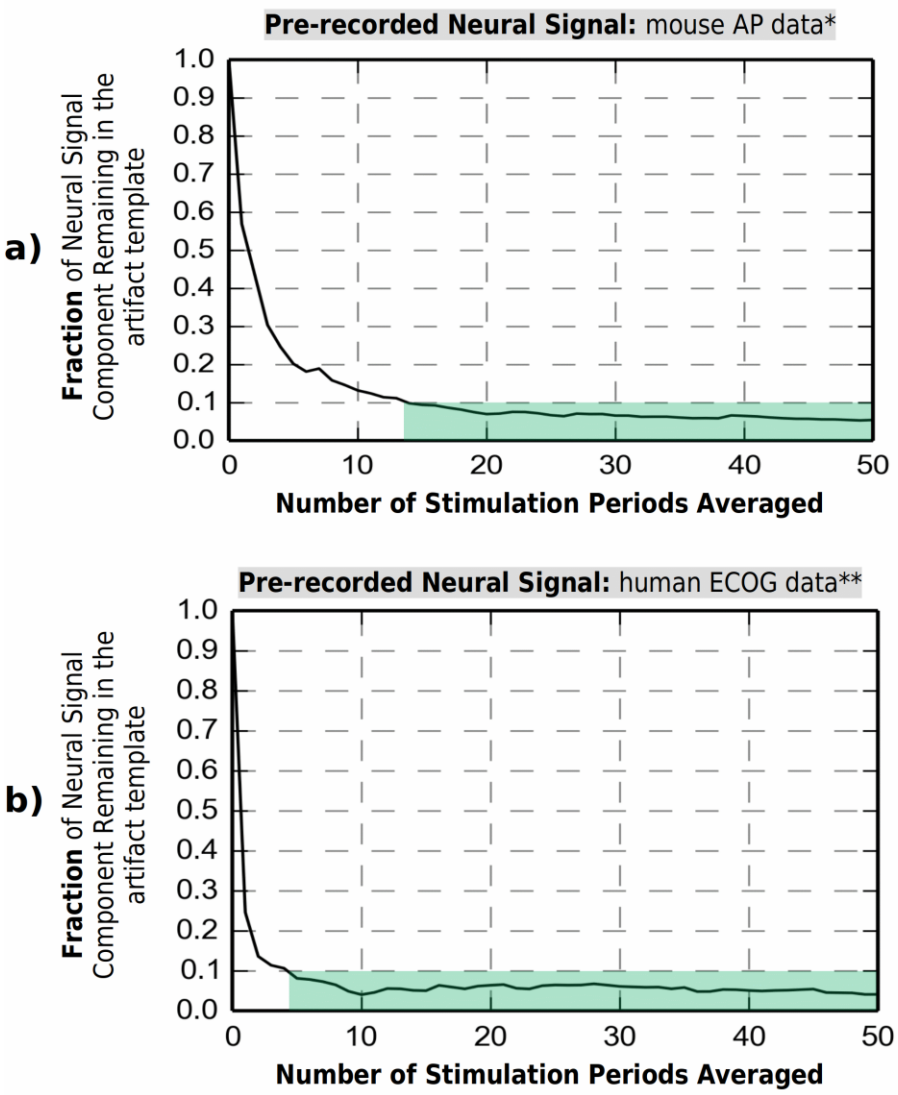

Figure 3-8. Trade-off between number of stimulation periods averaged and fraction of neural signal component remaining in the generated artifact template.
The trade-off is analyzed for: (a) Mouse AP data*, (b) Human ECOG data**. Are where the remaining signal component fraction is below 0.1 is highlighted in green.

Two pre-recorded neural signals (AP and LFP) are analyzed in Figure 3-8 to determine the optimal k. The plots show the trade-off between k and the fraction of the neural signal remaining in the generated template. k = 20 meets the requirement with a safe margin in both cases. In a case with a different signal type, this number can also be set experimentally during initial recording to reduce the artifact residue by a template generated with sufficient averaging. The averaged artifact

template is then subtracted from each individual residual artifact at the hardware device output, and the final result is displayed to the user. The running-average live algorithm dynamically adapts to any changes in the artifact waveform caused by chemical drift at the electrode-tissue interface. These drifts are small, don't pose risk of saturation and don't affect the hardware module operation.

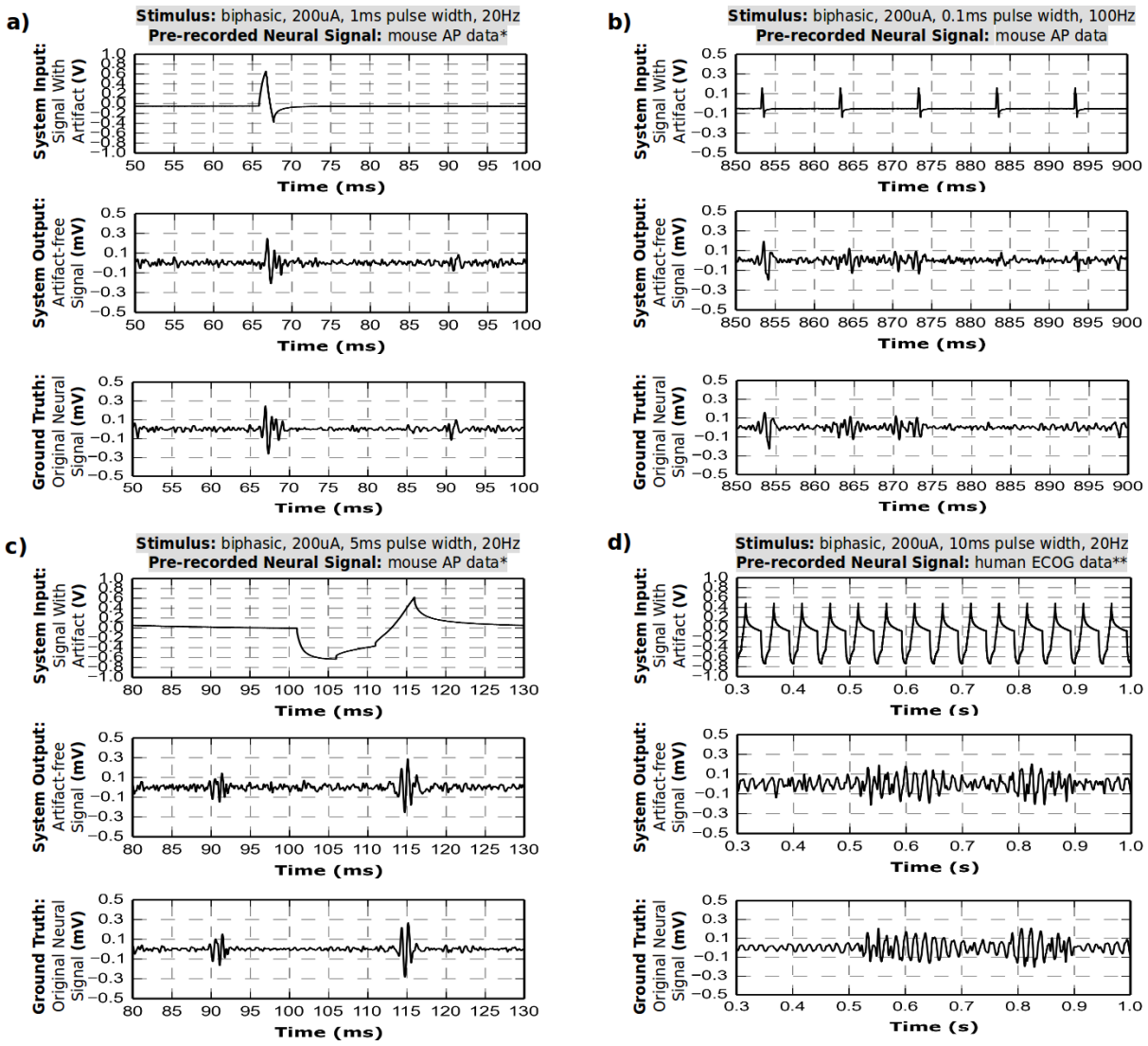

Figure 3-9. The system is tested in-vitro in a saline solution with the same-electrode stimulation and recording setup.

The electrode impedance is ~5 kΩ at 1 kHz. Four different stimulation protocols are used, while a pre-recorded neural signal is injected into the saline. For each case, the system input contains a neural signal and a stimulation artifact. The artifact is canceled with hardware and software real-time processing and the neural signal is recovered. The recovered signal closely resembles the ground truth. ∗(a)–(c) uses Mouse Action Potentials pre-recorded from hippocampus [28]. * *(d) uses human ECoG data containing fast-gamma waves. Data is provided to us courtesy of Dr. Yue-Loong Hsin, Biomedical Electronics Translation Research Center at the National Chiao Tung University, Taiwan.

3.4 In-Vitro Experimental Results

3.4.1 In-Vitro Test Setup

The prototype device is initially tested in-vitro with stainless steel wire electrodes (AS632, Cooner Wire, U.S.) immersed in saline (0.90% NaCl). The electrode impedance is measured to be ~5 kΩ at 1 kHz. The setup is configured for same-electrode stimulation and recording, as in Figure 3-1. The working electrode is connected to both the current stimulator developed in our prior work [55] and the positive input of the recording device. The reference electrode connects to the negative terminal of the recording device. The ground electrode is connected to the ground terminal of the device and the stimulator. An additional wire electrode injects pre-recorded neural signals into the saline.

3.4.2 In-Vitro Test Results

The versatility and capability of the prototype device is demonstrated in four distinct test cases, with different test conditions, as labeled in Figure 3-9. In each test, the working electrode directly records the artifact from the stimulator, while simultaneously picking up the injected pre-recorded neural signal from saline. The neural signal overlaps in time domain with stimulation artifact. The artifact is suppressed in real-time to prevent saturation and the fully recovered neural signal is captured for visual analysis in Figure 3-9 (a)-(d). The system input plot shows the pre-recorded neural signal with the superimposed artifact; the artifact is much larger than the neural signal and thus dominates the waveform. The system output plot displays the recovered neural signal after full hardware and software artifact cancellation, normalized by the gain. The ground truth plot shows the original signal injected into saline.

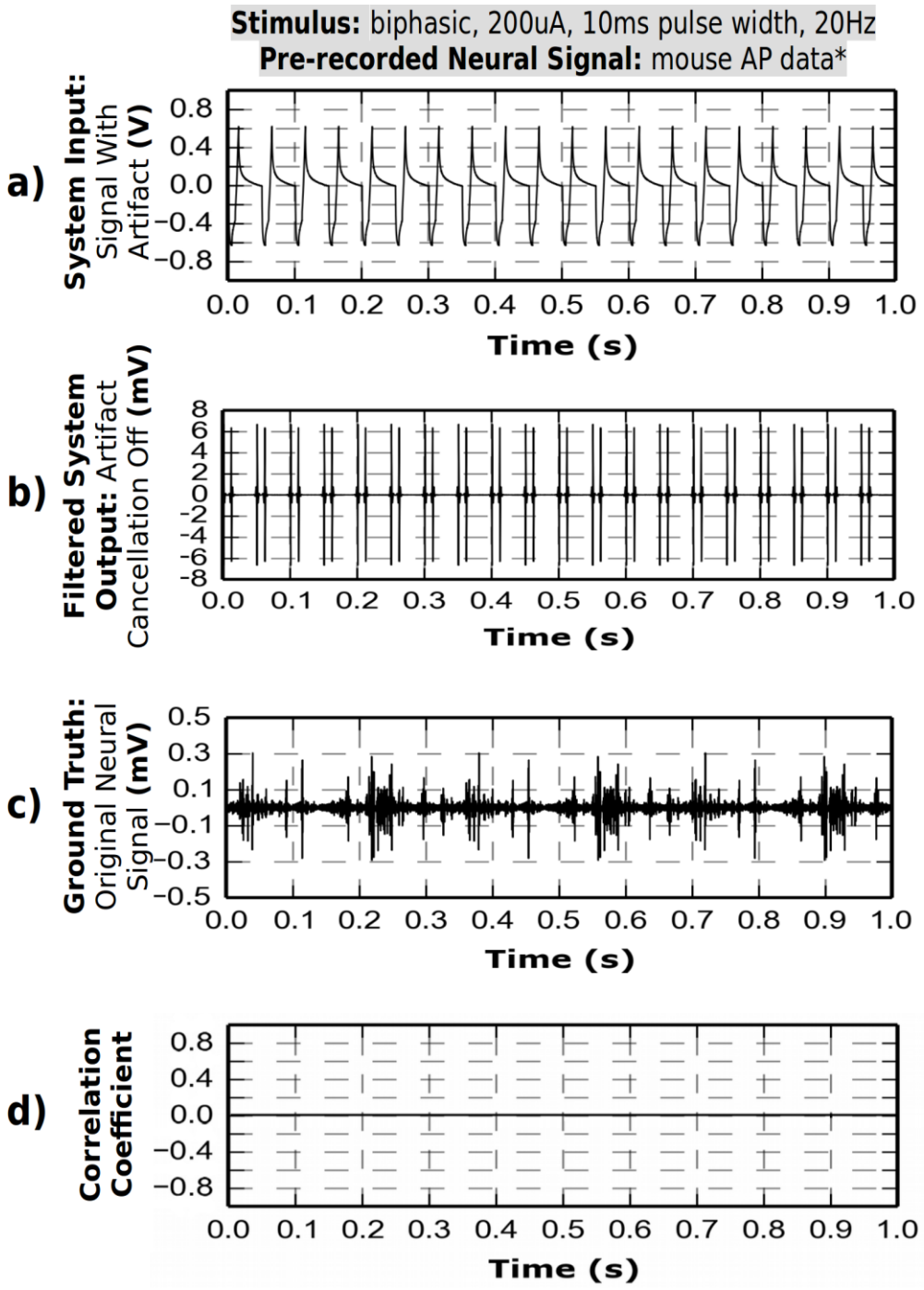

Figure 3-10. Artifact cancellation feature is disabled, and simple frequency filtering is applied to amplifier‘s output by the software.
Amplifier is saturated and incurs complete signal loss. Pearson correlation coefficients between output signal and the ground truth are zero, confirming that output waveforms do not contain any valid neural signals. (a) System Input: Signal with artifact (V). (b) Filtered System Output: Artifact Cancelation off (mV). (c) Ground Truth: Original neural signal (mV). (d) Correlation coefficient.

Each of the test cases demonstrate full signal recovery throughout the entire length of the stimulation artifact. In test (c), the neural spike of interest underlies the anodic phase of the artifact. In the other three cases, the neural spikes (or fast gamma waves) span the full length of the artifact(s). The neural signal is recovered in all four cases. An added noise is observed in the recovered signals and shows no dependency on stimulation conditions. Test (d) shows the most pronounced distortion of recovered neural signals. The fast gamma signal is distorted due to residual artifact by less than 100 μV relative to ground truth, which translates to a reduction of the raw 1.2 V artifact by more than 100 dB (20 dB scale). Test data is further analyzed in time and frequency domains in the Section 3.4.3.

3.4.3 Signal Correlation

The Pearson correlation coefficient between the recovered neural signal and the ground truth is displayed before and after artifact cancellation is applied in Figure 3-10 and

Figure 3-11, respectively. As discussed earlier, when artifact cancellation is not performed, the amplifier saturates at the hardware module and cannot record the signal of interest. Figure 3-10 (a) shows the device input (sum of stimulation artifacts and a pre-recorded neural signal) to the system with artifact cancellation turned off. Figure 3-10 (b) shows the resulting system output. The output signal is filtered with a 350-5000 Hz band-pass filter by the software in an attempt to recover the neural signal APs. The neural signal ground truth is shown in Figure 3-10 (c). Figure 3-10 (d) shows zero correlation between filtered system output and the ground truth, which confirms signal loss due to amplifier saturation. In contrast, saturation is avoided when artifact cancellation is enabled (

Figure 3-11) and signal is successfully recovered with an average Pearson correlation coefficient of 0.83. The non-ideal recovery is attributed to signal distortion by the system noise.

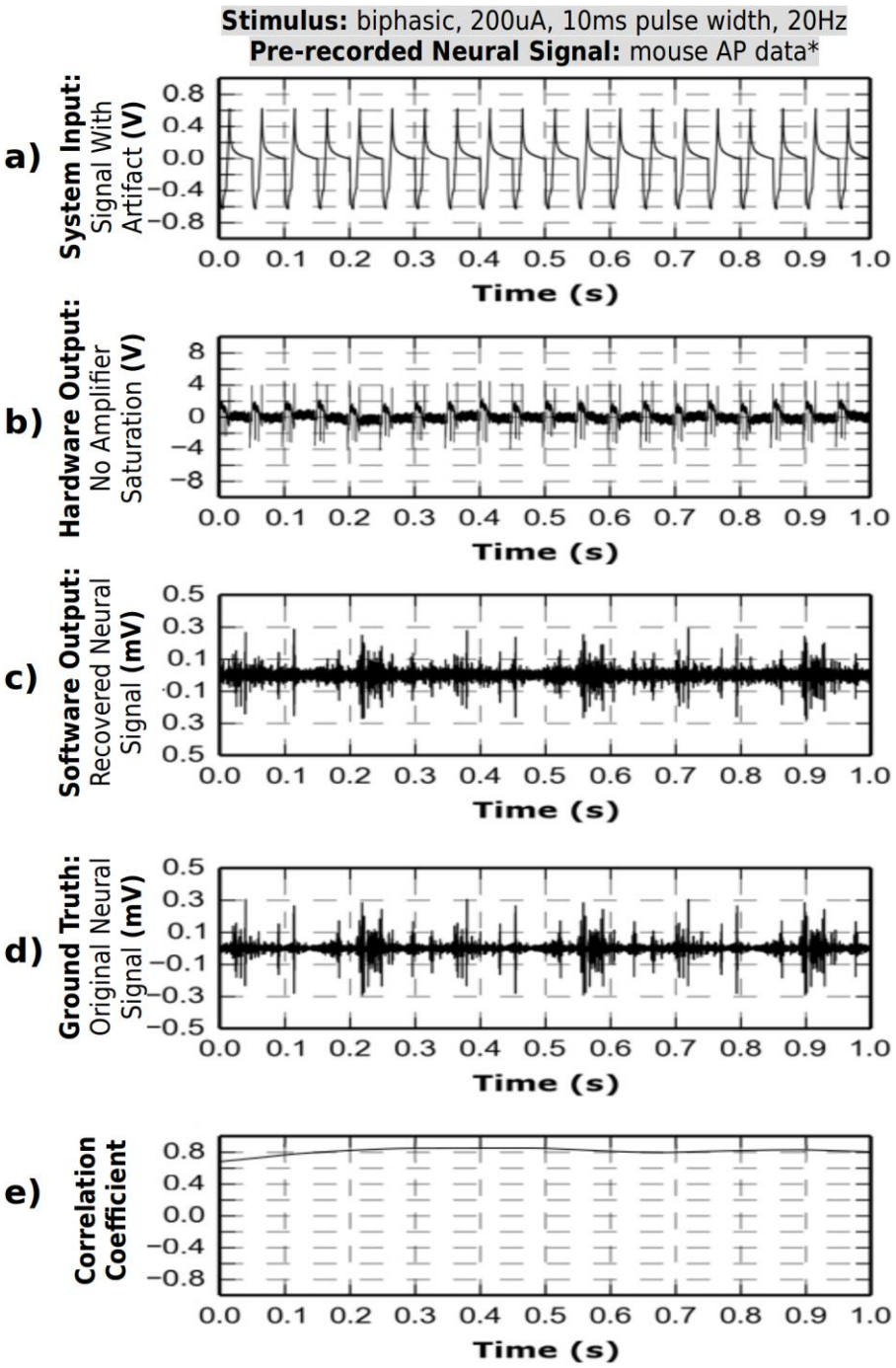

Figure 3-11. Artifact cancellation by hardware device prevents any amplifier saturation.
The hardware output contains the neural signal component, which is recovered via software algorithm. Pearson correlation coefficients between output signal and the ground truth is of ~0.8, which demonstrates that the recovered neural signal contains valid data. (a) System Input: Signal with artifact (V). (b) Hardware Signal: Artifact reduced to prevent saturation (mV). (c) Software output: Recovered neural signal (mV). (d) Ground Truth: Original neural signal (mV). (e) Correlation coefficient.

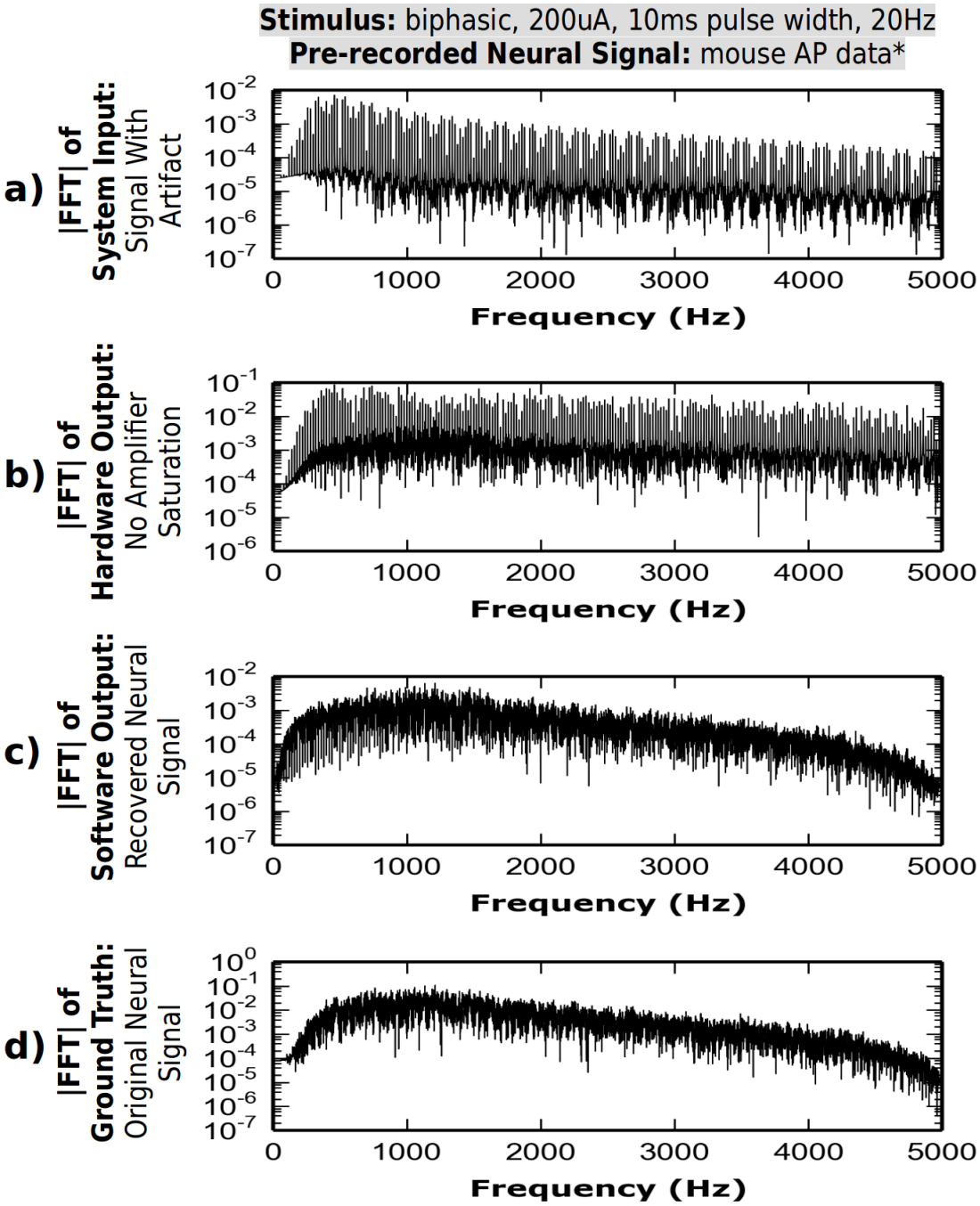

Figure 3-12. Frequency spectrum of system input signal contains artifact harmonics.
The harmonics are minimized and amplified at hardware output. Software algorithm removes the residual artifact producing output with spectrum similar to that of the ground truth. (a) |FFT| of system input: Signal with artifact. (b) |FFT| of hardware output: No amplifier saturation. (c) |FFT| of software output: Recovered neural signal. (d) |FFT| of ground truth: Original neural signal.

Frequency Spectrum Analysis

Figure 3-12 shows the Fourier transform plots of the signals at various stages of the artifact cancellation system. Since the stimulus artifact waveform is periodic and has high edge rates, it has a frequency content similar to that of a square wave. This content is a set of large periodic harmonics throughout the full spectrum of hardware module input (a) and output (b). In contrast, plot (c) illustrates the recovery of the neural signal free of such artifact harmonics. In addition, the similarity between the Fourier transform of the recovered signal (c) and the ground truth (d), indicates that the neural signal is preserved with minimal distortion, as previously seen in the time domain.

In addition, the system was tested in-vitro with a 2 V stimulation artifact at 20 Hz injected at the input without any neural signal, and the output spectrum was used to calculate the effective system noise post-cancellation (Figure 3-13 (a)-(c)). The integrated noise was calculated to be 9.7 µVrms and 9.4 µVrms for 1 Hz-10 kHz band and 300 Hz-10 kHz band, respectively. Furthermore, a 100 µV sine wave was injected with and without 20Hz stimulation to measure system's signal distortion (Figure 3-13 (d), (e)). The chain of amplifiers in the system exhibits THD of 0.88% for 100 µV sine wave input. It produces distortion spurs at -111dBV, which is 31dB below the -80dBV sine wave tone after artifact cancellation. The distortion spurs are spaced 20Hz apart from the fundamental tone and occur due to mixing between the repeating artifact and the injected sine wave.

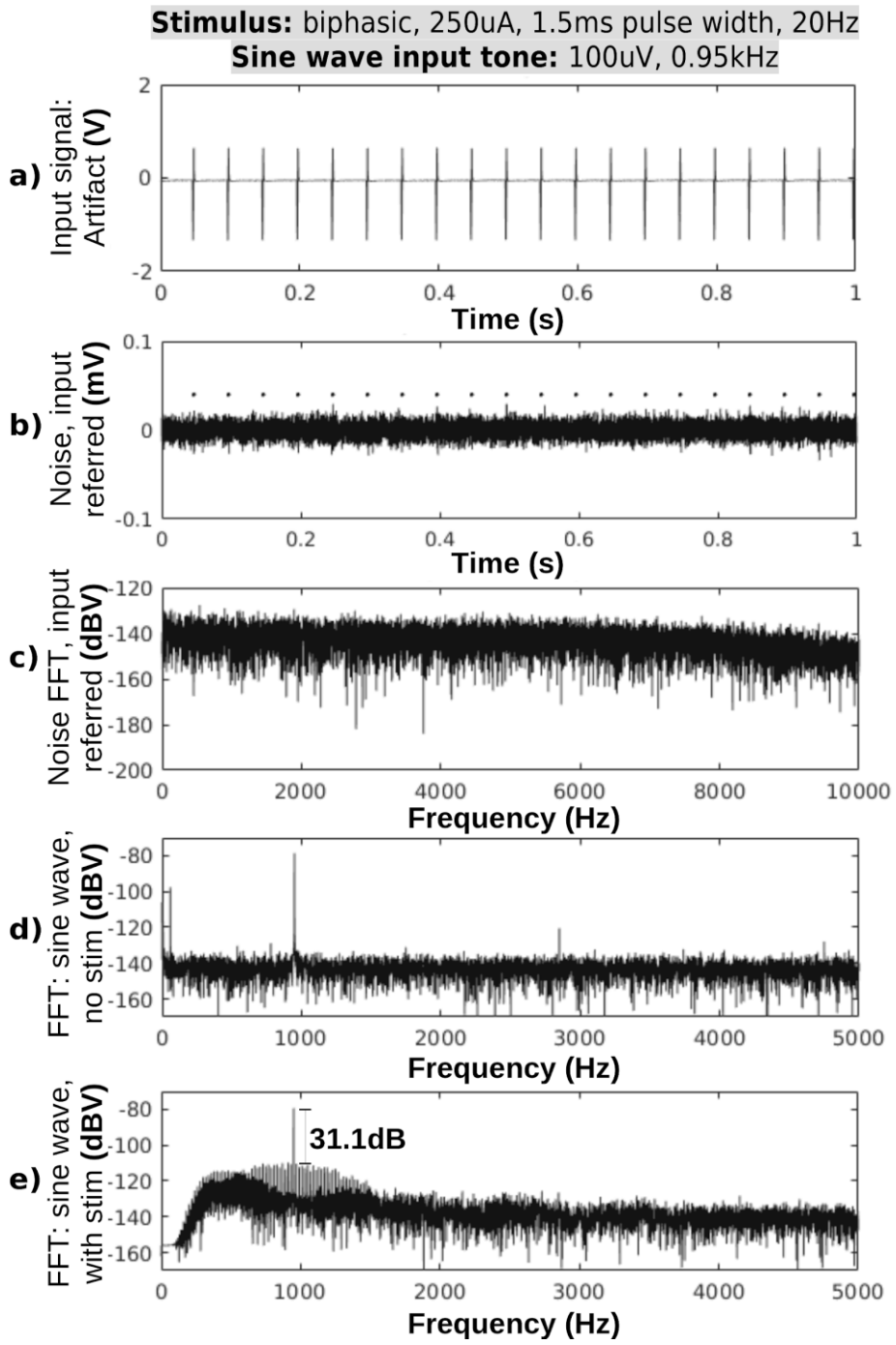

Figure 3-13. The prototype system is tested in-vitro for noise and distortion.
(a)–(c) A 2V stimulation artifact is cancelled by the system. Output noise includes residual artifacts and integrates to 9.7 μVrms in 1 Hz–10 kHz band. (d) The system exhibits THD = 0.88% for a 100 μV sine wave without stimulation. (e) When 2 V stimulation artifact is applied and cancelled, the system incurs distortion 31.1 dB below the 100 μV sine wave tone. The distortion spurs are spaced 20 Hz apart and are the products of mixing between the large artifact and the small sine wave signals in the amplifier chain.

3.5 In-Vivo Experimental Results

3.5.1 Animal Preparation and Electrode Implantation

The prototype device is further tested in a male Sprague Dawley rat (255 grams) in-vivo. The animal was anesthetized with isoflurane (2%) to a depth of anesthesia that does not elicit a response to foot pinch or reflexive paw response to ear bars. A midline scalp incision was made to expose the midsagittal suture from bregma to lambda, the skin retracted and galea was cleaned from the skull to allow dental acrylic to adhere at the end of the procedure. Using a variable-speed Dremel drill with sterilized jewelers screw-sized bit, very small holes were drilled bilaterally to allow the passage of recording microwires to underlying cortical and subcortical tissue. A pair of tungsten microwires (50 μm OD) with 1.0mm distance between the tips was implanted bilaterally into the left (LSu) and right (RSu) hippocampal subiculum area (coordinates: AP=-6.7; ML=4.6; DV=4.0) based on [56]. The impedance of the microwire electrodes was measured to be ~100 kΩ at 1kHz. Only one electrode was simultaneously stimulated and recorded at a time for in-vivo testing of the device prototype. The reference and ground screw electrodes were placed in the cerebellum near the midline at a distance 1mm from each other. Surgery and all experimental procedures were approved by the Chancellor's Animal Research Committee of David Geffen School of Medicine at UCLA. Experiments were carried out under freely moving conditions to record brain activity for verification of successful electrode implantation.

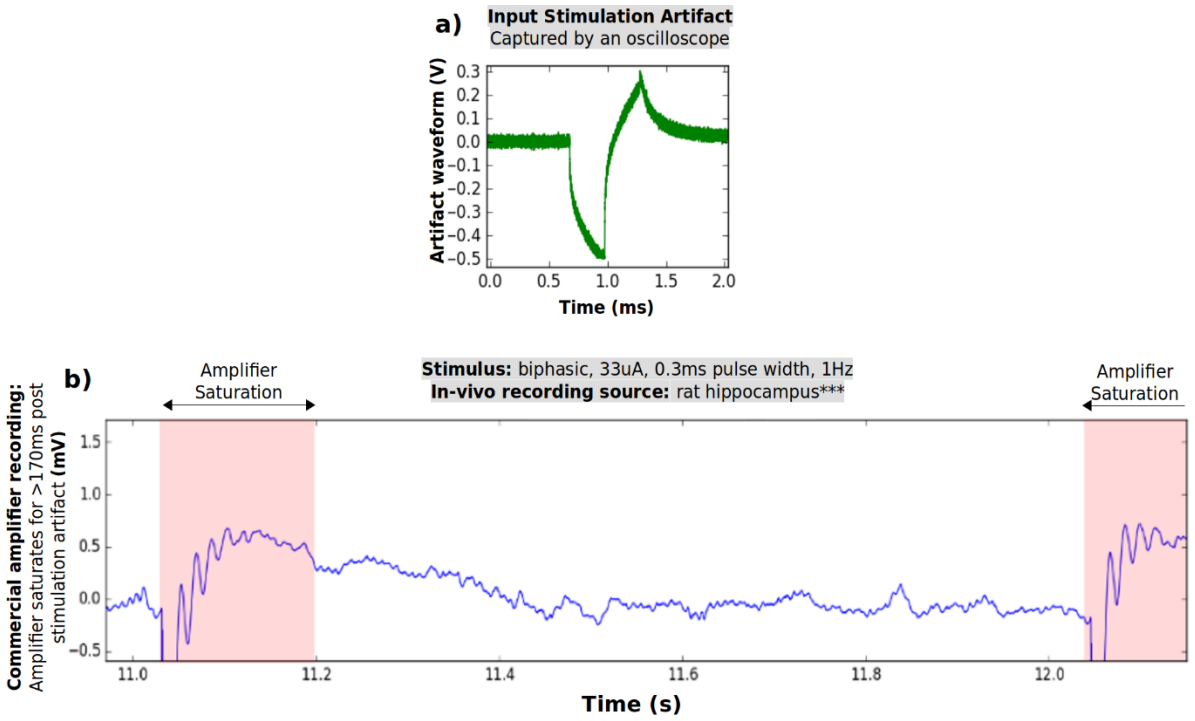

Figure 3-14. In-vivo same-electrode stimulation and recording test is made using commercial neural amplifier (RHD 2132, Intan Technologies, CA, U.S.).
(a) Stimulation artifact presented at the input of the amplifier has an amplitude of ~0.8 V. (b) Commercial amplifier saturates at each stimulation event due to a large artifact and its output shows ~180 s of milliseconds of saturation recovery, incurring complete signal loss before returning to normal recording. ***Animal recording was made available to us courtesy of Dr. Anatol Bragin, Department of Neurology at the University of California, Los Angeles, CA, U.S.

3.5.2 In-vivo Test Setup

Stimulator and artifact cancellation system prototype share the same working electrode and are connected similarly to the in vitro setup. A commercial neural recording amplifier (RHD 2132, Intan Technologies, CA, U.S.) is connected in parallel with the prototype for a side-by-side comparison of the recordings during stimulation onset. An electrode in the hippocampus area is chosen for stimulation and recording due to relatively high excitability and expected abundance of neural responses. Similar set-up for the in vitro experiment is reused here. Stimulation parameter limits are chosen experimentally to avoid disturbance to the animal. The pulse amplitude and duration parameters are swept at stimulation frequency of 1 Hz, while monitoring the recorded

output. The selected frequency avoids neuron fatigue, while the selected amplitude of 33 µA and the duration of 0.3 ms generate adequate neural responses, without altering the animal's behavior. When this stimulus current is injected into the impedance of the implanted electrode, it generates an artifact with and amplitude of ~0.8 V. (Figure 3-14 (a)).

3.5.3 In-vivo Test Results

The recording output from the commercial amplifier by Intan Technologies is displayed in Figure 3-14 (b). The amplifier saturates, as the amplitude of the stimulation artifact exceeds amplifier's input range (-4 mV to +4 mV) at a gain of 1000 V/V by two orders of magnitude. The saturation and recovery periods last hundreds of milliseconds until the system's amplifier settles back to normal operation. During this period the neural responses are lost without any possibility of recovery by post processing. Figure 3-15 (a) shows extracted consecutive segments of the recorded data in response to ten consecutive stimulation events. The segments are overlaid as a family of curves, and the stimulation event for each occurs at zero seconds. Each individual curve displays consistent saturation behavior bearing no information of neural signals present during this time period.

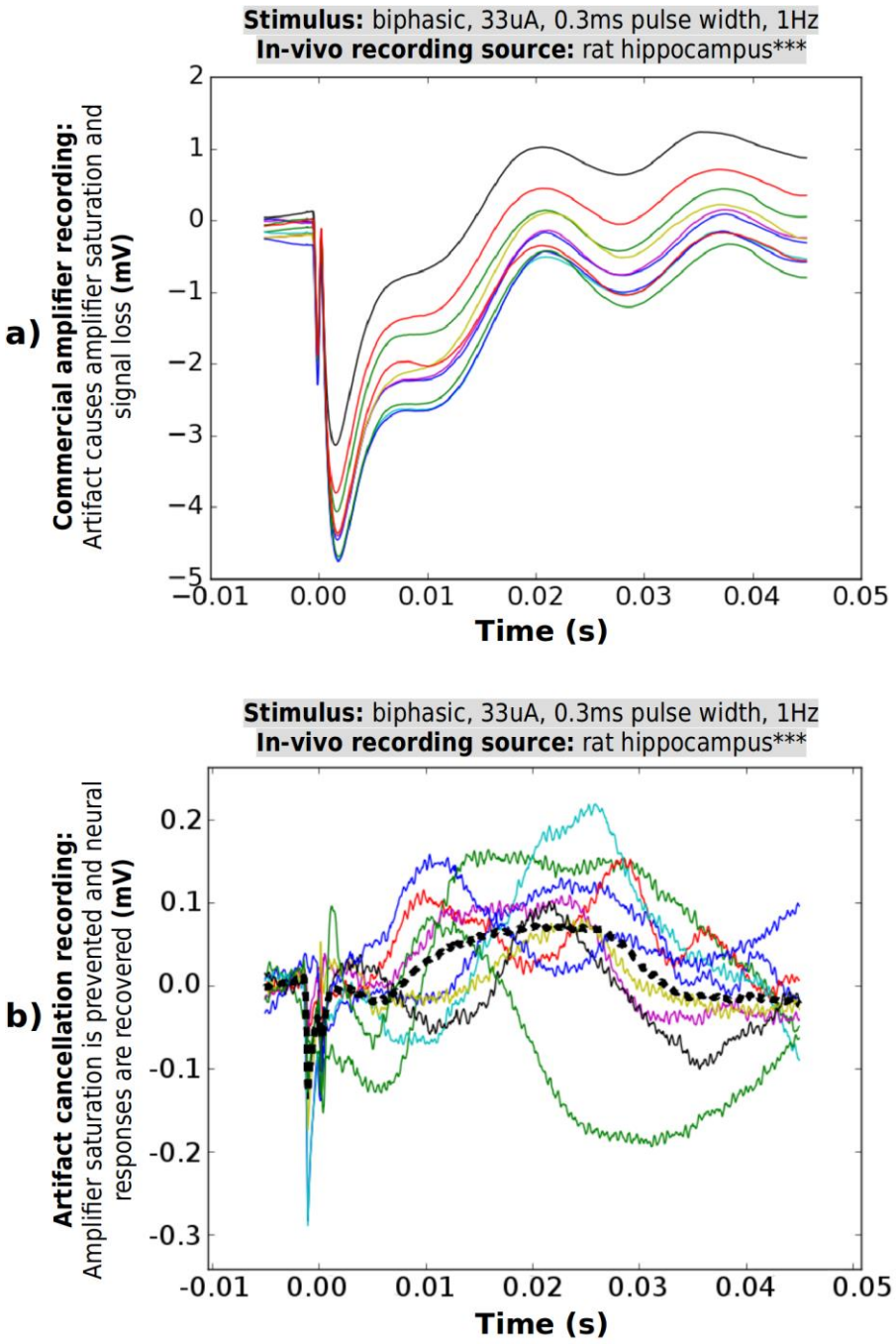

Figure 3-15. In-vivo same-electrode simultaneous stimulation and recording using our design. 10 consecutive segments triggered by the stimulation event are extracted from the recording and overlapped. (a) Commercial neural amplifier recording shows amplifier's saturation and slow recovery, which completely conceals neural responses. (b) Proposed design suppresses a large artifact, prevents saturation and recovers neural responses. 10 responses are overlaid, and the average is plotted with dashed line. The output waveform contains a remaining fraction of the artifact waveform, which is discussed in Section 3.5.3.

The designed prototype connects in parallel to the same electrodes, cancels the artifact and avoids the unrecoverable signal loss. The resulting recording was dissected into stimulation-triggered segments. Figure 3-15 (b) shows 10 consecutive segments extracted from a single recording instance and overlaid as a family of curves. The average of 10 curves is plotted with a dashed line. The curves display the neural responses to each stimulation instance. In contrast to commercial amplifier data in (a), this device avoids saturation and preserves the neural response waveforms. Response magnitudes range 100-200 μV, with pulse durations 10-20 ms. The characteristics of the recorded neural responses match previously reported studies of local neural network responses to stimulation (e.g. [57]).

The waveforms recorded in-vivo still contain a residual fraction of the stimulation artifact. This residual component, not cancelled by the template subtraction algorithms, is a result of the stimulator's random output noise. The noise is much more pronounced in the in-vivo recordings compared to in-vitro due to scarring formed around the in-vivo electrodes. The electrodes used for recording were implanted in this animal for several months, incurring inflammation and scarring [58]. The scar tissue formed around the electrode prevented neuron AP recording (larger group responses were captured instead) and increased the electrode impedance from baseline 100 kΩ to an impedance several times higher. The higher impedance results in higher voltage noise for a given stimulator current noise. Notably, the system still achieves artifact suppression from ~0.8 V amplitude to a noisy residue less than ~300 μV (more than three orders of magnitude reduction) and recovers the neural signals in-vivo in same-electrode stimulation and recording. In a case with an electrode specifically designed for long-term recording, the scarring and thus impedance are expected to be better controlled, allowing better artifact cancellation.

In comparison to the amplifier blanking approach, which avoids recording during stimulation, this design prevents saturation of the amplifier and allows uninterrupted recording. In cases with better controlled stimulator noise and/or electrode impedance (as with in-vitro results), a full artifact removal can be achieved. Whereas the blanking approach makes it impossible regardless of the stimulator and electrode characteristics.

Generally, the issue of stimulator noise is not considered in previously published artifact-cancellation works that record at a distance from the stimulation site, where artifact effects are greatly attenuated. Relatively, the challenging same-electrode setup will confront a much larger artifact and consequently a larger stimulator noise. This noise will be higher in current-mode stimulation with high-impedance electrodes (e.g. penetrating Multi-Electrode Arrays) or with noisy voltage-mode stimulators. Both scenarios motivate the designs of custom low-noise stimulators to achieve better cancellation.

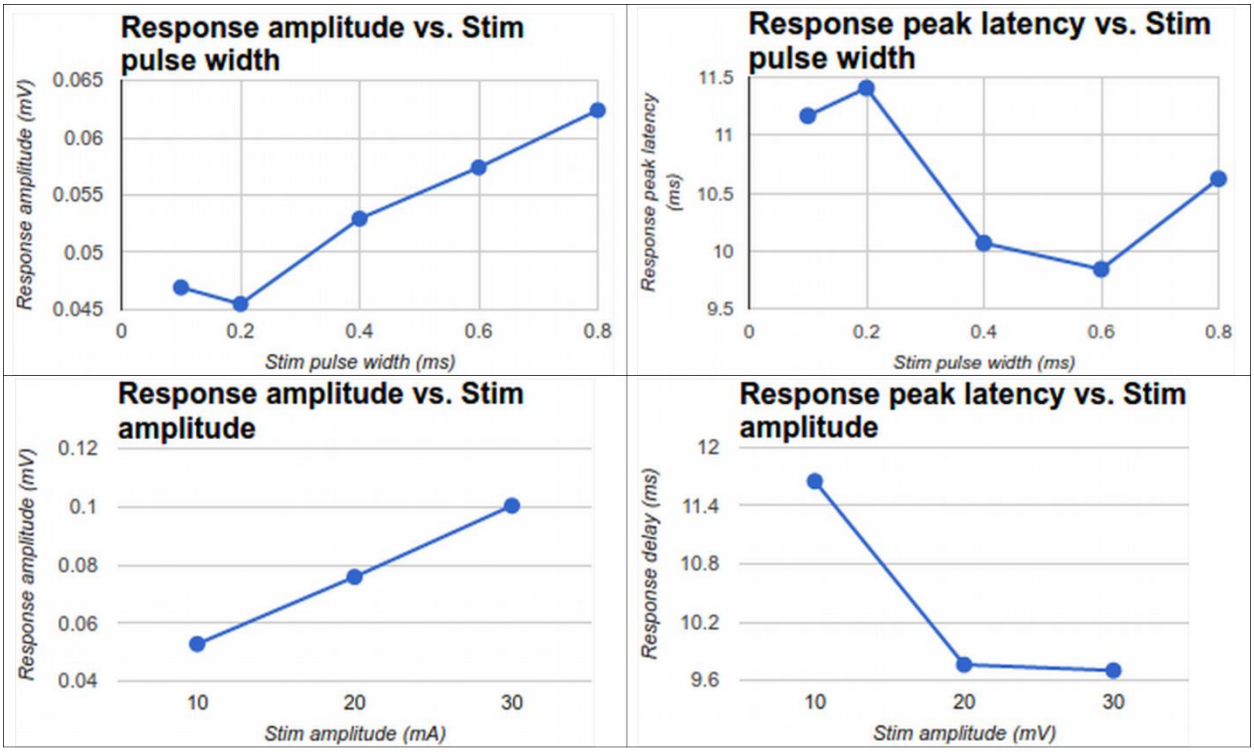

Figure 3-16. Stimulation parameter sweep generates neural responses with corresponding characteristics.
The amplitude of neural responses increases linearly with both, increasing stimulation amplitude and pulse width. The latency of neural responses instead tends to decrease with increase in stimulation amplitude and pulse width. This follows the intuition.

To further confirm the validity of the in-vivo recording results, we have collected a set of neural responses to stimulation protocol with various parameters (Figure 3-16). The same-electrode stimulation and recording setup is preserved, and each response data point on the graphs represents an average of 10 responses with the same stimulus parameters. The neural response amplitude tends to increase with increasing stimulation pulsed width and stimulation amplitude. This is expected, as the increase in each of these stimulation parameters increases the amount of charge injected into the electrode interface. Increased stimulation charge recruits more neurons around the stimulating electrode, thus increasing the amplitude of the sum of their action potentials. The neural response latency instead decreases with increased current amplitude injected into the electrode interface. This also follows fundamental understanding of relationship between

evoked potentials and stimulus. Higher current initially produces a faster rate of depolarization of the membrane of axons or somas of neurons near locus of stimulation and thus a faster response. The membrane is modelled as a capacitance and thus follows the $\frac{dV}{dt} = \frac{i_{STIM}}{C_{membrane}}$ relationship. Finally, the increase in the stimulation pulse width increases the amount rather than the rate of depolarization of the neuronal membranes. Because our stimulation is at threshold, injecting an increase amount charge by increasing pulse width ensures that the neurons are triggered by this charge, reducing the wait and reliance on background processes to augment the stimulation protocol, thus reducing the latency of neural responses. Though the trend in the plot has an infliction as further increase in charge is not necessary for triggering action potentials.

The plots collected in Figure 3-16 help confirm that the signals represent valid evoked responses, which hold a known relationship to the stimulus, rather than incidental neural activity or a secondary residual stimulation artifact remaining post artifact cancellation.

3.6 Discussion

3.6.1 Use of Adaptive Filters in the Software Module with In-Vivo Data

The real-time software algorithm is designed to use 20 initial artifact samples to compute a usable template waveform and use it to cancel the input signal artifacts (Section 3.3). The approach is suitable for mapping neural networks in-vitro and in-vivo by simultaneous stimulation and recording, and in many closed-loop neural prosthetics which use high frequency trains for neural modulation. The approach may not be desired in some applications, which use low stimulus count for each neural modulation protocol. To reduce the number of initial artifacts needed for creating a template, an adaptive Kalman filter algorithm was tested and compared to the original artifact averaging. The Kalman filter's state estimate is initialized with the first artifact residue,

and the state is updated with observation of each new incoming artifact. Both approaches were applied in post-processing to a raw in-vivo recording taken at the output of the hardware module. Figure 3-17 shows the resulting waveforms for each filter. The Kalman filter requires significantly fewer artifacts to perform effective cancellation, due to its inherently faster convergence.

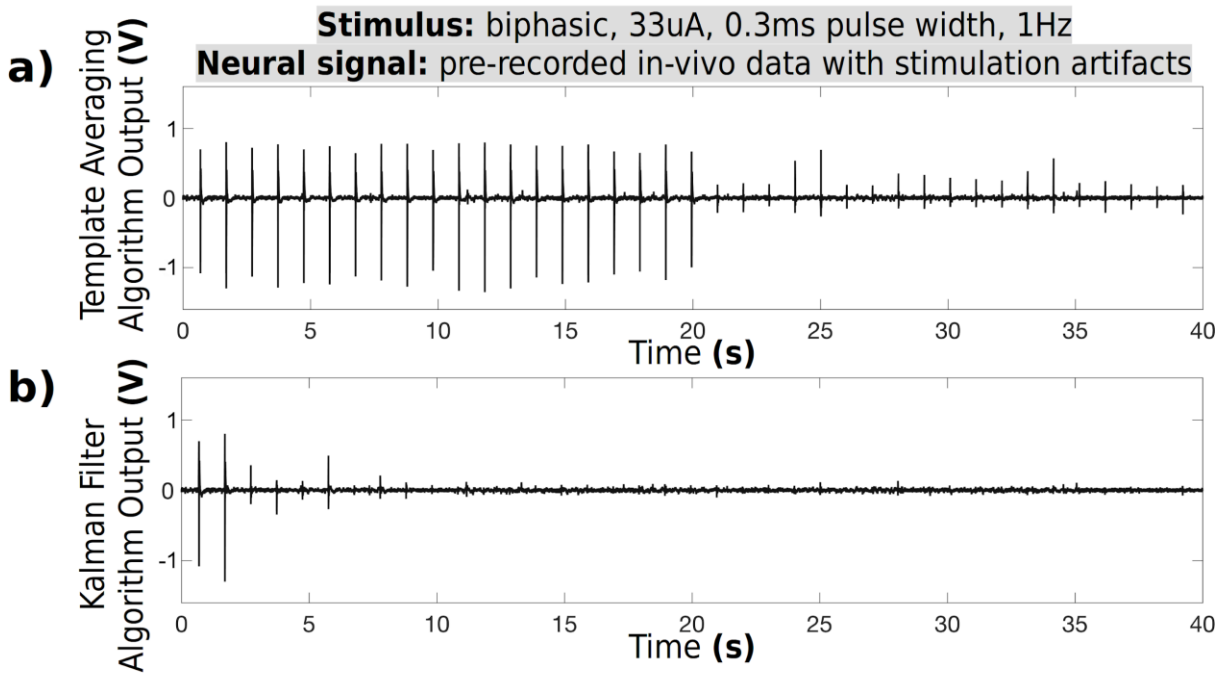

Figure 3-17. Template averaging is compared to Kalman filter approach for software artifact cancellation.
(a) Averaging algorithm used in this design requires 20 initial artifact samples to generate an accurate template. (b) Kalman filter algorithm requires only four initial samples to converge.

3.6.2 Improvement Opportunities in Phase I Design

The approach of Phase I design relies on a key assumption regarding the relationship between stimulation event onset and neural tissue's electrical response. As explained earlier, the response must sufficiently vary in its latency relative to timing to each stimulus, such that the averaging algorithm recovers a template with an intact stimulation artifact residue but a near-zero mean neural response component [19]. The system subtracts the template's contents from the signal to rid the recordings from residual artifacts.

The same is true of the Kalman filter approach discussed above, which updates its state (here - the estimate of the artifact residue) with incoming signal segments. The varying neural signal within the segment can be treated by Kalman filter as noise, whereas the stable artifact residue reaffirms the state estimate, which again helps subtract the remaining artifact within the recordings.

In other applications, such as study of dynamics of neural networks in spinal cord, intact, injured and during post-injury rehabilitation, a standardized protocol generates consistent evoked potentials, which are time-locked to the stimulus [13], thus not satisfying the above assumption. In such cases both the averaging algorithm and Kalman filter would converge to a combination of signal's artifacts and evoked potentials as an output, unable to discriminate between them. Thus, a new algorithm is explored to separate a persistent and time invariant evoked potential superimposed onto the artifact in the recordings. This new approach is introduced into the system architecture in the next phase of the design, which uses additional information to learn the artifact waveform and distinguish it from the underlying neural responses within the signal.

Additionally, the new design iteration expands the hardware module into a multi-channel recording architecture allowing simultaneous cancellation of artifact in stimulation electrode as well as the electrodes in the MEA adjacent and near to the site of stimulation, where the artifact is still large enough to severely saturate the conventional neural recording systems and cause loss of information. This in turn reveals the order in which the neuron bundles generate the responses to stimulation, across the plane of the electrode array. This can, for example, trace the directivity of the local neural network around the site of spinal cord injury and changes to this network during the rehabilitation protocol, as explained in Section 2.4.

Chapter 4

Phase II: Multi-channel Artifact Cancellation Design

4.1 Improvements in System Design

The Phase II iteration improves upon the initial system design and targets the application of studying the neural network dynamics in spinal-cord-injured animal models, as outlined in Section 2.4. While the objective of the design remains the same, additional system requirements drive changes to both Hardware and Software module implementations (Figure 4-1).

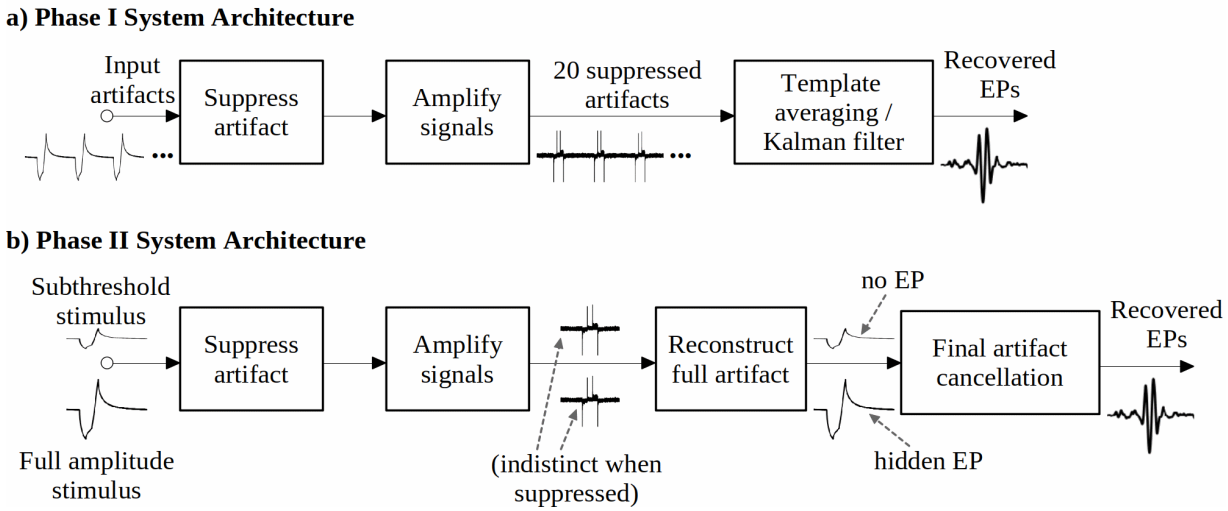

Figure 4-1. Changes to system architecture from a) Phase I design to b) Phase II design. The second design iteration does not require a stimulation pulse train to cancel the artifact. Instead the system reconstructs the full artifact post-suppression and uses a subthreshold artifact waveform scaled up to fit and remove the full artifact waveform.

The evoked potentials in the target application are time-locked to the stimulus events, and, as explained earlier, can't make use of the prior solution which recorded 20 stimulation pulses and subtracted the artifact template generated by averaging. A new algorithm is implemented instead in conjunction with an altered stimulating protocol. A subthreshold stimulation artifact, which contains no evoked potentials, is acquired as described in [18] and used as a template and is scaled up by predetermined factors to match and subtract the full-amplitude stimulus. The full amplitude

stimulus also contains the neural potential which now remains after the subtraction of the scaled subthreshold template. To facilitate the new methodology, the hardware circuit board and signal processing together first suppress the artifact to prevent saturation and signal loss, but now also fully reconstruct the original signal at the output to present the recording signal with full artifact. The fidelity of the reconstructed signal meets the Phase I system-noise requirements. The full reconstructed artifact in the signal is what enables the new artifact removal methodology.

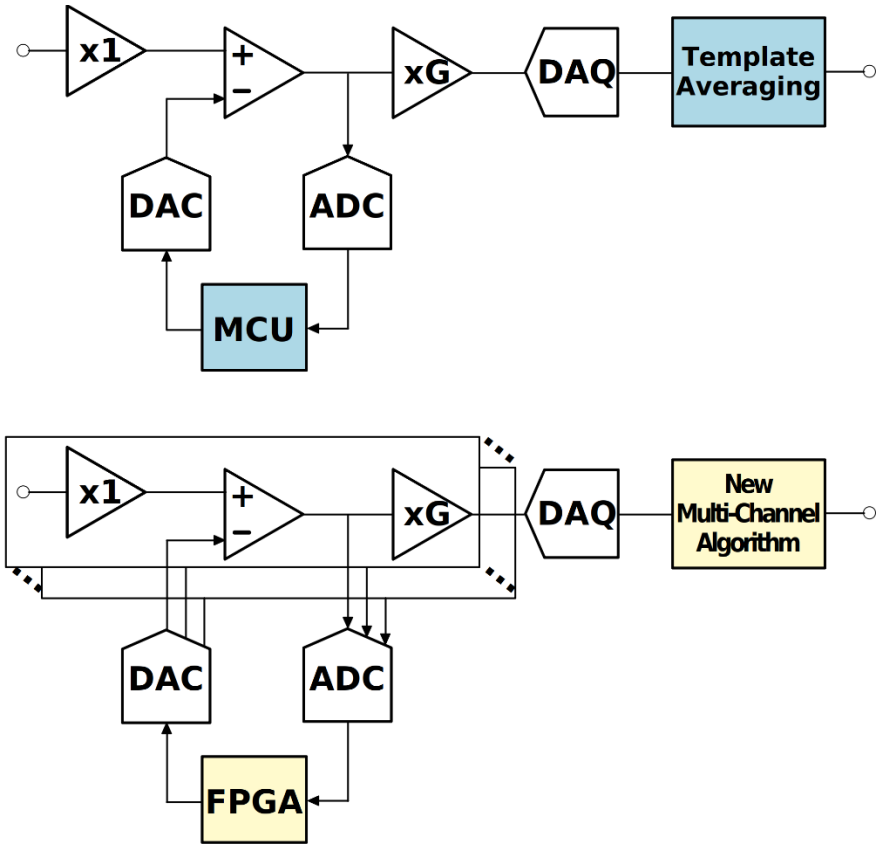

Figure 4-2. Comparison of Phase I to Phase II H/W implementation.
a) Phase I HW module uses an MCU firmware to command one channel artifact suppression. Signal is then routed to the template-averaging algorithm in the backend. b) Phase II HW module uses FPGA firmware to run multi-channel artifact suppression by parallel processing. A digital artifact-suppression data is serially streamed out of FPGA to reconstruct the artifact to its original state. The reconstructed signal with full original artifact is routed to a new, multi-channel artifact-cancellation algorithm.

4.2 Hardware Module Implementation

Following the new system architecture, the Hardware Module in Phase II is redesigned in several aspects, shown in Figure 4-2. The amplifier chain is replicated into eight slices to accommodate eight recording channels. A multi-channel DAC/ADC replaces the previous single-channel equivalent. The Phase I hardware circuits in (a) use an MCU to facilitate the logic for artifact suppression, whereas the Phase II implementation employs an FPGA. The FPGA can run multiple logic slices in parallel to govern the suppression of the artifact in all channels simultaneously. The core logic of new FPGA's firmware remains the same as in Phase I, previously described in Chapter 2, but is now implemented in Verilog code.

The FPGA firmware is additionally designed to output data containing the coarse representation of the suppressed artifacts as a digital bit stream. The bit stream is designed to comply with the Serial Peripheral Interface standard. The data in this format is then collected by the DAQ device along with the analog signals. Both signals are then routed the back-end Software Module which reconstructs the artifacts and thus the full signals back to their original form using the reconstruction algorithm described below in Section 4.3.

Finally, the implemented design of Phase II of HW-M complies to the same performance requirements outlined in Table 3-1, making it compatible with all neural signals and protocols considered in Chapters 1 and 2. The PCB implementation shown in Figure 4-3 follows similar strategy to the one in Phase I. Namely, a four layer board is selected. The two inner layers are mostly used as ground planes to effectively isolate the signals presented in the traces of the outer layers. The board supports simultaneous eight channels of recording. The FPGA on its own daughterboard is plugged into a header on the main PCB.

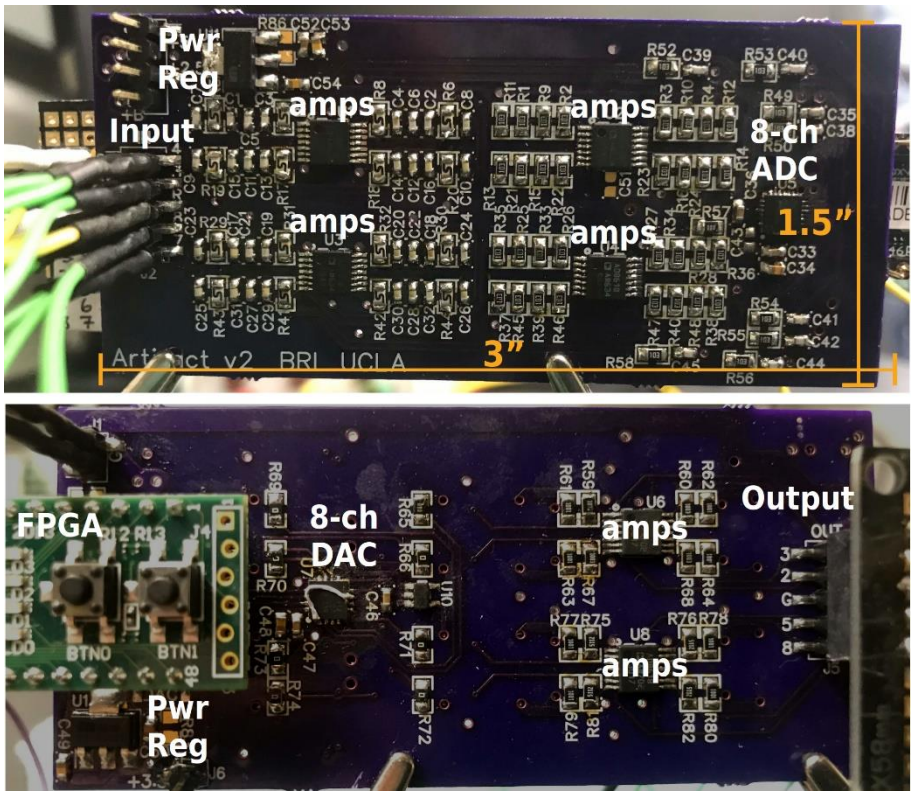

Figure 4-3. HW-M is redesigned in phase II for 8-channels of recording and is implemented on a PCB.
The PCB contains the amplifiers, ADC and DAC, supporting passive and active components and a bus which connects to a small FPGA board (bottom left).

4.3 Software Module Implementation

The SW-M is redesigned to comply with new requirements of the target application (as in Section 2.4). The development process of this module explores commonly used multi-channel artifact removal techniques, where the efficacy of these techniques is inferred from stimulation artifact models. The models generate the expected waveform of the artifacts at and around the site of stimulation, and the relationships between the waveforms are analyzed. The analysis shows that the basic assumption required for commonly used techniques does not hold for our target application. To suit the application, we instead advance an alternate approach.

The selected approach, which is described later, requires the artifacts to be intact prior to their final cancellation process, which scales an artifact from a subthreshold stimulation, naturally evoking no neural responses, to fit and subtract the artifact of desired, full amplitude, which contains the sought evoked response. The HW-M front-end suppresses the artifacts in the recorded signals and does so by a non-linear transformation, resulting in artifacts that don't resemble their initial shape. To recover the initial shape and execute the intended algorithm, the signal's artifacts are reconstructed in a preprocessing step, which reverses the HW-M's transfer function. Part of this function is predetermined by design, other relevant transformation data is streamed from a serial interface added to the HW-M in Phase II design (Figure 4-2 (b)), and yet other parameters need to be precisely fine-tuned for reconstructed signal fidelity. The reconstruction function and calculation of its parameters are discussed below.

4.3.1 Signal-Reconstruction Transfer Function

Precise signal reconstruction is required to allow common multi-channel signal processing methods to fully separate the low amplitude EPs from the much larger amplitude multi-channel artifacts. As the artifacts are suppressed by the HW-M to prevent saturation and loss of recording signals, the artifacts' signal components in multiple channels are altered by a non-linear transfer function (i.e. subtraction of quantized ADC/DAC waveforms from the signal). This nonlinearity prevents a multi-channel algorithm from correctly extracting the artifact from the signal and removing it.

The reconstruction reverses the transfer function governing the HW-M's artifact suppression. The suppression is reversed when the residual signal is referred back to the point where the digital subtraction occurred, and then the stored digital template is added back according to the transfer function. Although the transfer function is known by design, some of its parameters

are known imprecisely with respect to the sensitivity of the SW-M artifact removal algorithms. Thus prior to applying the algorithms, the key parameters of HW-M's transfer function are precisely estimated using an optimization approach discussed below. This estimation has to be conducted only once for each fabricated prototype of the HW-M, as the parameters are defined by the physical circuit components and are thus fixed.

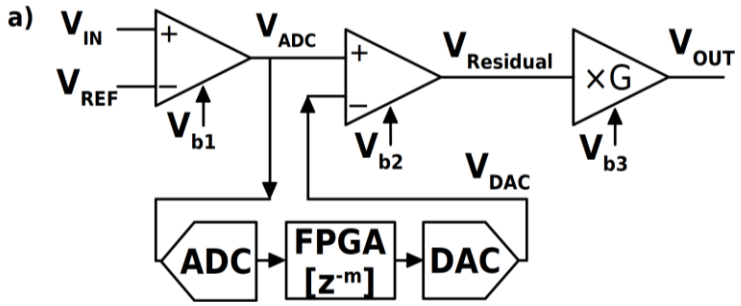

Figure 4-4. System block diagram shows the transfer function parameters that need to be optimized during signal reconstruction.

The signal recorded by the system passes through the HW-M's circuits illustrated in high-level block diagram of Figure 4-2 (b). Figure 4-4 expands the diagram and highlights the module's architecture with key parameters in question. These parameters are amplifier biases, output stage gain and time latency (in number of samples) between stimulation trigger and Hardware artifact subtraction (V_{b2}/V_{b3}, G, m). The corresponding characteristic equation 4-1 is:

$$V_{OUT} = [(V_{IN} + V_{b1} - V_{DAC} \times z^{-m} + V_{b2}) - V_{b2}] \times G + V_{b3} \quad (4\text{-}1)$$

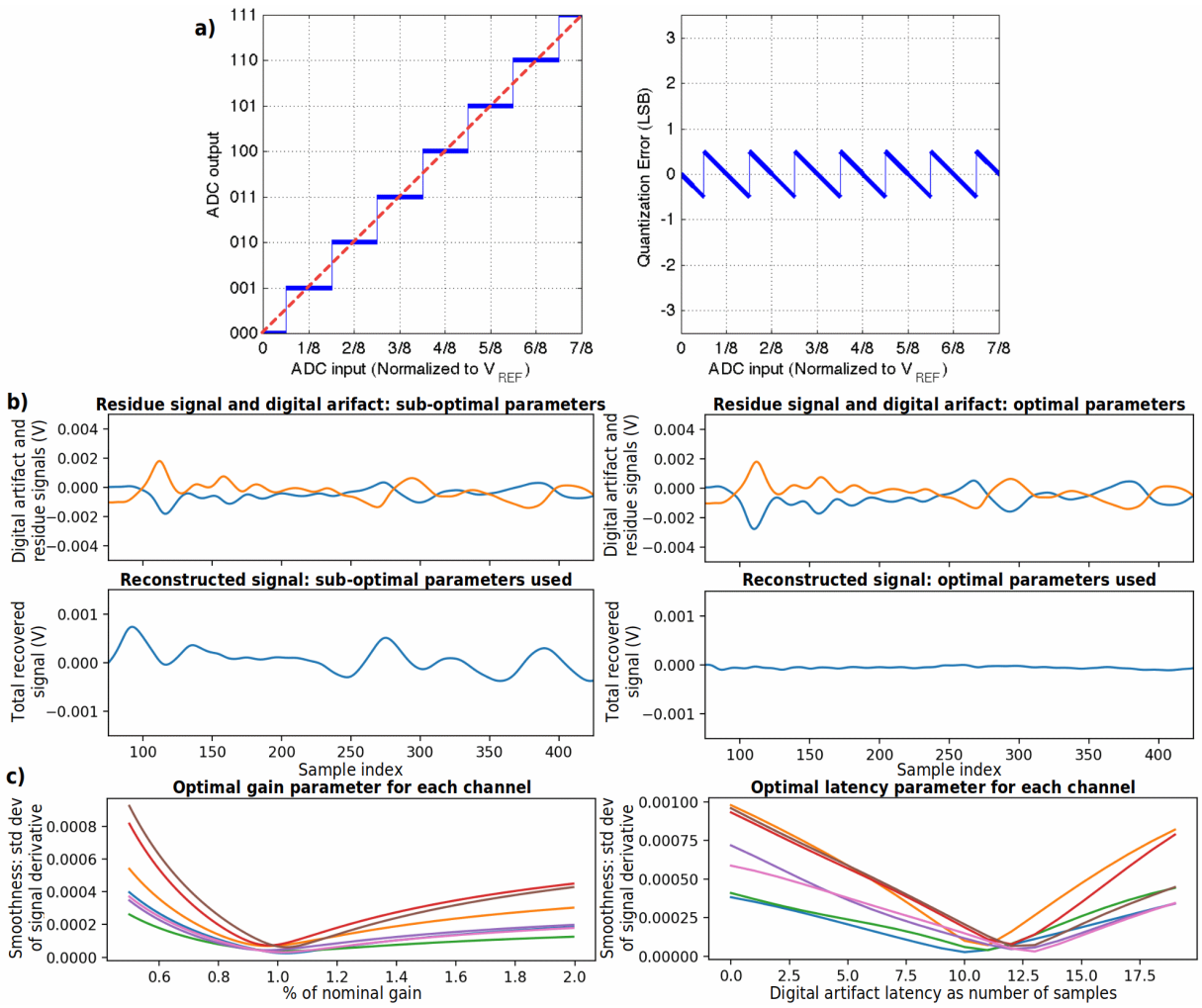

Figure 4-5. Optimization of parameters during the reconstruction process.
a) digital template quantization leaves a residual signal. b) misalignment or incorrect gain during the residue normalization contaminates the reconstructed signal with a large quantization error. c) optimization curves select the best parameters to achieve the smoothest reconstructed signal.

The bias term helps correctly normalize the recorded residual signal to its DC level at the V_{ADC} node. At this node, the signal is $V_{ADC} = V_{IN} + V_{b1}$. Additionally, the biases of the amplifiers in the 2nd and 3rd stages are equal ($V_{b2} = V_{b3}$). Rearranging the terms: $V_{ADC} = [(V_{OUT} - V_{b3})/G] + V_{DAC} \times z^{-m}$. The Vb3 can be easily and precisely measured as a circuit on the HW-M's which sets the bias of the amplifiers. The exact V_{DAC} digital signal is recorded as a bit stream from HW-M

during recording of the analog V_{OUT}. This leaves the parameters G and z^{-m}, which are fine-tuned by an optimization process.

This optimization process requires a criterion, such as error function, to minimize. Here such error results from mismatch between quantization waveforms present in digital V_{DAC} signal and the analog V_{ADC} signal derived from V_{OUT} as above, as illustrated in Figure 4-5. Figure 4-5 (a) explains the concept of quantization error, where the ADC/DAC represents a signal quantized to a limited choice of levels, leaving a residual difference to the input signal. A perfect reconstruction of the original signal happens when the residual is transformed back to the original state it was in at the circuit node where the ADC/DAC performed the quantization. Then the quantized digital waveform is added back at the exact times where each digital sample was taken and subtracted. This again points back to the need of precise calculation of the transformation parameters in amplitude and timing. The timing and amplitude matching are shown in Figure 4-5 (b). These parameters directly control the distortion of the reconstructed signal as illustrated in Figure 4-5 (c). This also demonstrates the sensitivity to the precision of the parameters. A small mismatch in G and z^{-m} leads to quantization noise imposed on the signal with levels well above the EPs, making the latter impossible to recover.

The optimization of the parameters is performed by first taking an estimated amplification gain, G, set by the nominal values of feedback resistors in output amplifier stage, and the estimated latency n, as zero samples (which translates to time as $t=n/f_S$). Then a linear search is performed while signal smoothness is measured as the optimization criteria, i.e.:

$$(G, z^{-m}) = argmin(\ \sigma(\ f(G, z^{-m})[n+1] - f(G, z^{-m})[n]\ )\ ) \tag{4-2}$$

The derivative of a smooth signal changes slowly and thus has a lower variance sample-to-sample, while that of a non-smooth noisy signal has abrupt changes sample-to-sample and thus

higher variance. The resulting optimization curves have unique global minimums (Figure 4-5 (d)), thus precisely estimating the best parameter set for the reverse transfer function which reconstructs the full input signal.

4.3.2 Simulations and Analysis of Multi-channel Artifact Models

To advance our insight on the artifact forming on multiple channels of an electrode array during stimulation, we further explore how they are generated and the relationship between them. Here, the interface of each electrode channel on a custom spinal-cord epidural array manufactured by our lab [47] and of a ground electrode are modelled with corresponding Randles cell electronic circuit components [15]. The circuit values were derived using Electro-Impedance Spectroscopy on a sample of such array following procedure in [47]. The resulting complete circuit is then simulated using LTspice SPICE circuit simulator (version XVII; Linear Technology, Analog Devices, 2019) which generates the expected artifact waveforms (Figure 4-6 (b, c)). Close inspection of the resulting signals reveals how the shapes of the artifacts are influenced by each circuit block: electrode-tissue interfaces at each recording electrode, ground/return electrode, and the resistivity of the tissue and cerebrospinal fluid (CSF). These three segments are effectively in series in the path of the current flow from the stimulation site to current's return terminal. Thus, following Kirchhoff's voltage law, the artifacts on each channel are described as the sum of time domain voltage signals formed across these components:

$$V_{stim\ chan\ S} = V_{stim\ elect.interf.} + a_S \times V_{saline} + V_{GND\ elect.interf.}$$

$$V_{non-stim\ chan\ N} = a_N \times V_{saline} + V_{GND\ elect.interf.} \quad (4\text{-}3)$$

The equation set 4-3 highlights that all three components define the artifact on the stimulating electrode, while only two components (excludes the Randles cell of the stimulating

electrode) define the artifact on the adjacent electrodes. The Randles cells of non-stimulating electrodes do not affect the artifact waveforms as they do not fall onto the current path - the amplifier recording those electrodes has a high input-impedance by design, and thus does not draw any current.

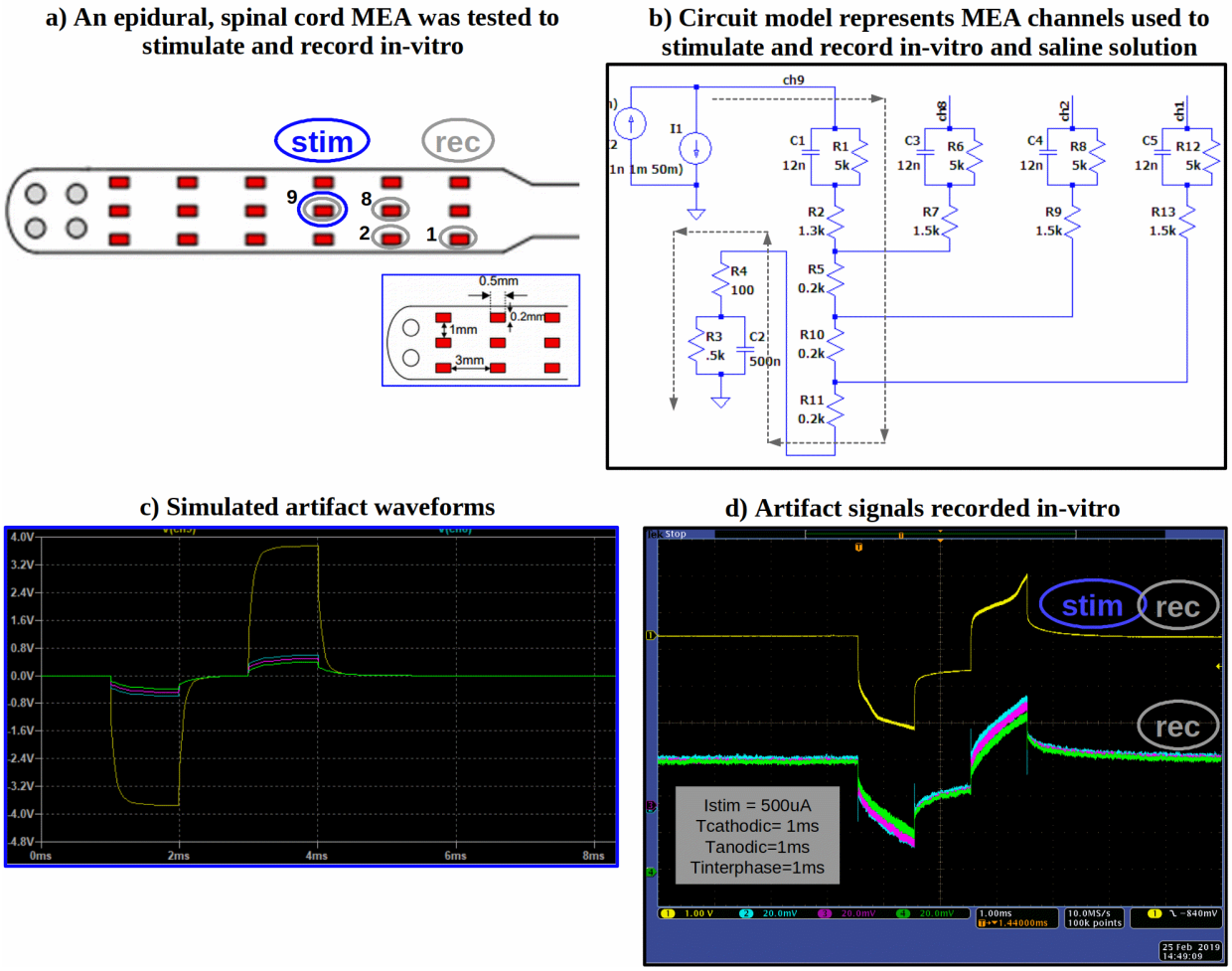

Figure 4-6. Modelling of stimulation artifact in a multi-electrode array.
a) An epidural spinal cord MEA was used in a saline solution to stimulate and record from the same channel as well as adjacent channels. b) A circuit model using Randles cells and resistive divider was created to describe the MEA and tissue, CSF or saline interaction during stimulation. c) SPICE simulator was used to predict the artifact waveforms on all recorded channels. Results show that the non-stimulation channels exhibit artifacts that are similar in proportion, while the stimulation channel artifact is uniquely different. d) waveforms are captured on the oscilloscope screen and confirm the conclusion of the model, which states that the stimulation channel has a unique artifact waveform when compared to other channels.

Two conclusions are made from this analysis. First, the artifacts on the non-stimulating electrodes are likely to be very similar in shape and are attenuated according to their distance from the stimulation site. This is because this distance correlates to the resistance of saline from the location of recording to the ground electrode, thus linearly scaling V_{saline} in equation 3-3. Second, the artifact at the stimulation site, which is uniquely defined by the electrical response of its own electrical tissue interface ($V_{stim\ elect\ interf}$), is in contrast expected to have a significantly different waveform. These conclusions are confirmed by the in-vitro measurements captured by an oscilloscope in Figure 4-6 (d). Blue, magenta and green traces from non-stimulation electrodes are overlaid to show the similarity among the shapes of their that only differ in attenuation of their amplitudes. The yellow trace is the waveform on the stimulating electrode which has a unique shape, as predicted by circuit analysis above. The in-vitro artifact shape of the stimulating electrode exhibits features not seen in the corresponding electrode in Figure 4-6 (d), specifically around the peaks. These features are attributed to second order effects, such as non-reversible reactions and chemical interactions at the electrode tissue interface in the presence of injected current flow during stimulation, which cause other non-linear behaviors. These non-linearities cannot be easily modeled by circuit components and are not necessary for further developments of our artifact cancellation algorithm. It suffices to take away the consistent uniqueness of the waveform of the artifact on the stimulus electrode, compared to others.

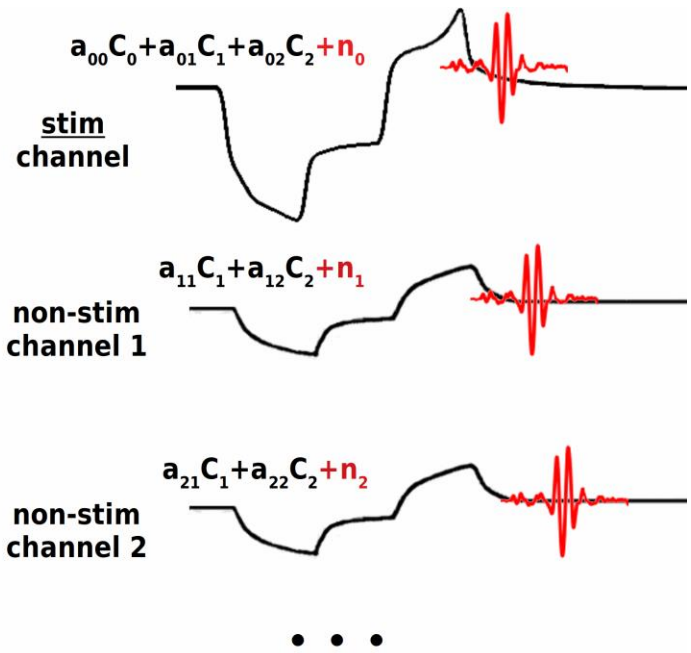

Figure 4-7. Artifact waveforms can be modelled as a sum of signal components.
The stimulation channel's artifact contains a unique signal component but also shares common components with non-stimulation channels. Neural signals are treated as an additional component. This relationship among multi-channel artifacts can be exploited by component analysis such as PCA.

4.3.3 Implementation of The Multi-channel Artifact Cancellation Algorithm

To complete the SW-M and the full cancellation of the artifact within the system's signal flow, we seek an optimal algorithm which can take advantage of the information in the multi-channel artifact models created above. Our circuit model predicted that a combination of three mathematical components, when properly scaled, can describe the artifact of both the stimulation channel and the adjacent channels. In a practical situation there will also exist components representing neural signals at one or more channels, which will be superimposed onto the artifact components. We then can initially propose that a correctly selected component analysis tool will be able to extract the components differentiating the artifacts on multiple channels and then separate them apart from the remaining components representing the underlying neural signals (Figure 4-7). Such separation of components can be performed by well-suited multi-channel

artifact extraction techniques such as PCA, discussed earlier in Section 2.3.2. The application of PCA to the proposed multi-channel artifact model is examined here by signal analysis.

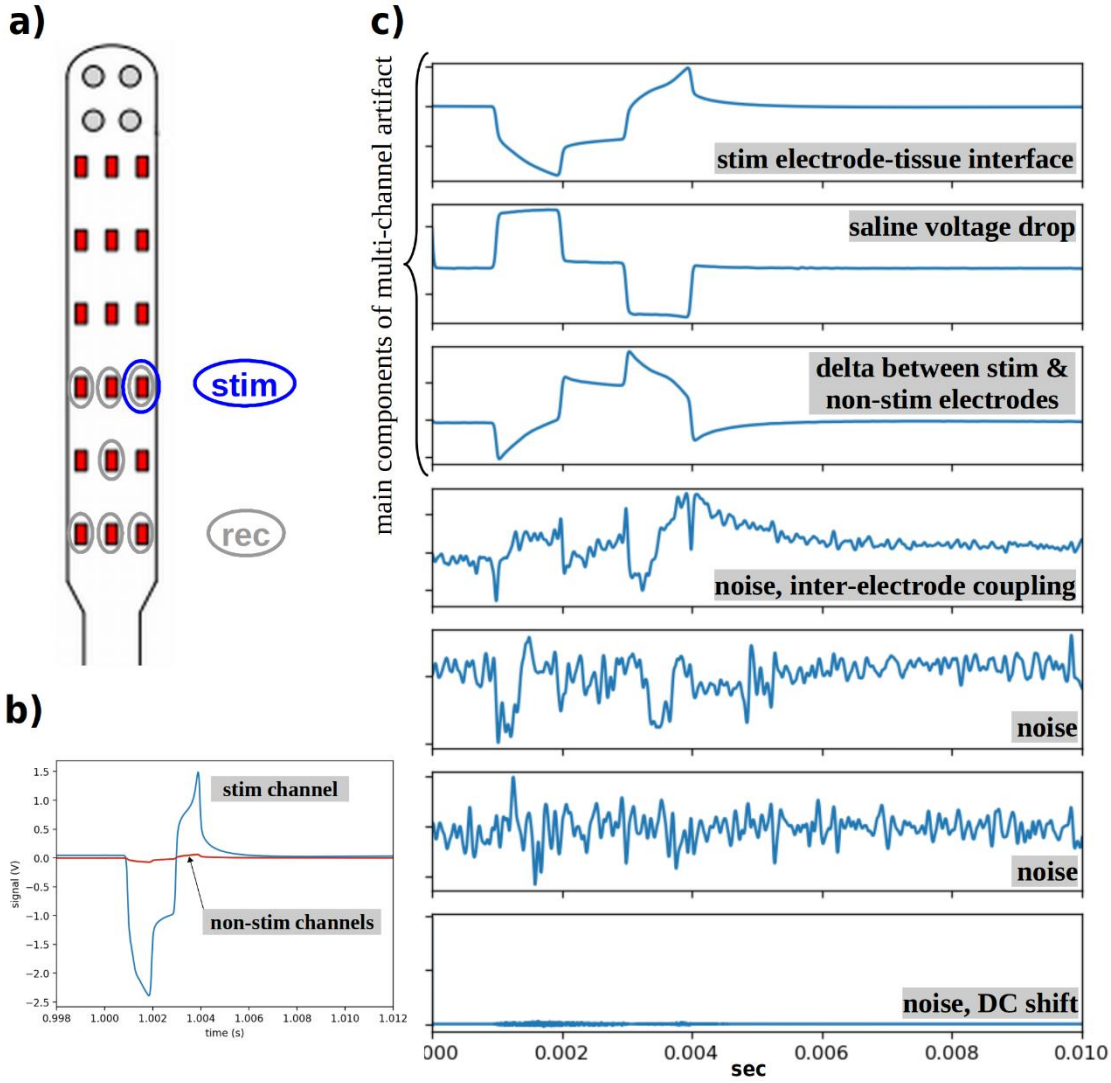

Figure 4-8. PCA identifies most distinct components of multi-channel artifacts.
a) The epidural MEA is stimulated under the same monopolar protocol. Seven channels are recorded including locus of stimulus. b) The artifacts resemble the same waveforms previously observed. c) PCs are displayed in the order based on the amount of variance they explain, starting with the most significant one. The top three PCs represent components with amplitudes which are large and are well above the system's noise level in the recorded signal. The remaining PCs capture components comparable to noise levels.

Further in-vitro testing was repeated to evaluate the resulting artifacts mathematically. The same epidural MEA and saline solution were used, but with a seven-channel electrode

configuration setup (Figure 4-8 (a)). The resulting signals were instead recorded using the HW-M, which suppressed, amplified and reconstructed the signals per our Phase II system design (Figure 4-8 (b)). Upon visual inspection of the signals at each channel, similar waveforms are observed as compared to the previous artifacts. PCA was applied to the multi-channel signals and the PCs are plotted Figure 4-8 (c). The 10 ms signal segments under analysis were sampled at 100 ksps, resulting in 1000 sample-points per each of the seven channels. Each channel contains one artifact instance within the 1000-point dimensional space, and the maximum number of calculated PCs is equal to seven – the number of channels. These PCs form a new space reduced to only seven dimensions. The artifact at each channel can now be represented as a weighted combination of these dimensions or PCs.

The PCs are sorted based on the amount of variance they explain. The most significant components, which explain the majority of variance among channels, are at the top of the list. Judging by the smoothness of the curves of the top three PCs, we can speculate that they are above noise levels and thus are largely the descriptors of the artifact waveforms. This agrees with the previously discussed circuit model which predicts that the artifacts at all channels are composed of three major signal terms (equation 4-3). The next four PCs explain the remaining variance, but also contain significant random noise. This suggests that they describe parts of artifacts that are small and comparable to the system's noise levels.

An additional analysis is conducted to help choose a suitable number of PCs which can reconstruct and remove artifacts from signals with maximum fidelity, but without overfitting the signals. Figure 4-9 shows an average amplitude of the residual signals per channel after n PCs were used to eliminate the artifacts in the recordings. The number n is swept from one to maximum (seven) and the average residual amplitude decreases as expected. It is important to note that n>3

reduces the residual below system's noise level, which we define as "overfitting" the signals. Thus n=3 PCs is the most optimal number: it extracts the multi-channel artifacts with highest fidelity without overfitting. This again validates that multi-channel artifacts are indeed best explained by three signal components. Figure 4-8 (c) shows these top three components. The top component, PC_0 resembles the unique shape of artifact at the stimulating electrode. The second PC_1, represents the linear saline voltage drop due to the cathodic and anodic phases of stimulation. Finally, PC_2 represents the difference between the unique waveform of the stimulating electrode, and the artifact waveform of the adjacent channels, which forms largely due to the Randles cell of the ground electrode, as discussed previously.

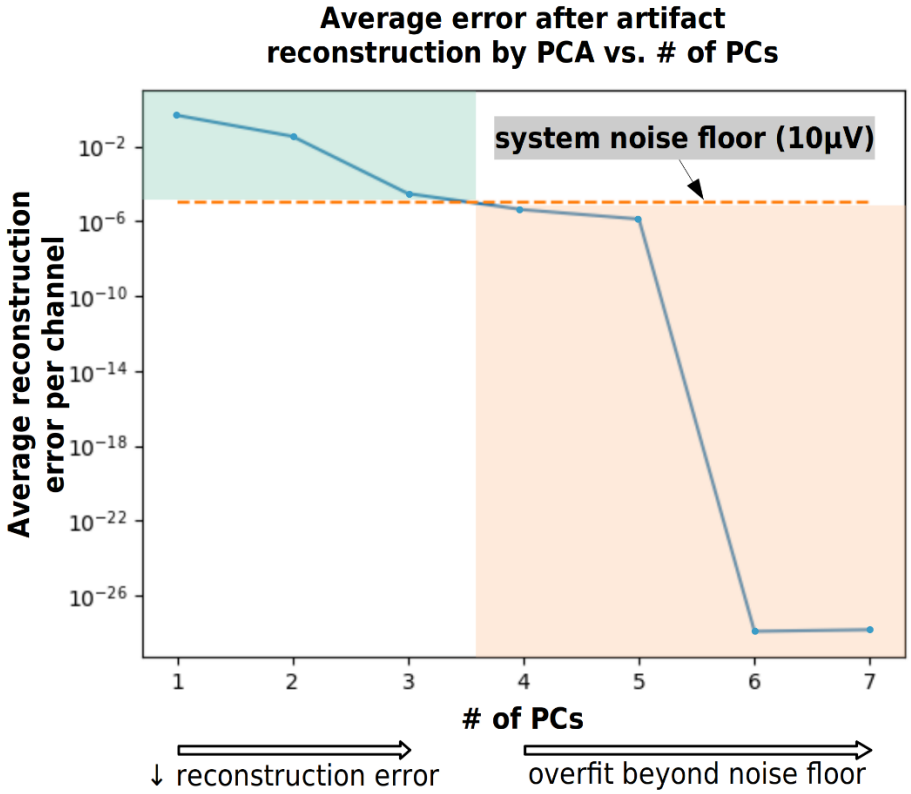

Figure 4-9. Number of Principle Components vs. fidelity of artifact removal extraction.
The plot helps choose the number of PCs that represent the artifacts with good fidelity, but without overfitting to the signal noise. Given the noise floor of the system, n=3 represents the best artifact fit, without overfitting.

Next, the artifacts at all channels were reconstructed using the top three calculated principal components (Figure 4-10 (a)). A linear combination of these components produces a good fit to all artifacts, and when subtracted from the recorded signals, retains an average residual error signal with an amplitude of 250uV or less (Figure 4-10 (b)). The error consists of second order effects, such as channel-to-channel signal coupling during recordings, that are difficult to model by the circuit components and are not reflected by equation 4-3. Although this residual error still represents an impressive reduction of artifacts, it sufficiently large to obscure the expected neural responses, which means that the PCA reconstruction will not be able to recover them. Based on these results, we conclude that in our target application, where stimulus artifacts are many orders of magnitude higher that the evoked potentials, even a correctly selected PCA method will not be able to recover the underlying evoked potentials. Thus, PCA or any similar multi-channel BSS methods are not suitable for our SW-M design. Importantly, applications that successfully employ PCA for artifact removal [16], [32], have protocols with the artifacts much smaller in magnitude and thus produce proportionally smaller residual errors and are able to recover the neural signals.

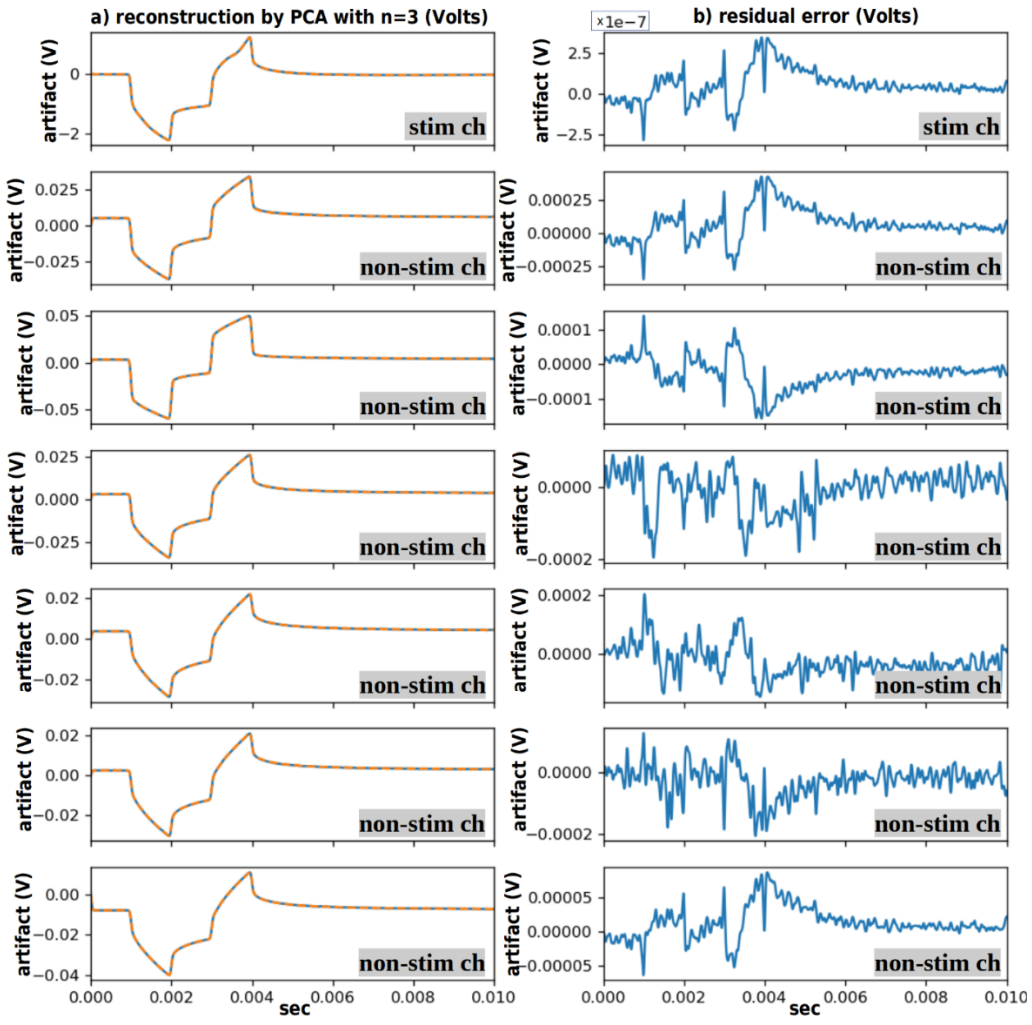

Figure 4-10. PCA is applied to multi-channel artifacts recorded with HW-M from Phase II design.

a) Artifacts are recorded from the stimulating and adjacent channels. b) One-component PCA fails to sufficiently reconstruct all artifacts. The one-component PCA template resembles waveform of stimulating channel but not the adjacent channels. This is explained by the proposed circuit model. c) Three-component PCA can reconstruct all stimulation artifacts with sufficient precision. d) Residual errors show close fit, but still insufficient to recover evoked potentials.

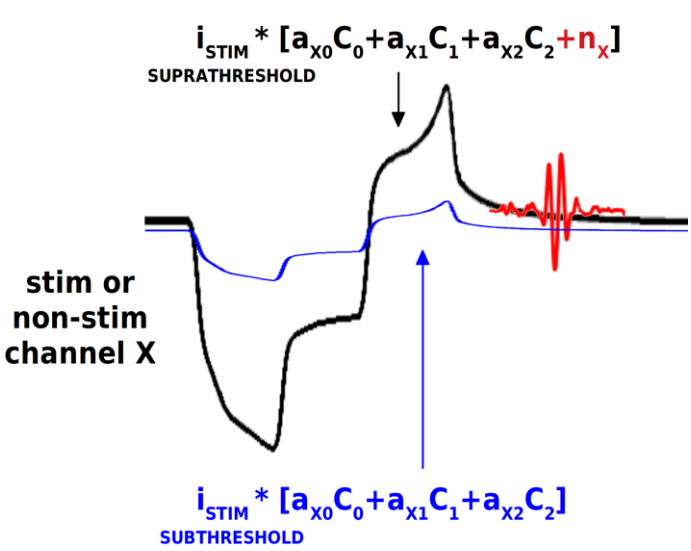

Figure 4-11. Signal components of the artifact waveform linearly scale with stimulation current to the first order.
This can be exploited to extract the neural signal for any selected channel. Subthreshold stimulation artifact does not contain a neural signal and thus can be scaled to match the suprathreshold stimulation artifact, less the neural evoked response. Non-linear and second order signal components will cause some degree of error in this method of neural signal recovery.

While we have showed that PCA is unsuitable for separating evoked potentials from artifacts for large artifacts, such is in our application, PCA has increased confidence in our artifact circuit model which can be used to develop an alternate solution. We observe that both first order and second order components of any selected channel should scale with value of the applied stimulation current, following Ohm's law (Figure 4-11). This means that a subthreshold, low-current stimulation will produce an artifact waveform, which is an attenuated version of the large-current suprathreshold stimulus artifact. Since the former does not contain a neural response, by definition, it can be scaled and used as a template to cancel the latter while preserving the neural response. This principle is explored and validated by in-vitro testing of the full Phase II system design in the Section 4.4.

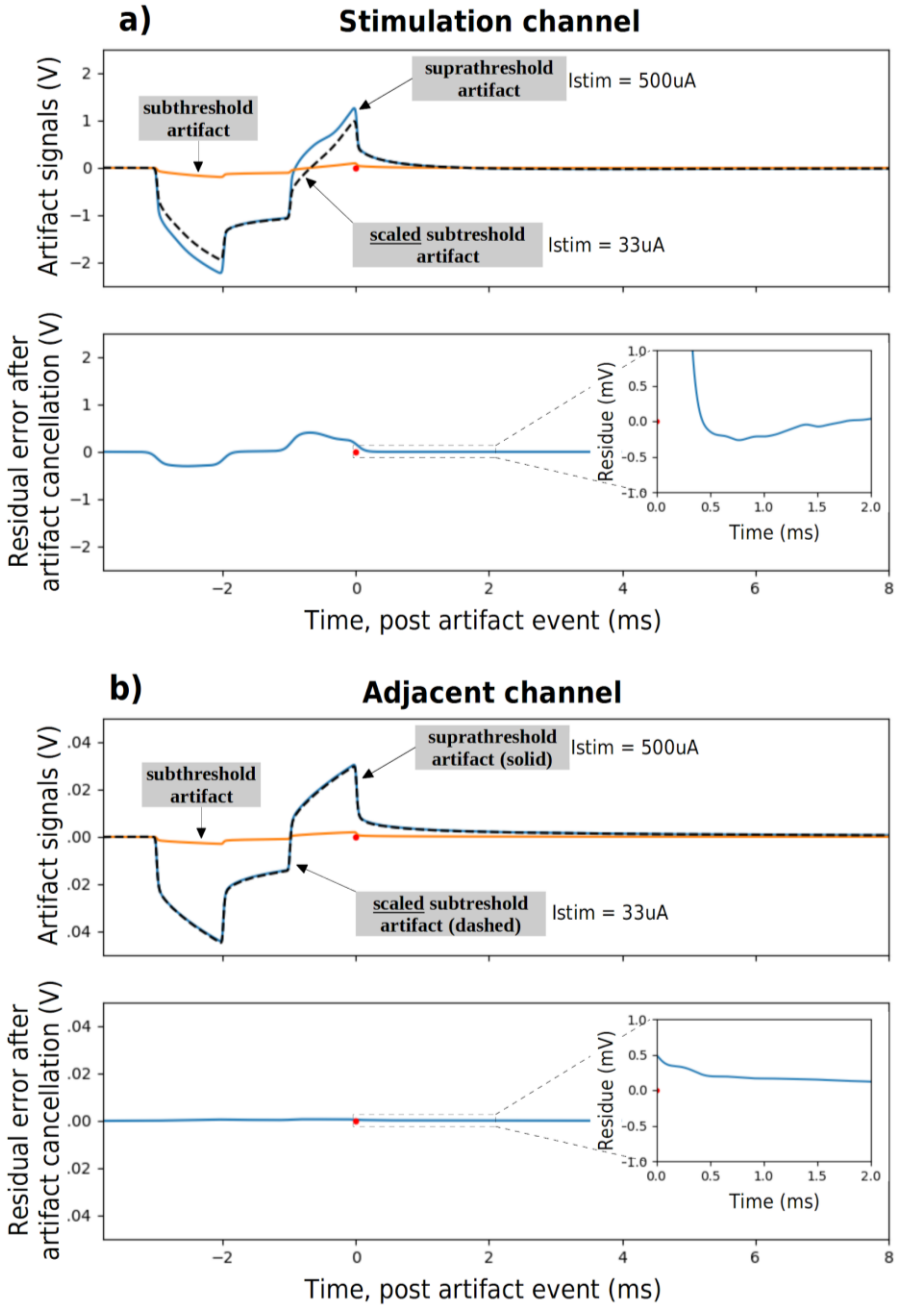

Figure 4-12. Artifact Cancellation is applied to multi-channel recordings of a biphasic, monopolar stimulation to measure system performance.
Subthreshold stimulation is recorded and linearly scaled up to subtract the artifact from the suprathreshold stimulus. (a) Artifact at stimulation channel is large and so is the residual error. The error settles to low values 0.4ms after the anodic phase of the stimulation. (b) Artifact at a channel adjacent to the stimulation site is smaller in amplitude, and so is the respective residual error after cancellation. The error is within 0.5mV immediately after stimulus current turns off. The error settles close to zero within 0.4ms post stimulus.

4.4 In-vitro Experimental Results

We begin the validation of our final artifact cancellation algorithm by collecting in-vitro data, in a setup similar to that of Figure 4-10. A monophasic bipolar stimulus is applied to one channel of the epidural MEA immersed in saline, while the stimulus channel is recorded simultaneously with an adjacent channel using the HW-M. The stimulation parameters are 500uA at 1ms per each phase: cathodic, anodic and interphase delay. The experiment is repeated using 33uA current while all else is kept the same. No neural signals are imposed on the recorded artifacts in this test. The waveforms are extracted, reconstructed per standard flow of SW-M and are shown in Figure 4-12.

The proposed final artifact cancellation is applied by scaling the 33uA signal to cancel the waveform of the 500uA signal. The scaling factor is chosen to minimize the difference between them and is plotted as the residual error in Figure 4-12 (a, b) for stimulation and adjacent channels respectively. Several takeaways are noted. First, there is an obvious mismatch between the artifact waveforms during the stimulation pulses, which is especially apparent in the stimulation channel. This suggests that the response of the electrode tissue interface in duration of the current injection does not linearly scale with the stimulus current. The is likely related to the large signal behavior, as the relative mismatch is much smaller in the adjacent channel, where the signal voltage is smaller. On the other hand, immediately after the stimulus current is turned off, during the period when the voltage at the electrodes is settling back to it's steady-state zero value, the "tails" of the scaled and full artifacts match relatively well. Specifically, the residual error at the algorithm's output settles to 0.5mV within 0.35ms post-stim in the stimulation channel and is within 0.5mV immediately post-stimulation at the adjacent channel.

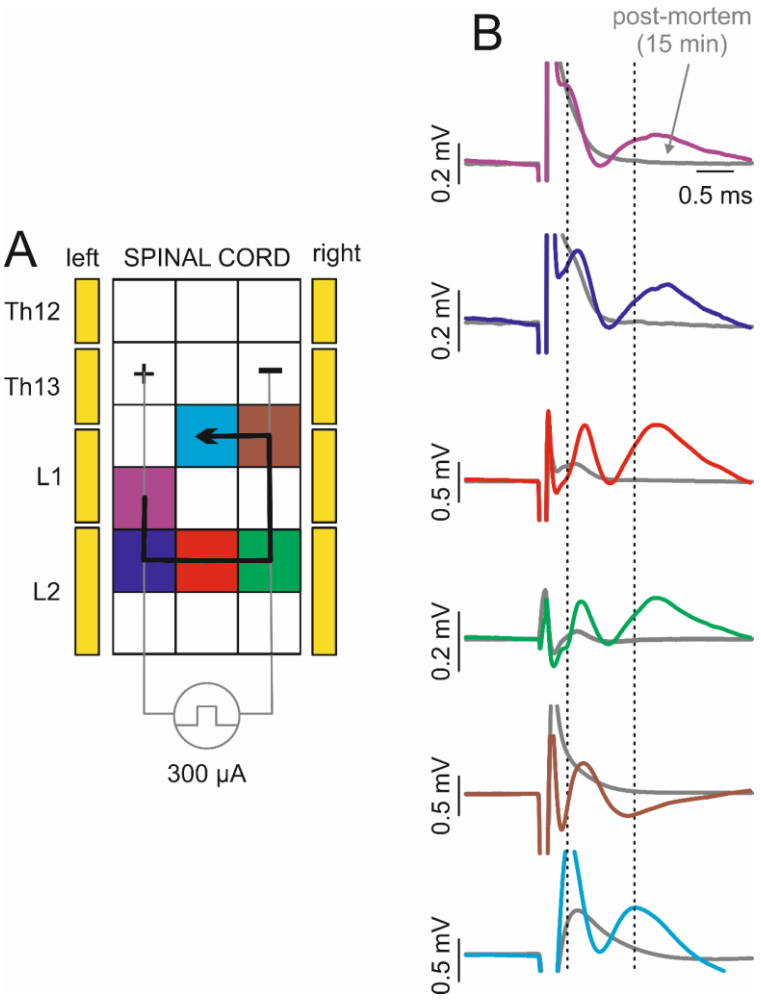

Figure 4-13. Bipolar stimulation of 300uA is applied to a pair of electrodes on the spinal cord epidural MEA in-vivo on an animal model during work in study [13].
Electrical potentials (B) are recorded from the surface of the cord by the MEA (A) from the electrode with the corresponding color. The responses to stimulation appear 0.5ms or later post-stimulus event. Dotted vertical lines help notice the time-staggered nature of Evoked Responses. Signals are recorded by a standard neural amplifier and are distorted due to stimulation artifacts. Signals at stimulation electrodes are fully inaccessible due to large induced artifacts.

The quality of this result can be assessed relative to a chosen experiment protocol, based on its neural signal responses and their timing to stimulation, and similar requirements. To identify these parameters for our target application, a preliminary investigation was performed in-vivo under work [13]. As explained in Section 2.4, epidural stimulation of the spinal cord was conducted to measure connectivity by capturing muscle's EMG responses. The EMGs were measured per

protocol, while the MEA electrodes were recorded in parallel. Repeated measurements have revealed multi-channel evoked potentials in response to stimulation (Figure 4-13). The responses exhibit the expected features of spinal cord potentials, as documented in [59], which investigated the nature of the potentials in response to activation of monosynaptic pathways. It is evident from our MEA recordings that the signals of interest appear 0.5ms post artifact and have amplitudes between 0.2mV and 0.7mV depending on the contact between the implanted epidural electrode and the dura tissue. These parameters fit within the performance of our proposed artifact cancellation algorithm. In addition, the signals are distorted due to the stimulation artifacts present, and the channels at the site of stimulation are impossible to record as was introduced in Chapter 2. This confirms that recording epidural potentials by spinal cord stimulation is a feasible application for our system.

We emulate a similar experiment in-vitro and further validate our multi-channel design. The MEA is immersed in saline and stimulated with a bipolar, monophasic current at 300uA for 0.1ms, repeating the protocol in Figure 4-13. The location of cathodic and anodic stimulus is shown in Figure 4-14, bottom right. Again, two sets of data are collected: a multi-channel artifact recorded at seven electrodes, two of which are the loci of stimulation, and an additional set of artifacts generated by subthreshold current of 33uA (Figure 4-14, left column). The signals contaminated by suprathreshold artifact also contain superimposed spinal cord evoked potentials, while the subthreshold artifacts do not. The superimposed potentials vary in latency to the stimulus for each channel, imitating an in-vivo scenario, with earliest responses at the stimulation electrodes and higher latency ones at more distance locations. Again, the standard recording flow of the HW-M and SW-M is applied, including the artifact cancellation algorithm. The 33uA subthreshold curves are then scaled (Figure 4-14, middle column) and subtracted from the 300uA waveforms. The

resulting difference is plotted in Figure 4-14, right column. The time scale is set to zero at the end of stimulus pulse and a red dot is placed on the plots to mark this time. The recovered evoked potentials are clearly visible at the output of each channel. The plots of non-stimulation channels notably show these evoked responses without any significant distortion, unlike the in-vivo test described earlier in Figure 4-13, which used a standard neural amplifier. In addition, the evoked potentials at stimulation electrodes are captured as well, while this was impossible in the case of the standard amplifier. The stimulation electrode recordings exhibit distortion of the signal in the first 0.5ms, as is expected based on our preliminary algorithm assessment in Figure 4-12. The major peak of the evoked potential (or inverted peak in the case of the bottom plot with cathodic stimulation) is still visible. Thus, the proposed Phase II artifact cancellation system allows the user to trace the time sequence of the evoked potential events and thus the connectivity of the network in the spinal cord (Figure 4-14, bottom right). Unlike other published work which used an artifact cancellation approach applied to this scenario ([60]), this design allows adequate view of the spinal cord's responses at each electrode of the array, including the stimulating electrodes, and avoids loss of the recorded signal.

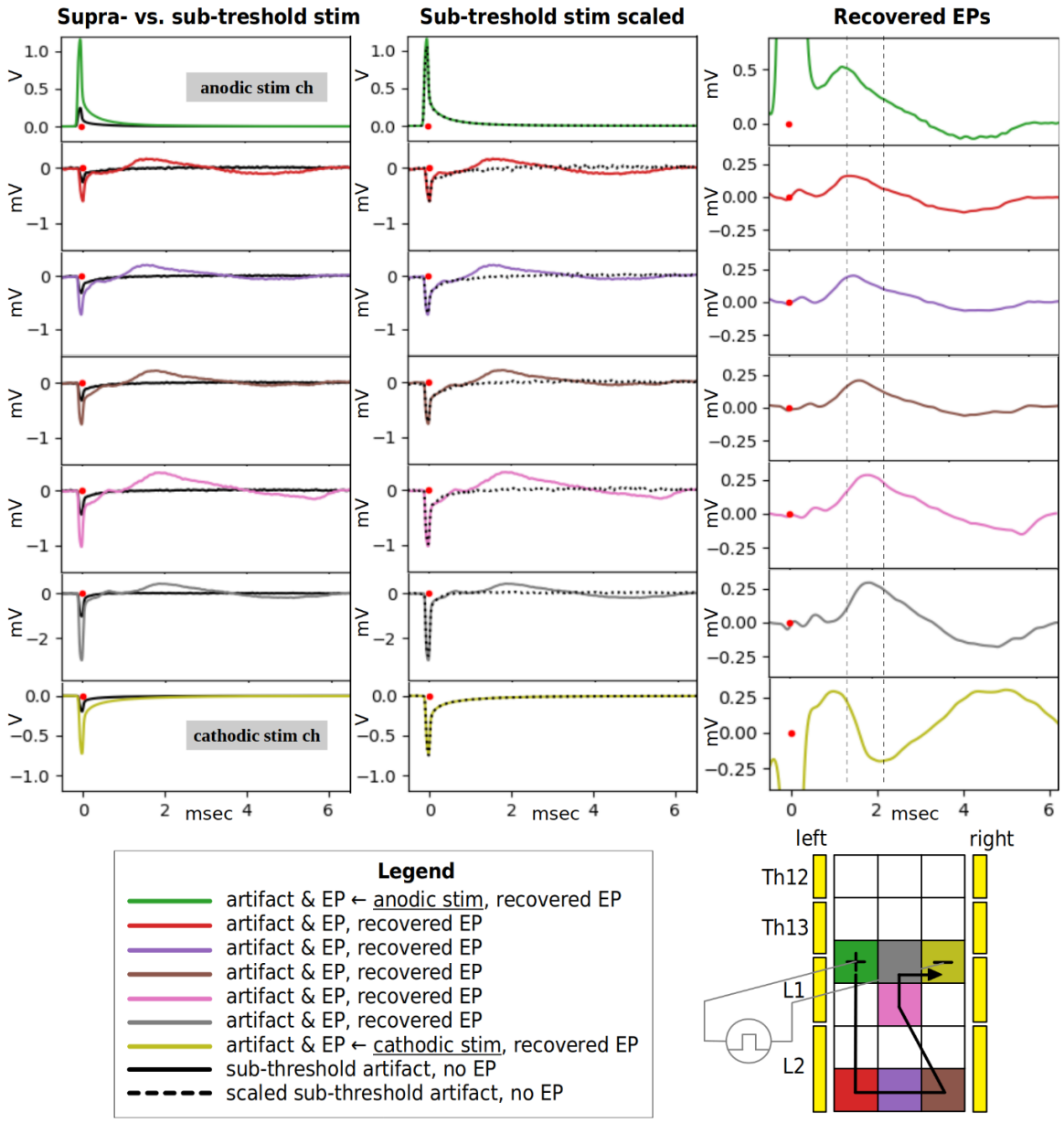

Figure 4-14. The full artifact cancellation system with the proposed software algorithm component is tested in-vitro, emulating the protocol of the target application.
The MEA is stimulated in saline at 300µA with a 0.1ms bipolar monophasic pulse applied to channels green and yellow channels. Seven electrodes are recorded simultaneously. Emulated spinal cord evoked responses are superimposed onto the electrode signals. The protocol is repeated with 33µA subthreshold pulse without evoked responses. Artifact cancellation is applied, and the responses are recovered (right). The bottom, cathodic electrode reveals an inverted evoked response. Both stimulating electrodes (top, bottom) show distortion in the recovered responses, but notably preserve the location of the major peak of the signal. The remaining responses are recovered with minimal distortion. The readings allow tracing of timing of the evoked potentials, thus identifying the connectivity of the spinal cord's neural network (bottom right).

4.5 Discussion

4.5.1 Efficient Implementation of HW-M for High-Channel-Count Recordings

High density MEAs with growing number of electrodes support signal recording from neuronal populations on an increasingly larger scale. This follows the key goal of neuroscience and medical applications in accessing a more complete view of information processing in the brain for research and neural therapy, respectively [61]. The scaling of the MEA channels requires an equivalent scaling of the number of inputs in the recording electronics. Since the architecture of the HW-M presents an overhead in hardware components which suppress the stimulation artifacts in the signal, its efficient implementation is essential to minimize the power consumption, design complexity and overall device size.

The proposed efficient approach groups channels with similar artifact magnitudes to share a single artifact feedback signal, which effectively shares a single ADC and DAC channels (Figure 4-15). This is possible because after subtracting the artifact approximation $\tilde{a}$ from the artifact a_n at any given channel n within the group, the error ($\Delta a = a - \tilde{a}$) only needs to be smaller than the input compliance voltage of the gain amplifier, as explained in Section 3.1.2.

Figure 4-15 illustrates that the artifact magnitude is similar at all electrodes equidistant to the site of stimulation. Thus, a planar electrode array with n^2 channels or 3D array with n^3 channels will only require on the order of n hardware-feedback ADC/DAC channels. Additional ADC/DAC channels can be added if an electrode array spans multiple tissue structures, where artifact waveform changes across the barrier between them. Finally, any distant electrode which records an artifact small enough to avoid risk of saturation, doesn't require any cancellation circuitry and can be recorded with standard amplifiers directly.

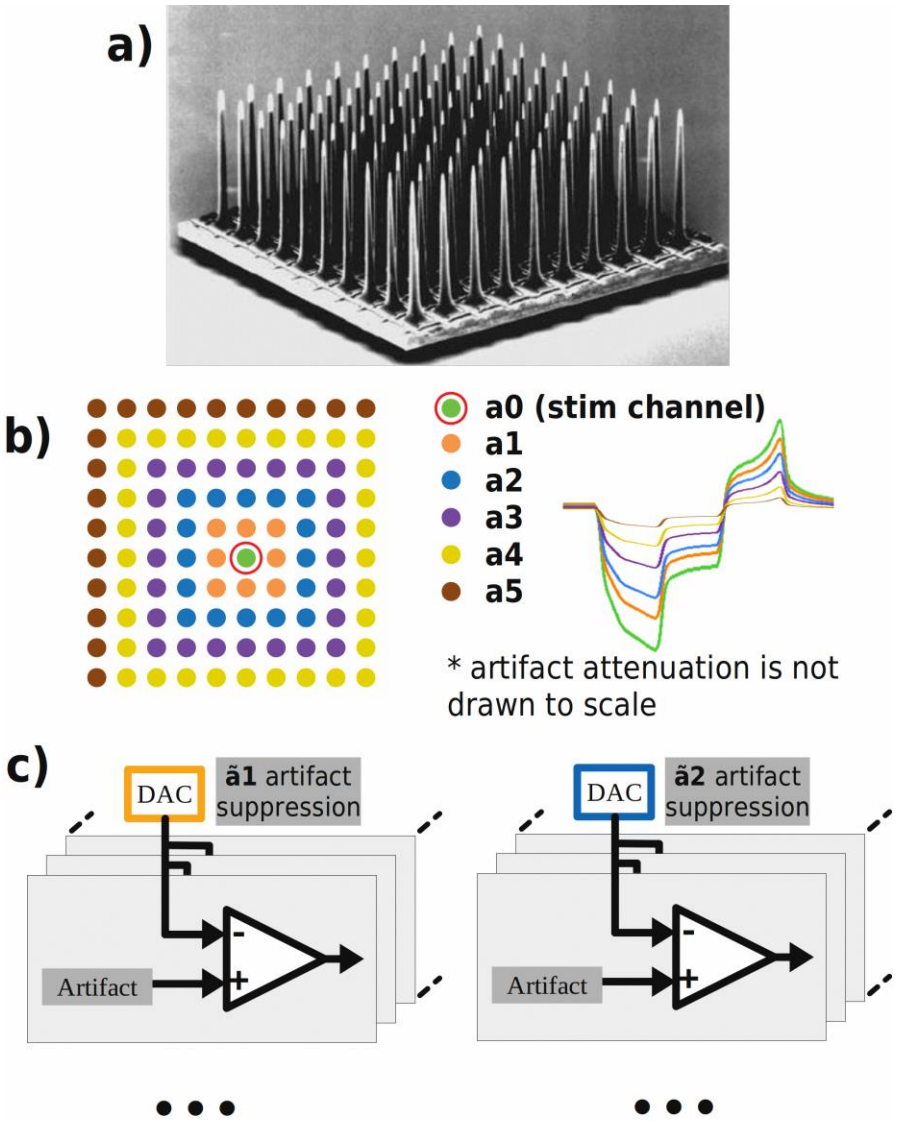

Figure 4-15. Artifact cancellation in high-channel-count recordings through an MEA can be accommodated by fewer count of artifact-suppression circuits.
a) Utah MEA can be used for neural connectivity study [62] by stimulation and recording. b) electrodes equidistant to the locus of stimulation have artifacts with approximately similar amplitudes. c) a single ADC/DAC artifact suppression channel can subtract from multiple amplifiers with signals with similar sized artifacts. Thus a MEA with n^2 electrodes can be accommodated by just n ADC/DAC channels.

To illustrate this more concretely, we have analyzed in-vitro and in-vivo examples of multi-channel recordings and quantified the delta between artifacts at different electrodes with respect to the error tolerance Δa of the HW-M amplifier. In our HW-M implementation, the amplifier requires $\Delta a < 5mV$ (Section 3.1.2).

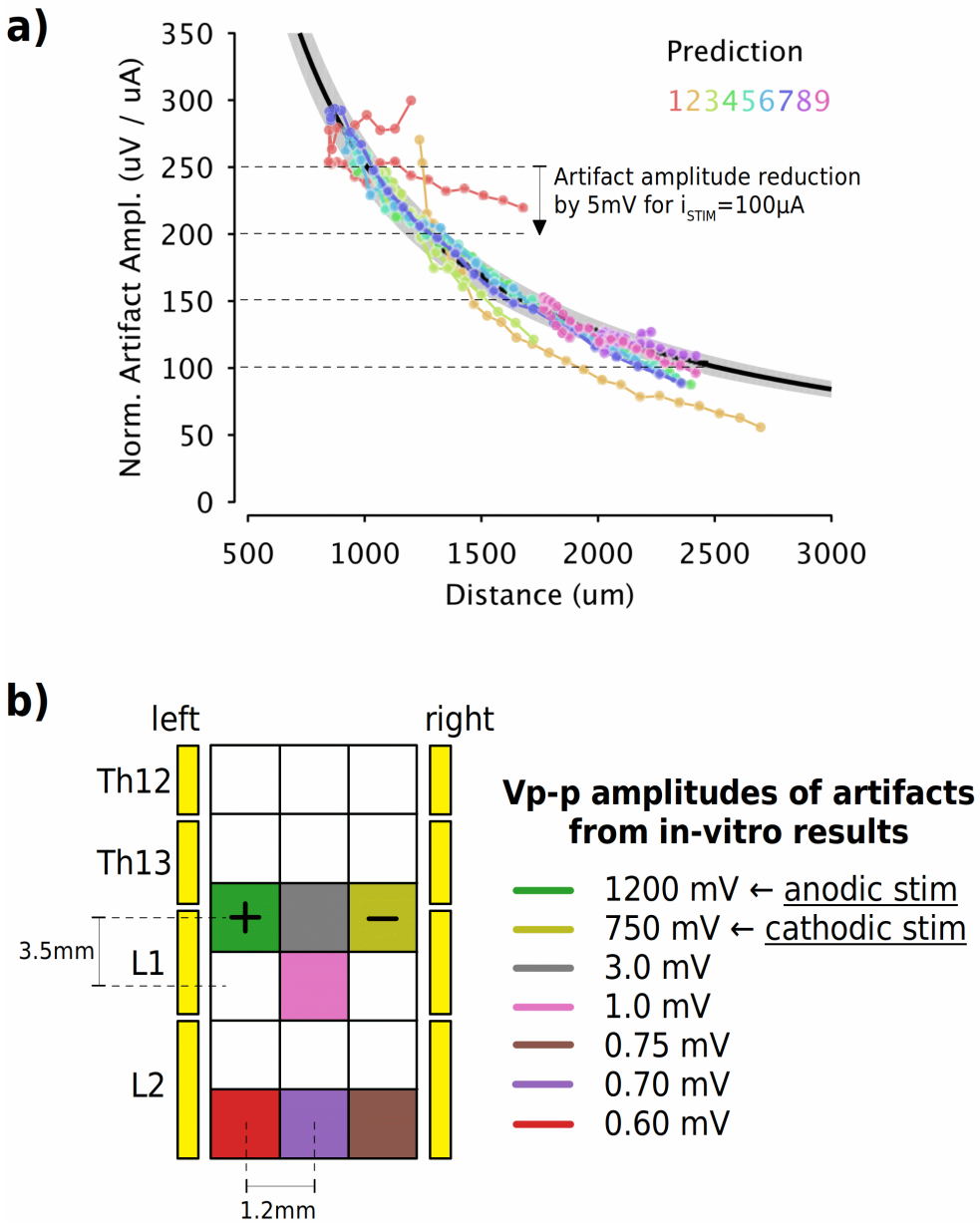

Figure 4-16. In-vivo and in-vitro examples of artifact attenuation with distance.
In our HW-M implementation, residual artifact can be ≤ 5 mV without incurring saturation. Thus, recording channels can be assigned to artifact-suppression groups with amplitudes similar by a 5 mV margin. a) Work [16] plots stimulation artifacts at various electrodes in the implanted array. A curve is fit to approximate the relationship between normalized amplitude and the distance from site of stimulation. 17 electrodes can be assigned to just three artifact suppression groups. b) In-vitro testing of the proposed multi-channel system records seven stimulation artifacts. The seven channels can be assigned to just 3 groups based on the 5 mV margin.

Work [16] uses a shank electrode array with channels uniformly positioned along the length of the shank. The authors quantified the amplitude of the stimulus artifact, normalized by the

stimulating current, at each channel as a function of distance of this channel from the locus of stimulation. The normalization of the amplitude by current is justified similarly to our approach in Phase II algorithm: the signal voltage of the artifact components linearly scales with the stimulus current, following Ohm's law (Figure 4-11). The resulting attenuation of artifact vs. distance from work [16] is shown and annotated in Figure 4-16 (a). From this plot we can derive approximate examples of artifact amplitudes along the channels in the recording shank electrode array. We assume an i_{stim}=100 μA, which is on the same order as the threshold for muscle activation, as noted by the authors. Then the channel closest to locus of stimulation, 1mm away, is expected to have an artifact of 25 mV. Any channels with artifacts within the 5mV delta will be grouped together: 25 mV-20 mV, 20 mV-15 mV, 15 mV-10 mV. These amplitude groups correspond to distances 1 mm, 1.3 mm, 1.7 mm, 2.5 mm. Using the purple trace, we count the number of electrodes (marked as dots on the curve) within these interval groups as four, five and eight electrodes, respectively. Following the efficient implementation schema, a total of 17 electrode artifacts can be accommodated by just three ADC/DAC channels.

In another example we reexamine our in-vitro results from Figure 4-14. The artifact amplitudes for each recorded channel are noted in Figure 4-16 (b). Repeating electrode grouping by the amplitudes with 5 mV intervals, we find that each of two stimulation electrodes must be assigned a unique artifact suppression loop. But the remaining five electrodes are within the predefined input range of the amplifier and thus can be recorded without artifact suppression all together. Thus, in this case, seven electrode artifacts are accommodated by just two ADC/DAC channels.

The efficiency factor for each case will be found after electrode implantation and initial stimulation and artifact recording, to identify the expected artifact amplitudes, which depend on

the specific stimulation protocol, electrode spacing and electrode impedance. But in all cases, a significant reduction of feedback ADC/DAC channels is expected.

4.5.2 Implementation in Neural Interface SoC

The proposed methodology is also envisioned in a SoC neural interface as a modular design. The design will require only a limited number of artifact template (ADC/DAC) channels to accommodate many recording slices (Section 4.5.1). Each recording slice will contain a basic gain amplifier and the feedback artifact subtraction will be conducted through its bias point. Each amplifier will be assigned one of the available groups with a common artifact suppression channel. The assignment would be facilitated by a network of multiplexing switches programmed after implanting the electrode array, during initial testing and calibration.

The overhead area and power for the hardware module's digital controller would be minimal in sub-micron CMOS technologies. Finally, the software algorithm will be applied in the post-processing stages on the recorded signals.

4.5.3 Comparison to Previous State-of-the-art

Recent and past works demonstrating results with artifact cancellation by use of analog and digital design approaches are summarized in Table 4-1. To the best of these authors' knowledge, the proposed work is the first to achieve neural response recovery in-vivo while simultaneously stimulating and recording in the same electrode during large artifact events.

Table 4-1. Comparison with Other Published Works.

	[40]	[10]	[38]	[39]	[12]	[30]	**This work**
Unconstrained electrode setup?	Yes	Yes	Yes	Yes	No	Yes	**Yes**
In-band artifact rejection?	No	Yes	Yes	No	No	Yes	**Yes**
Max. tol. artifact	1.8V	10mV	100mV	10mV	10V	1.8V	**5V**
Artifact suppression ratio	80dB	46dB	N/S	42dB	24dB	N/S	**100dB**
Signal BW	1Hz-500Hz	12Hz-4.5kHz	1Hz-250Hz	1Hz-2kHz	N/S	100Hz-5kHz	**1Hz-10kHz**
In-band noise	1.6uVrms	4.5uV	2.2uVrms	5uVrms	1uVrms	4.2uVrms	**9.7uVrms**
Demonstration medium	In-vivo	Ex-vivo	In-vitro	In-vivo	In-vivo	In-vivo	**In-vivo**

Chapter 5

Conclusion and Future Work

5.1 Conclusion

The implementation of the proposed methodology demonstrates simultaneous neural stimulation and recording on the same electrode and in multi-channel designs, uniquely recovering the neural signal with minimal distortion under the presence of a superimposed stimulation artifact with magnitude approximately 100dB higher than the signal of interest. The design distributes the artifact cancellation task into a two-part solution with a novel hardware architecture at the front-end of the system, and software algorithm at the backend. The prototype is implemented using off-the-shelf components, a custom PCB, and a custom software design.

In-vitro test results using prerecorded spinal cord evoked potentials demonstrate the capability of the design to be applied to a study of neural networks of the spinal cord in animal models for purposes of advancing rehabilitation research for SCI. In-vivo experimental results with a rodent model implanted with deep brain electrode probes, show neural responses recovered in the presence of very large stimulation artifacts and recovering the underlying neural signals. This design can be used to map neural networks in tissues by recording the propagation of neural responses starting at the stimulation site. Critically, this design does not constrain its use to 1) deliberately setting the stimulation frequency to be out of band with signals of interest, 2) placing the recording electrodes symmetrically around the stimulation electrode to treat the artifact as a common-mode noise, as is done with popular state-of-the-art devices.

5.2 Future Work

The paradigms of standards in neural stimulation protocols continues to be challenged with innovative approaches to investigating, diagnosing and rehabilitating neural networks. A new methodology is emerging in the field. The new methods use pre-recorded biological signals to stimulate the test subjects [63]–[65]. This approach can be labeled as “biomimetic stimulation”. Our work with spinal cord injury animal models has investigated one such method [13]. An EMG signal recorded from a rodent, containing stepping pattern is replayed and injected back into the spinal cord. The initial hypothesis states that the variance in the signal content, both in amplitude and in frequency, makes such signal more effective at increasing excitability of neural tissue. Effective can be defined as safer, more energy efficient or for longer lasting periods of time, but further works have to be published showing such potentials of biomimetic protocols.

We have recently demonstrated a device architecture featuring the ability to administer this protocol [66]. The device is based on an implantable SoC developed by Biomimetic Research Lab at UCLA (https://www.seas.ucla.edu/IBR). This further motivates the question: why do these non-periodic protocols perform better? To effectively study the “reactions” and responses of the neural networks during the administration of such protocol, a completely new type of stimulation artifact cancellation technique and device is needed. It is our intention to evolve our current artifact cancellation system to not only remove standard periodic stimulation artifacts from neural recordings but also the new biomimetic types of artifacts. The challenge in this goal once again spans designs on the system, hardware and signal processing levels. We therefore plan to accomplish this goal in our future works.

Chapter 6

Bibliography

[1] S. Culaclii, B. Kim, Y. K. Lo, L. Li, and W. Liu, "Online Artifact Cancelation in Same-Electrode Neural Stimulation and Recording Using a Combined Hardware and Software Architecture," *IEEE Trans. Biomed. Circuits Syst.*, vol. PP, no. 99, pp. 1–13, 2018.

[2] W. M. Grill, S. E. Norman, and R. V. Bellamkonda, "Implanted Neural Interfaces: Biochallenges and Engineered Solutions," *Annu. Rev. Biomed. Eng.*, vol. 11, no. 1, pp. 1–24, 2009.

[3] M. H. Histed, V. Bonin, and R. C. Reid, "Direct Activation of Sparse, Distributed Populations of Cortical Neurons by Electrical Microstimulation," *Neuron*, vol. 63, no. 4, pp. 508–522, Aug. 2009.

[4] G. Fritsch, "Uber die elektrische Erregbarkeit des Grosshirns," *Arch Anat Physiol Wiss Med*, vol. 37, pp. 300–332, 1870.

[5] R. BARTHOLOW, "ART. I.--Experimental Investigations into the Functions of the Human Brain.," *Am. J. Med. Sci. 1827-1924 Phila.*, no. 134, p. 305, Apr. 1874.

[6] R. Chen, A. Canales, and P. Anikeeva, "Neural recording and modulation technologies," *Nat. Rev. Mater.*, vol. 2, no. 2, pp. 1–16, Jan. 2017.

[7] T. Al-ani, F. Cazettes, S. Palfi, and J.-P. Lefaucheur, "Automatic removal of high-amplitude stimulus artefact from neuronal signal recorded in the subthalamic nucleus," *J. Neurosci. Methods*, vol. 198, no. 1, pp. 135–146, May 2011.

[8] D. M. Thompson, A. N. Koppes, J. G. Hardy, and C. E. Schmidt, "Electrical Stimuli in the Central Nervous System Microenvironment," *Annu. Rev. Biomed. Eng.*, vol. 16, no. 1, pp. 397–430, 2014.

[9] J. D. Rolston, R. E. Gross, and S. M. Potter, “A low-cost multielectrode system for data acquisition enabling real-time closed-loop processing with rapid recovery from stimulation artifacts,” *Front. Neuroengineering*, vol. 2, p. 12, 2009.

[10] P. Hottowy, A. Skoczeń, D. E. Gunning, S. Kachiguine, K. Mathieson, A. Sher, P. Wiącek, A. M. Litke, and W. Dąbrowski, “Properties and application of a multichannel integrated circuit for low-artifact, patterned electrical stimulation of neural tissue,” *J. Neural Eng.*, vol. 9, no. 6, p. 066005, Dec. 2012.

[11] Geo. H. Bishop, “The Form Of The Record Of The Action Potential Of Vertebrate Nerve At The Stimulated Region,” *Am. J. Physiol. -- Leg. Content*, vol. 82, no. 2, p. 462, Sep. 1927.

[12] S. Stanslaski, P. Afshar, P. Cong, J. Giftakis, P. Stypulkowski, D. Carlson, D. Linde, D. Ullestad, A.-T. Avestruz, and T. Denison, “Design and validation of a fully implantable, chronic, closed-loop neuromodulation device with concurrent sensing and stimulation,” *IEEE Trans. Neural Syst. Rehabil. Eng. Publ. IEEE Eng. Med. Biol. Soc.*, vol. 20, no. 4, pp. 410–421, Jul. 2012.

[13] G. Taccola, P. Gad, S. Culaclii, R. M. Ichiyama, W. Liu, and V. R. Edgerton, “Using EMG to deliver lumbar dynamic electrical stimulation to facilitate cortico-spinal excitability,” *Brain Stimulat.*, Sep. 2019.

[14] D. R. Merrill, M. Bikson, and J. G. R. Jefferys, “Electrical stimulation of excitable tissue: design of efficacious and safe protocols,” *J. Neurosci. Methods*, vol. 141, no. 2, pp. 171–198, Feb. 2005.

[15] Y.-K. Lo, C.-W. Chang, and W. Liu, “Bio-impedance characterization technique with implantable neural stimulator using biphasic current stimulus,” *Conf. Proc. Annu. Int. Conf.*

IEEE Eng. Med. Biol. Soc. IEEE Eng. Med. Biol. Soc. Annu. Conf., vol. 2014, pp. 474–477, 2014.

[16] D. J. O'Shea and K. V. Shenoy, "ERAASR: an algorithm for removing electrical stimulation artifacts from multielectrode array recordings," *J. Neural Eng.*, vol. 15, no. 2, p. 026020, 2018.

[17] S. F. Cogan, "Neural Stimulation and Recording Electrodes," *Annu. Rev. Biomed. Eng.*, vol. 10, no. 1, pp. 275–309, 2008.

[18] B. H. Boudreau, K. Englehart, A. D. C. Chan, and P. A. Parker, "Subthreshold training: a novel approach to stimulus artifact cancellation in somatosensory evoked potential recordings," in *Proceedings of the 25th Annual International Conference of the IEEE Engineering in Medicine and Biology Society (IEEE Cat. No.03CH37439)*, 2003, vol. 3, pp. 2659-2662 Vol.3.

[19] T. Hashimoto, C. M. Elder, and J. L. Vitek, "A template subtraction method for stimulus artifact removal in high-frequency deep brain stimulation," *J. Neurosci. Methods*, vol. 113, no. 2, pp. 181–186, Jan. 2002.

[20] T. Wichmann, "A digital averaging method for removal of stimulus artifacts in neurophysiologic experiments," *J. Neurosci. Methods*, vol. 98, no. 1, pp. 57–62, May 2000.

[21] J. Xu, T. Wu, W. Liu, and Z. Yang, "A Frequency Shaping Neural Recorder With 3 pF Input Capacitance and 11 Plus 4.5 Bits Dynamic Range," *IEEE Trans. Biomed. Circuits Syst.*, vol. 8, no. 4, pp. 510–527, Aug. 2014.

[22] H. Chandrakumar and D. Marković, "A High Dynamic-Range Neural Recording Chopper Amplifier for Simultaneous Neural Recording and Stimulation," *IEEE J. Solid-State Circuits*, vol. 52, no. 3, pp. 645–656, Mar. 2017.

[23] W. Jiang, V. Hokhikyan, H. Chandrakumar, V. Karkare, and D. Marković, “A +/-50-mV Linear-Input-Range VCO-Based Neural-Recording Front-End With Digital Nonlinearity Correction,” *IEEE J. Solid-State Circuits*, vol. 52, no. 1, pp. 173–184, Jan. 2017.

[24] “Front Ends - Ripple Neuro.” [Online]. Available: http://rippleneuro.com/front-ends. [Accessed: 30-Apr-2017].

[25] C. Sekirnjak, P. Hottowy, A. Sher, W. Dabrowski, A. M. Litke, and E. J. Chichilnisky, “High-Resolution Electrical Stimulation of Primate Retina for Epiretinal Implant Design,” *J. Neurosci.*, vol. 28, no. 17, pp. 4446–4456, Apr. 2008.

[26] T. Wichmann and A. Devergnas, “A novel device to suppress electrical stimulus artifacts in electrophysiological experiments,” *J. Neurosci. Methods*, vol. 201, no. 1, pp. 1–8, Sep. 2011.

[27] E. A. Brown, J. D. Ross, R. A. Blum, Y. Nam, B. C. Wheeler, and S. P. DeWeerth, “Stimulus-Artifact Elimination in a Multi-Electrode System,” *IEEE Trans. Biomed. Circuits Syst.*, vol. 2, no. 1, pp. 10–21, Mar. 2008.

[28] J. W. Gnadt, S. D. Echols, A. Yildirim, H. Zhang, and K. Paul, “Spectral cancellation of microstimulation artifact for simultaneous neural recording in situ,” *IEEE Trans. Biomed. Eng.*, vol. 50, no. 10, pp. 1129–1135, Oct. 2003.

[29] S. Nag, S. K. Sikdar, N. V. Thakor, V. R. Rao, and D. Sharma, “Sensing of Stimulus Artifact Suppressed Signals From Electrode Interfaces,” *IEEE Sens. J.*, vol. 15, no. 7, pp. 3734–3742, Jul. 2015.

[30] Z. Yang, J. Xu, A. T. Nguyen, T. Wu, W. Zhao, and W. k Tam, “Neuronix enables continuous, simultaneous neural recording and electrical microstimulation,” in *2016 38th Annual International Conference of the IEEE Engineering in Medicine and Biology Society (EMBC)*, 2016, pp. 4451–4454.

[31] C. Bishop, *Pattern Recognition and Machine Learning*. New York: Springer-Verlag, 2006.

[32] D. Han, Y. N. Rao, J. C. Principe, and K. Gugel, “Real-time PCA (principal component analysis) implementation on DSP,” in *2004 IEEE International Joint Conference on Neural Networks (IEEE Cat. No.04CH37541)*, 2004, vol. 3, pp. 2159–2162 vol.3.

[33] S. Basir-Kazeruni, S. Vlaski, H. Salami, A. H. Sayed, and D. Marković, “A blind Adaptive Stimulation Artifact Rejection (ASAR) engine for closed-loop implantable neuromodulation systems,” in *2017 8th International IEEE/EMBS Conference on Neural Engineering (NER)*, 2017, pp. 186–189.

[34] L. F. Heffer and J. B. Fallon, “A novel stimulus artifact removal technique for high-rate electrical stimulation,” *J. Neurosci. Methods*, vol. 170, no. 2, pp. 277–284, May 2008.

[35] K. Limnuson, null Hui Lu, H. J. Chiel, and P. Mohseni, “Real-Time Stimulus Artifact Rejection Via Template Subtraction,” *IEEE Trans. Biomed. Circuits Syst.*, vol. 8, no. 3, pp. 391–400, Jun. 2014.

[36] D. P. Allen, E. L. Stegemöller, C. Zadikoff, J. M. Rosenow, and C. D. MacKinnon, “Suppression of deep brain stimulation artifacts from the electroencephalogram by frequency-domain Hampel filtering,” *Clin. Neurophysiol.*, vol. 121, no. 8, pp. 1227–1232, Aug. 2010.

[37] M. Yochum and S. Binczak, “A wavelet based method for electrical stimulation artifacts removal in electromyogram,” *Biomed. Signal Process. Control*, vol. 22, pp. 1–10, Sep. 2015.

[38] D. Rozgic, V. Hokhikyan, W. Jiang, I. Akita, S. B.- Kazeruni, H. Chandrakumar, and D. Markovic, “A 0.338cm3, Artifact-Free, 64-Contact Neuromodulation Platform for Simultaneous Stimulation and Sensing,” *IEEE Trans. Biomed. Circuits Syst.*, pp. 1–1, 2018.

[39] A. E. Mendrela, J. Cho, J. A. Fredenburg, V. Nagaraj, T. I. Netoff, M. P. Flynn, and E. Yoon, "A Bidirectional Neural Interface Circuit With Active Stimulation Artifact Cancellation and Cross-Channel Common-Mode Noise Suppression," *IEEE J. Solid-State Circuits*, vol. 51, no. 4, pp. 955–965, Apr. 2016.

[40] A. Zhou, S. R. Santacruz, B. C. Johnson, G. Alexandrov, A. Moin, F. L. Burghardt, J. M. Rabaey, J. M. Carmena, and R. Muller, "A wireless and artefact-free 128-channel neuromodulation device for closed-loop stimulation and recording in non-human primates," *Nat. Biomed. Eng.*, vol. 3, no. 1, p. 15, Jan. 2019.

[41] B. C. Johnson, S. Gambini, I. Izyumin, A. Moin, A. Zhou, G. Alexandrov, S. R. Santacruz, J. M. Rabaey, J. M. Carmena, and R. Muller, "An implantable 700 uW 64-channel neuromodulation IC for simultaneous recording and stimulation with rapid artifact recovery," in *2017 Symposium on VLSI Circuits*, 2017, pp. C48–C49.

[42] S. Culaclii, B. Kim, Y. K. Lo, and W. Liu, "A hybrid hardware and software approach for cancelling stimulus artifacts during same-electrode neural stimulation and recording," in *2016 38th Annual International Conference of the IEEE Engineering in Medicine and Biology Society (EMBC)*, 2016, pp. 6190–6193.

[43] "Facts and figures at a glance," 2019. [Online]. Available: https://www.nscisc.uab.edu/. [Accessed: 25-Oct-2019].

[44] P. J. Grahn, G. W. Mallory, B. M. Berry, J. T. Hachmann, D. A. Lobel, and J. L. Lujan, "Restoration of motor function following spinal cord injury via optimal control of intraspinal microstimulation: toward a next generation closed-loop neural prosthesis," *Front. Neurosci.*, vol. 8, p. 296, 2014.

[45] G. Courtine, R. van den Brand, and P. Musienko, “Spinal cord injury: time to move,” *The Lancet*, vol. 377, no. 9781, pp. 1896–1898, Jun. 2011.

[46] S. Harkema, Y. Gerasimenko, J. Hodes, J. Burdick, C. Angeli, Y. Chen, C. Ferreira, A. Willhite, E. Rejc, R. G. Grossman, and V. R. Edgerton, “Effect of epidural stimulation of the lumbosacral spinal cord on voluntary movement, standing, and assisted stepping after motor complete paraplegia: a case study,” *Lancet Lond. Engl.*, vol. 377, no. 9781, pp. 1938–1947, Jun. 2011.

[47] C. W. Chang, Y. K. Lo, P. Gad, R. Edgerton, and W. Liu, “Design and fabrication of a multi-electrode array for spinal cord epidural stimulation,” in *2014 36th Annual International Conference of the IEEE Engineering in Medicine and Biology Society*, 2014, pp. 6834–6837.

[48] “TI ADS1299 Medical Analog Front End.” [Online]. Available: http://www.ti.com/product/ads1299. [Accessed: 18-Oct-2016].

[49] I. Koyanagi and C. H. Tator, “The effects of cortical stimulation, anesthesia and recording site on somatosensory evoked potentials in the rat,” *Electroencephalogr. Clin. Neurophysiol.*, vol. 101, no. 6, pp. 534–542, Dec. 1996.

[50] W. Franks, I. Schenker, P. Schmutz, and A. Hierlemann, “Impedance characterization and modeling of electrodes for biomedical applications,” *IEEE Trans. Biomed. Eng.*, vol. 52, no. 7, pp. 1295–1302, Jul. 2005.

[51] A. Branner, R. B. Stein, and R. A. Normann, “Selective stimulation of cat sciatic nerve using an array of varying-length microelectrodes,” *J. Neurophysiol.*, vol. 85, no. 4, pp. 1585–1594, Apr. 2001.

[52] D. McDonnall, G. A. Clark, and R. A. Normann, “Interleaved, multisite electrical stimulation of cat sciatic nerve produces fatigue-resistant, ripple-free motor responses,” *IEEE Trans.*

Neural Syst. Rehabil. Eng. Publ. IEEE Eng. Med. Biol. Soc., vol. 12, no. 2, pp. 208–215, Jun. 2004.

[53] X. F. Wei and W. M. Grill, "Impedance characteristics of deep brain stimulation electrodes in vitro and in vivo," *J. Neural Eng.*, vol. 6, no. 4, p. 046008, Aug. 2009.

[54] B. Gosselin, "Recent Advances in Neural Recording Microsystems," *Sensors*, vol. 11, no. 5, pp. 4572–4597, Apr. 2011.

[55] Y. Lo, Y. Kuan, S. Culaclii, B. Kim, P. Wang, C. Chang, J. A. Massachi, M. Zhu, K. Chen, P. Gad, V. R. Edgerton, and W. Liu, "A Fully Integrated Wireless SoC for Motor Function Recovery After Spinal Cord Injury," *IEEE Trans. Biomed. Circuits Syst.*, vol. 11, no. 3, pp. 497–509, Jun. 2017.

[56] G. Paxinos and C. Watson, *The Rat Brain in Stereotaxic Coordinates*, 6th ed. New York: Academic, 2006.

[57] S. Butovas, S. G. Hormuzdi, H. Monyer, and C. Schwarz, "Effects of electrically coupled inhibitory networks on local neuronal responses to intracortical microstimulation," *J. Neurophysiol.*, vol. 96, no. 3, pp. 1227–1236, Sep. 2006.

[58] V. S. Polikov, P. A. Tresco, and W. M. Reichert, "Response of brain tissue to chronically implanted neural electrodes," *J. Neurosci. Methods*, vol. 148, no. 1, pp. 1–18, Oct. 2005.

[59] C. McC. Brooks and J. C. Eccles, "Electrical investigation of the monosynaptic pathway through the spinal cord," *J. Neurophysiol.*, vol. 10, no. 4, pp. 251–273, Jul. 1947.

[60] J. L. Parker, D. M. Karantonis, P. S. Single, M. Obradovic, J. Laird, R. B. Gorman, L. A. Ladd, and M. J. Cousins, "Electrically Evoked Compound Action Potentials Recorded From the Sheep Spinal Cord," *Neuromodulation Technol. Neural Interface*, vol. 16, no. 4, pp. 295–303, Jul. 2013.

[61] M. Sharma, A. Gardner, H. Strathman, D. Warren, J. Silver, and R. Walker, “Acquisition of Neural Action Potentials Using Rapid Multiplexing Directly at the Electrodes,” *Micromachines*, vol. 9, no. 10, p. 477, Sep. 2018.

[62] E. M. Maynard, C. T. Nordhausen, and R. A. Normann, “The Utah Intracortical Electrode Array: A recording structure for potential brain-computer interfaces,” *Electroencephalogr. Clin. Neurophysiol.*, vol. 102, no. 3, pp. 228–239, Mar. 1997.

[63] M. G. Bianco, S. A. Pullano, D. Menniti, C. D. Critello, R. Citraro, E. Russo, G. D. Sarro, and A. S. Fiorillo, “Bioinspired Electric Stimulation: Comparison of ECoG Spectrum in the Main Auditory Structures,” in *2019 IEEE International Symposium on Medical Measurements and Applications (MeMeA)*, 2019, pp. 1–5.

[64] A. Soto-Breceda, T. Kameneva, H. Meffin, M. Maturana, and M. Ibbotson, “Irregularly timed electrical pulses reduce adaptation of retinal ganglion cells,” *J. Neural Eng.*, 2018.

[65] S. Elyahoodayan, T. W. Berger, and D. Song, “A Closed-Loop Multi-Channel Asynchronous Neurostimulator to Mimic Neural Code for Cognitive Prosthesis,” in *2018 40th Annual International Conference of the IEEE Engineering in Medicine and Biology Society (EMBC)*, 2018, pp. 1388–1391.

[66] P. Wang, S. Culaclii, W. Yang, Y. Long, J. Massachi, Y. Lo, and W. Liu, “A Novel Biomimetic Stimulator System for Neural Implant,” in *2019 9th International IEEE/EMBS Conference on Neural Engineering (NER)*, 2019, pp. 843–846.